ABSTRACT

Title of dissertation: SYNCHRONIZATION AND PREDICTION OF CHAOTIC DYNAMICS ON NETWORKS OF OPTOELECTRONIC OSCILLATORS

Adam Brent Cohen, Doctor of Philosophy, 2011

Dissertation directed by: Professor Rajarshi Roy
Department of Physics

The subject of this thesis is the exploration of chaotic synchronization for novel applications including time-series prediction and sensing. We begin by characterizing the nonlinear dynamics of an optoelectronic time-delayed feedback loop. We show that synchronization of an accurate numerical model to experimental measurements provides a way to assimilate data and forecast the future of deterministic chaotic behavior. Next, we implement an adaptive control method that maintains isochronal synchrony for a network of coupled feedback loops when the interaction strengths are unknown and time-varying. Control signals are used as real-time estimates of the variations present within the coupling paths. We analyze the stability of synchronous solutions for arbitrary coupling topologies via a modified master stability function that incorporates the adaptation response dynamics. Finally, we show that the master stability function, which is derived from a set of linearized equations, can also be experimentally measured using a two-node network, and it can be applied to predict the convergence behavior of large networks.

SYNCHRONIZATION AND PREDICTION OF CHAOTIC DYNAMICS ON NETWORKS OF OPTOELECTRONIC OSCILLATORS

by

Adam Brent Cohen

Dissertation submitted to the Faculty of the Graduate School of the
University of Maryland, College Park in partial fulfillment
of the requirements for the degree of
Doctor of Philosophy
2011

Advisory Committee:
Professor Rajarshi Roy, Chair/Advisor
Professor Thomas E. Murphy
Professor Brian R. Hunt
Professor Edward Ott
Dr. Louis M. Pecora

Goethe tells us in his greatest poem that Faust lost the liberty of his soul when he said to the passing moment: "Stay, thou art so fair." And our liberty, too, is endangered if we pause for the passing moment, if we rest on our achievements, if we resist the pace of progress. For time and the world do not stand still. Change is the law of life. And those who look only to the past or the present are certain to miss the future.

–John F. Kennedy

Acknowledgments

The main lesson of my graduate studies is that nonlinear dynamics prevails in areas well beyond the physics laboratory. My own state is the result of a complex intermingling of personal interactions, sometimes harmonizing into a shared consciousness but more often as a mixture of disconnected, incoherent, or contradictory ideas. This thesis is a testament to a complicated set of interactions of thoughts, experiences, and – above all – people that, when combined, have lead to something much more than the sum of its parts.

Rajarshi Roy and Thomas Murphy helped identify challenging problems for which even partial solutions expose insights about the essence of synchronization. To seek experiments whose outcomes cast a breadth of implications and which open a new set of questions defines the objective of a good scientist, for which both Raj and Tom are exemplary.

Bhargava Ravoori has been a close collaborator and friend whose ideas have shaped the evolution of the projects contained within this thesis as well as my development into the scientist and man I am today. We have literally traveled the world together and share an unforgettable set of experiences and emotions.

I have been fortunate to have productive collaborations with many scientists, including: Gilad Barlev, Xiaowen Li, Adilson Motter, Edward Ott, John Rodgers, Karl Schmitt, Anurag Setty, Francesco Sorrentino, Jie Sun, and Caitlin Williams.

I am grateful for my scientific and personal interactions with: Stanislaw Antol, Elizabeth Dakin, Syamal Dana, Hien Dao, Aaron Hagerstrom, Rachel Kramer,

Nicholas Mecholsky, Julia Salevan, Ira Schwartz, Abhijit Sen, Gautam Sethia, and Jordi Zamora-Munt.

I thank Yanne Chembo Kouomo, Xiaowen Li, Elbert Macau, and Francesco Sorrentino for their time and efforts in carefully reading and thoughtfully commenting on early drafts of this document. Their advice is responsible for much of its clarity. However, any errors, omissions, and inconsistencies are entirely my own.

I cannot relate the successes of my graduate studies without highlighting the interactions I have had at the three Hands-On Research Schools for Complex Systems in: Gandhinagar, India; São Paulo, Brazil; and Buea, Cameroon. All the participants have been a source of motivation and excitement for my research and for my interests and goals outside of academia. I am grateful to Harry Swinney, Kenneth Showalter, and Rajarshi Roy for their tireless dedication to the School. Harry has been especially inspirational with his mission for low-cost, high reward science.

Finally, I am forever indebted to Rebecca Schofield for her ceaseless encouragement, support, and friendship.

To plot the course of my future is impossible, but the structure of my attractor has been shaped by these interactions.

Table of Contents

List of Figures

Chapter 1

Introduction

1.1 Overview

Modern progress in nonlinear science is primarily due to an interplay between laboratory experiments, mathematical analysis, and computer simulations. Due to this complementary and multifaceted approach, we are in a position to harness the complexity and richness intrinsic to chaotic motion towards powerful and practical applications. We may also begin to answer fundamental questions regarding the emergence of collective behavior between coupled oscillators in which a large number of components evolve in a complicated interdependent choreography. The phenomenon of synchronization, in which temporal order reigns over the competing divergent force of chaos, is the link that connects these pursuits [1]. An understanding of how one specific type of network of interacting chaotic systems can evolve in unison, as a consequence of each individual member adjusting its internal rhythm, can guide our scientific inquiry and may lead to the development of a variety of applications.

To this aim, we study the nonlinear dynamics of a network of time-delayed optoelectronic feedback loop oscillators. The individual components that comprise each loop are reliable and robust photonic devices (including a semiconductor laser diode, fiber optic cables, an optical intensity modulator, a photoreceiver, and ana-

log and digital electronics). These widely-available building blocks are connected in an uncommon architecture in order to generate a wide range of outputs as system parameters are adjusted. The dynamical behaviors range from periodic oscillations to high bandwidth deterministic chaos with varying degrees of complexity and multiple time-scales [2]. This system is a good testbed for experiments on the nature of synchronization as well as a candidate for practical implementations such as for secure communication [3, 4], sensor networks [5], ultra-wideband waveform generation [6], and random number generation [7]. By combining elements from optics and electronics, this setup is easily scalable, modular, and flexible. Utilization of real-time digital signal processing within the feedback structure further enhances the controllability of parameters and reproducibility of experimental conditions [8]. A physical model based on delay differential equations displays excellent agreement with experimental observations [9, 10].

This thesis presents results from three projects. A common theme is the employment of experiments and modeling, in concert, to provide new insights into the nature of chaos and chaotic synchronization with a focus on designing proof-of-principle realizations for novel applications. In the first project, we explore a method based on chaotic synchrony for assimilating limited experimental observations into a computer model to measure system parameters, estimate the current state, forecast the future trajectory, and quantify local predictability. In the second project, we examine the stability of synchronization on an adaptive network with time-evolving coupling strengths and a finite response time. A mathematical formulation reduces this high dimensional stability analysis to a low dimensional problem. In the third

project, we investigate the role of network structure on the robustness of synchronous behavior. A metric based on transient response time-scales is used to classify and rank network topologies.

In the remainder of this Introduction, the importance and novelty of these concepts is highlighted and recent literature pertaining to the subject is briefly reviewed.

1.2 Time-delayed nonlinear dynamics

The temporal evolution of physical, biological, and technological systems is often determined by the current state of the system $\mathbf{x}(t)$ and the state of the system at an earlier point in time $\mathbf{x}(t-\tau)$ [11]. In a laser, the time it takes for light to travel one round-trip of the resonant cavity determines the output optical frequency modes [12]. In the human physiological system, time delays play an important role in the mechanisms responsible for white blood cell production and the breathing rate [13]. In modern communication systems, time delays pertaining to electronic and fiber optic cables are routinely measured and compensated for. In vehicular traffic dynamics, delay in the drivers' reaction is hypothesized to be a major cause of traffic jams [14]. The interaction of delay τ and nonlinearity $\mathbf{F}(\mathbf{x}(t), \mathbf{x}(t-\tau))$ in such systems can generate a rich array of dynamical effects which are sometimes intrinsic for maintaining proper operation [15] and other times detrimental [13, 16]. In this thesis, we utilize the dynamical complexity available in a time delay system for generating a wide array of different waveforms.

Time delays in nature are due to spatially separated entities and a finite propagation speed for communicated signals; delays are given as $\tau = d/v$ where d is the distance between bodies and v is the information transport speed. For electromagnetic radiation which travels at the speed of light, it takes a signal 3.3 ns to travel 1 m. For sound waves in air, a signal propagates the same length in 2.9 ms. The chemical synapse between neighboring neurons leads to a delay of about 2 ms in signal transmission [17]. Delays are also common in technological devices in regards to processor latency, data access times, and queuing delays. In the laboratory, we can devise experiments that incorporate delays due to physical mechanisms such as by introducing specific lengths of electrical or fiber optic cables. We may also find means to mimic time delays found in nature with equipment such as all-pass electrical filters [18, 19], bucket-brigade devices [20], charge-coupled devices [21], or the combination of analog-to-digital converters, digital shift registers, and digital-to-analog converters [22]. In the experiments described in this thesis, time delays are introduced through using a digital signal processing board or by the true propagation delays of light and electrical signals in optical fibers or coaxial transmission lines.

A continuous-time dynamical system with a single discrete time delay is described by a delay differential equation (DDE)

$$\frac{d\mathbf{x}(t)}{dt} = \mathbf{F}(\mathbf{x}(t), \mathbf{x}(t-\tau)). \tag{1.1}$$

The phase space for such an equation is infinite dimensional, because information about $\mathbf{x}$ on the continuous interval $(t-\tau, t)$ is required to fully specify the state at

time t. Especially when $\mathbf{F}$ is a nonlinear function, a DDE may exhibit complex time evolution [23]. The dynamics may exhibit a series of bifurcations as the parameter τ is varied, including a transition to high-dimensional chaos. Solving DDEs is challenging due to the difficulty in establishing a self-consistent initial history and interesting due to the possibility for complex spatiotemporal patterns [24, 25]. Examples of DDEs include: the Mackey-Glass equation [13] and models for fiber ring lasers [25] and optoelectronic feedback loops [26]. It is to be noted that inclusion of time delay within a dynamical system may also be used to stabilize an otherwise chaotic trajectory [27, 28].

1.3 Synchronization of networks of chaotic oscillators

It is expected, and indeed by definition, that two uncoupled chaotic oscillators that are initially nearby in phase space will quickly separate. This divergence is characterized by the maximal Lyapunov exponent h_1 that is defined as the mean exponential separation rate across a chaotic attractor. In terms of equations, two initial conditions $\mathbf{x}_1(0)$ and $\mathbf{x}_2(0)$ with $|\mathbf{x}_1(0) - \mathbf{x}_2(0)| < \epsilon$ will follow independent trajectories $\mathbf{x}_1(t)$ and $\mathbf{x}_2(t)$ such that $|\mathbf{x}_1(t) - \mathbf{x}_2(t)| \sim e^{+h_1 t}$ ($|\bullet|$ is the Euclidean norm). This extreme sensitivity is seemingly in direct conflict with the observation that two interacting chaotic oscillators can track each other's motion in lockstep, i.e. $|\mathbf{x}_1(t) - \mathbf{x}_2(t)| \to 0$. Synchronization of large groups of chaotic systems is a surprising and remarkable phenomenon in which an interconnected web of initially uncorrelated dynamical units converge into a single stable chaotic harmony, i.e.

$\sum_{i,j} |\mathbf{x}_i(t) - \mathbf{x}_j(t)| \sim e^{-\mu t}$ where i and j label the states of the oscillators in the chorus.

In recent decades, a mathematical framework has been developed to describe when synchrony is possible and when it is inevitable. The pioneering work of Kuramoto and others explains coherence in phase oscillators [29]. Pecora and Carroll specified a simple set of criteria for determining if chaotic oscillators will converge [30]. Network structure – the precise strengths and protocol describing how a set of nodes shuffles partial information about their states to one another – is the catalyst that can ensure synchrony and order. In this framework, a node j communicates its state $\mathbf{x}_j$ with a coupling function $\mathbf{H}(\mathbf{x}_j)$ to node i with a coupling strength or weight A_{ij}. In turn, each node i receives a superposition of the signals from all the nodes in the network as $\sum_j A_{ij}\mathbf{H}(\mathbf{x}_j)$. The strengths A_{ij} can be positive, negative, or zero. In the Pecora-Carroll stability analysis, the structure of the complete coupling or adjacency matrix $\mathbf{A}$ is the deciding factor for global synchrony, i.e. for a system of N chaotic oscillators, the solutions are given as $\mathbf{x}_1(t) = \mathbf{x}_2(t) = \cdots = \mathbf{x}_N(t) \equiv \mathbf{s}(t)$. For electronic oscillators, $\mathbf{H}(\mathbf{x}_j(t))$ is a voltage $V_j(t)$ or current $I_j(t)$ and A_{ij} is a gain or attenuation factor. For optical oscillators, $\mathbf{H}(\mathbf{x}_j(t))$ is an optical power $P_j(t)$. For a mechanical oscillator, $\mathbf{H}(\mathbf{x}_j(t))$ may be a position or velocity such as the phase or speed of a pendulum bob $\theta_j(t)$ or $\dot{\theta}_j(t)$ with A_{ij} representing the strength of transferred vibrations through a beam [31] or bridge [32]. In a chemical oscillator, $\mathbf{H}(\mathbf{x}_j(t))$ may represent a concentration within a specific spatial region [33]. In all of these cases, properties of the matrix $\mathbf{A}$ determines whether an interacting group will spontaneously synchronize.

There has been significant recent progress in the study of chaotic synchronization; yet there exist many open problems regarding the implications of network structure on the synchronization of real dynamical systems.

- How have natural systems evolved to enhance [34] or inhibit [35] synchronous behavior?
- Are certain local network motifs expressed to maintain global synchrony [36]?
- How do systems adapt in response to perturbations that affect communication channels [37]?
- Can synchrony be found in networks with disparate units with a wide range of nonidentical parameters [38]?

We can begin to address such questions by understanding the intricacies and limitations of the Pecora-Carroll approach. This thesis reports results from a set of exploratory investigations in this direction.

1.4 Data assimilation and time-series prediction

Synchronization is an essential feature of many communication protocols. As such, chaotic synchronization finds a natural application as a mechanism for transmitting and receiving hidden messages. Using a chaotic carrier to encrypt a signal provides a layer of security because the signal can only be decoded by a synchronized chaotic receiver that is nearly identical to the transmitter. The chaotic cipher algorithm relies on establishing open loop synchronization, in which the receiver unit

establishes synchrony by replacing a single scalar variable in its multi-dimensional equations of motion with a driving signal input from the transmitter [39, 40]. The parameters of the driver and driven systems must be tuned to be closely matched making it difficult for a potential eavesdropper without the proper parameter 'key' to recover an encoded message. This aspect is the justification provided by scientists for privacy and security. Consequently, open loop or unidirectional synchronization can be used as a precise method for ascertaining unknown system parameters. In a similar fashion, a computer can input a recorded scalar variable from a chaos generator into a numerical model, and the programmer can vary features of the dynamical model along with model parameters to construct the best, if still imperfect, representation of the chaotic oscillator. The quality of synchronization, measured as the error between the input time-series and a model-generated output, is a gauge of the accuracy of the model and its associated variables.

In essence, the method of using open loop synchronization to entrain a model to an experimental data sequence is a computational routine for data assimilation [41]. The first step in weather and climate prediction is data assimilation in which sparse data collected from a diverse set of instruments and from a broad swath of locations must be incorporated into a single computer model. This is a challenging effort which is inherently high dimensional and nonlinear in nature, with a great multitude of associated temporal and spatial scales. In terms of open loop synchronization, the measured time series is also limited in its scope: it is but one output function of a high dimensional physical system, it is measured on a digital oscilloscope only at a specific sampling interval and with finite resolution, and it is littered with

unavoidable and unpredictable noise. Moreover, even for laboratory apparatuses, only incomplete and imperfect models can be programmed, especially for a chaotic system, in which a small fluctuation or variation may have a macroscopic effect.

The key objective in data assimilation is to estimate parameters and the current state with a goal of advancing the model to reliably forecast and predict future states. Once open loop synchronization between data and model is achieved to within a prescribed level, the experimental input is terminated and the model is iterated using only its internal signals. Remarkably, if the model is good enough, then the model output continues to track the true observations. Thus, it is discovered that synchronization provides a means for short-term prediction of chaotic time-series. In the long term, prediction is deemed impossible since the model and observations will necessarily diverge, with the error accumulating as $e^{h_1 t}$ where h_1 is the characteristic Lyapunov exponent. Further comparison of model output and experimental observations reveals that this prediction horizon time is not unbeatable [42]. Along a chaotic trajectory, the predictability varies, with some regions along the attractor more amenable to forecasting than others. We can quantify this with a local Lyapunov exponent [43, 44], and thus provide a measure of confidence along with a given forecast.

Conventional schemes for chaos prediction rely on time-series analysis or optimizing black box models [45]. For the former method, a repository of past states is stored and searched for windows in time that resemble the current state and most recent history [46]. The latter method starts with a generic model and evolves its parameters to best match observations [47]. To make predictions, this optimized

model is stepped forward in time using the current measurement as the initial condition. Such algorithms are appropriate when there is little or no knowledge about the underlying physical mechanisms. However, it is more often the case that there are well-developed theories describing the dynamics of the variables of interest. Data assimilation and time-series prediction based on open loop synchronization integrate observational data and physical modeling to reach an efficient and effective balance of these resources.

1.5 Adaptive synchronization and sensor networks

Complete and isochronal synchronization of a network of N chaotic oscillators – when all the states $\mathbf{x}_i$ $(i = 1, \ldots, N)$ follow the same paths without any time shifts [48, 49] – occurs only when a set of restrictive criteria is satisfied. Especially in a time-delay system, where time shifts are fundamental to the dynamics, isochronal synchronization is counterintuitive. One, instead, expects a leader who drives its subsidiaries into dynamic order [50]. Isochronal synchrony breaks this expectation; in this case, synchrony is a decentralized phenomenon – a function of local interactions and not external forcing. To achieve this order, all the couplings between each of the individual nodes must be designed to have a precise structure; all N^2 elements of the adjacency matrix A_{ij} must be appropriately chosen and properly tuned [30]. How can we engineer, or how can nature construct, such an intricate web of connections? How can these constraints be continuously satisfied in the face of unavoidable drifts in parameters? If global order is sensitive to all the A_{ij}'s

adhering to a specific form, how is order maintained when the A_{ij}'s are modified?

Recently, an adaptive synchronization technique to maintain global synchronism even as coupling strengths vary has been suggested [37] and experimentally tested [5]. The method transforms each node into a smart receiver that processes the incoming superposed signal and constantly readjusts the relative coupling strength with respect to an internal feedback signal. This is a decentralized procedure in that each node only requires access to its local signals; no central processor is needed to inspect each of the coupling signals $A_{ij}\mathbf{H}(\mathbf{x}_j(t))$. In this manner, an otherwise unsynchronizable network is converted into a synchronized network. Additionally, the set of local control signals that are constantly updated by the readjustment routine reveals valuable information about the time-varying coupling structure. Hence, adaptive synchronization provides an indirect vehicle for learning about temporal fluctuations and drifts taking place between spatially distributed nodes in a synchronized network.

The network of chaotic oscillators may be considered as a type of distributed sensor network that reports on changes within the spatial region covered by the nodes and their communication links. For example, a system like this could be used for region surveillance. As such, only noise-like chaotic signals are broadcast between nodes, making it difficult for an intruder to perceive he or she is being monitored. This scenario shows how adaptive synchrony can convert an apparent limitation – that global complete synchrony is sensitively dependent on network structure – into an asset useful for a practical purpose. In essence, the chaotic signals being passed throughout a network of chaotic oscillators encode an obscured measurement of the

underlying coupling structure, and adaptive synchronization makes these measures legible.

There are a number of key questions regarding the capability of a chaos-based sensor network. What initial network topology provides the largest operating range in terms of perturbation strengths? Over what time-scales can the sensors react to changes and recover synchrony? How many simultaneous variations can a given network interpret and localize? Can a given network recover from the loss of one or more sensors? We can begin to analyze such questions from the standpoint of the master stability function formalism [51, 30], a mathematical toolkit initially developed to study synchrony of static networks. This toolkit can be extended to handle adaptive networks and to provide insights into the relationship between response time-scales and synchronization range. It can be used to determine, for example, which networks will recover from a perturbations and how quickly [52]. Finally, the robustness of these predictions can be verified on real networks where parameter mismatches and noise are ever-present.

1.6 Master stability function formulation

The Pecora-Carroll analysis [30] considers the stability of a synchronous solution for a generic arrangement of identical coupled oscillators. Here, we outline the main results of this derivation. For N oscillators, the coupled equations of motion are

$$\frac{d\mathbf{x}_i}{dt} = \mathbf{F}(\mathbf{x}_i) + \varepsilon \sum_{j=1}^{N} A_{ij}\mathbf{H}(\mathbf{x}_j) \tag{1.2}$$

where $\mathbf{x}_i$ is the state of the ith oscillator, $\mathbf{F}$ describes the internal dynamics (which could include a feedback delay $\mathbf{x}_i(t-\tau)$), $\mathbf{H}$ is a coupling function (which may also include a coupling delay), A_{ij} is an adjacency matrix element, and ε is an overall coupling strength applied to all of $\mathbf{A}$. Eqs. (1.2) describe a situation where the interactions are linear in nature, i.e. node i receives a linear superposition of outputs from all the other nodes; however, the function $\mathbf{F}$ and $\mathbf{H}$ may be highly nonlinear.

The first step is determining the necessary conditions for synchrony to be admitted by Eqs. (1.2). This is only the case when the row sums $k_i = \sum_{j=1}^{N} A_{ij}$ are uniform, i.e. $k_1 = k_2 = \ldots = k_N \equiv k_0$. The technique described in §1.5 introduces an adaptive weight $\varepsilon \to \varepsilon_i(t)$ at each node to compensate for unequal row sums, even as the A_{ij}'s vary in time. One way to comply with two equal row sum condition is to choose $A_{ii} = -\sum_{j \neq i} A_{ij}$ such that $k_0 = 0$. A coupling matrix defined in this way is called the Laplacian matrix and labeled $\mathbf{L}$. The oscillators coupled in this manner are said to be diffusively coupled, since each incoming signal into a node is offset with an equal and opposite internal feedback term. We note that there is no accepted technique for programming the A_{ii} terms without a prior knowledge about the network structure.

With this row sum constraint satisfied, the second step is to consider the linearized growth of perturbations away from the synchronous solution $\mathbf{x}_i(t) = \mathbf{s}(t)$. If all the differences $\mathbf{x}_i - \mathbf{x}_j$ decay, then the synchronous solutions with $\mathbf{x}_i - \mathbf{x}_j \to 0$ are stable. If even one linearized difference intensifies in time, then global synchrony is broken and it is not possible for the entire set $\mathbf{x}_i - \mathbf{x}_j$ to fall silent in unison. The

variational equation about the synchronous manifold is

$$\frac{d\delta\mathbf{x}_i}{dt} = D\mathbf{F}(\mathbf{s})\delta\mathbf{x}_i + \varepsilon\sum_{j=1}^{N} A_{ij} D\mathbf{H}(\mathbf{s})\delta\mathbf{x}_j \tag{1.3}$$

where $\delta\mathbf{x}_i$ is the variation from $\mathbf{s}$ of $\mathbf{x}_i$ and $D\mathbf{F} = \partial\mathbf{F}/\partial\mathbf{x}$ and $D\mathbf{H} = \partial\mathbf{H}/\partial\mathbf{x}$ are the Jacobians of $\mathbf{F}$ and $\mathbf{H}$ respectively evaluated at the synchronous state $\mathbf{s} = \mathbf{s}(t)$. This is a high dimensional coupled system of equations with its dimensionality proportional to the total number of nodes N. Pecora and Carroll performed an eigenvalue decomposition, which successfully reduces the dimensionality by decoupling all the modes: $[\delta\mathbf{x}_1, \ldots, \delta\mathbf{x}_N] \to [\boldsymbol{\eta}_1, \ldots \boldsymbol{\eta}_N]$ such that the $\boldsymbol{\eta}_i$'s are independent of one another. The decomposition relies on diagonalizing the adjacency matrix, and there are observable differences in dynamics of networks in which the matrix $\mathbf{A}$ is non-diagonalizable [53]. The power of this method is that if all the $\boldsymbol{\eta}_i$'s decay, then so do all the $\delta\mathbf{x}_i$'s. Then it becomes possible to consider only one equation for the evolution a generic $\boldsymbol{\eta}$, and apply it to all the $\boldsymbol{\eta}_i$'s.

The condition for stability of $\boldsymbol{\eta}(t)$ is that the average Lyapunov exponent of the generic variational equation

$$\frac{d\boldsymbol{\eta}}{dt} = D\mathbf{F}(\mathbf{s})\boldsymbol{\eta} + (\varepsilon\lambda) D\mathbf{H}(\mathbf{s})\boldsymbol{\eta}, \tag{1.4}$$

given by $M(\epsilon\lambda) = \frac{1}{T}\ln\frac{|\boldsymbol{\eta}(T)|}{|\boldsymbol{\eta}(0)|}$ in the limit $T \to \infty$, is negative. If this is the case for all the eigenmodes, then the globally synchronous solution $\mathbf{x}_i = \mathbf{s}$ will persist. The function M is the master stability function and must only be measured once for a given $\mathbf{F}$ and $\mathbf{H}$. So, a necessary condition for stability of the synchronous solution is that for $i = 1, 2, \ldots, N-1$, $M(\varepsilon\lambda_i) < 0$, where the λ_i's are the complex eigenvalues of the coupling matrix $\mathbf{A}$. (The single eigenvalue $\lambda_N = k_0$ is ignored in this stability

analysis, because it represents perturbation tangential to the $(N-1)$-dimensional synchronous manifold $\mathbf{x}_1(t) = \mathbf{x}_2(t) = \ldots = \mathbf{x}_N(t)$. Since the synchronized motion is chaotic, the associated Lyapunov exponent is positive.) The master stability function framework separates the chaotic dynamics $\mathbf{x}_i(t)$ from the coupling structure $\mathbf{A}$ and "once and for all" solves the problem of synchronous stability for linear coupling among the network nodes..

The master stability function formulation recasts a question about dynamical behavior, namely synchronization, into the language of the well-studied discipline of graph theory. The eigenvalue spectrum of the adjacency matrix is the link between these realms. The eigenvalues play an important role in determining the availability of synchronous behavior in terms of dynamical systems as well as an important role in graph structure. Graph theoretic results can advance our understanding of coupled nonlinear dynamics.

1.7 Optimal synchronizability and convergence rates

From the location of the adjacency matrix eigenvalues in the complex plane, one can use the master stability function to determine whether if a given network will synchronize, as outlined in §1.6. It is empirically observed that many systems essentially have the same form for their master stability functions $M(\varepsilon\lambda)$ – having a single global minimum along the real axis and a monotonic increase as distance from the central minimum increases [54]. In fact, for systems with coupling delays (i.e. $\mathbf{H}(\mathbf{x}_j(t-\tau))$), there is preliminary theoretical evidence that the contours of

$M(\varepsilon\lambda)$ will form a series of concentric rings about a minimum, independent of the specific form of dynamical equations [55]. Thus, results pertaining to a single type of chaotic network can be generalized to describe common features about a broad class of networks. In particular, in some cases, we may expand the scope of the master stability function analysis to determine not only *if* a network will synchronize but also to quantify *how well* it will.

Synchronizability – the measure of how well a given network topology **A** will synchronize – can be quantified in principally four ways:

- the range of coupling strengths ε over which the network maintains synchrony,
- the minimum coupling cost ε_{min} for achieving synchrony,
- the rate at which an initially uncoupled network converges to the synchronous state upon enabling coupling,
- or the rate at which a network recovers from an applied perturbation.

Recently, the spread of eigenvalues in the complex plane (or eigenspread) has been proposed as an equivalent graph theoretic measure for synchronizability for diffusively-coupled networks [56]. A network with a localized cluster of eigenvalues will have more favorable synchronization properties than a network with a widely distributed eigenvalue spread. The justification for this hypothesis is that for a well-confined eigenspread, all the eigenvalues can be placed close to the global minimum in $M(\varepsilon\lambda)$ by adjustment of ε alone. The extreme case – when all the eigenvalues are equal and thus the eigenspread is zero – is called optimal, and ε can be made such that

the $\varepsilon\lambda$'s coincide with the minimum of the master stability surface. For a given number of nodes N, only a small subset of possible topologies have this trait, and these are designated as optimal topologies. For a binary network, within which all the couplings are fixed to be either on or off (i.e. $A_{ij} \in \{0, 1\}$), this theory has noteworthy consequences for the types of networks that are optimal. Specifically, for a binary network with N nodes and m total links, only networks with an integer multiple of $(N-1)$ links have a possibility of being optimal. A network with many fewer connections than the all-to-all coupling regime (with $N(N-1)$ links) can have synchronization properties equivalent to those of the all-to-all case. This has important ramifications for the design of efficient networks in which less overall energy can be used for communication to achieve optimized synchrony.

An important inference from the discovery that many complex networks share a master stability function structure is that we can utilize results from a prototype network with only a small number of nodes and links to differentiate and classify large networks which house a complicated and tangled web of interconnections. In fact, controlled experimental measurements can be extremely productive in this field of study which, until recently, have been dominated by theoretical work. The knowledge gleaned from experiments on optoelectronic networks of two, three, or four nodes can substantiate theoretical arguments for generic networks of N nodes and inform us about the robustness of theories for real networks. Surprisingly, a two-node network can be used to determine if an N-node network is optimal, a three-node network can be used to determine if an arbitrary network will synchronize [57], and a four-node network can verify the result that quantized arrangements of the

number of links lead to optimal synchrony [58].

The claim that Laplacian eigenspread is related to the convergence rate to the synchronous solution implies that an experimentally observable feature – the transient behavior from uncorrelated to near identical evolution upon instantaneous coupling – is a broadly significant network property. It is commonly thought that the master stability function directly embeds the convergence rate of networks. This incorrect notion is based in the assumption that the slowest eigenmode, the one with $M(\varepsilon\lambda)$ closest to zero, fully dominates the exponential decay rate with a characteristic time-scale $1/M(\varepsilon\lambda)$. In fact, this only holds infinitesimally close to the synchronization manifold. In a real network, a finite synchronization floor is set by mismatches and noise, so that the convergence rate is determined by a combination of all the eigenvalues $M(\varepsilon\lambda_i)$. Nonetheless, by measuring convergence properties of real networks where the eigenvalues have been suitably placed, the transient behavior of arbitrary networks can be well-estimated.

1.8 Outline of thesis

In this introductory chapter, we have provided motivation for studying the subjects presented within this thesis and posed a series of questions regarding fundamental and practical research on chaos synchronization. The following six chapters provide experimental, numerical, and analytical results on studies of networks of optoelectronic time-delayed feedback loops.

In Chapter 2, we systematically introduce the components of an isolated feed-

back loop, which includes: a semiconductor laser diode, fiber optic cable, an electrooptic intensity modulator, a photodetector, an electronic filter, and an electronic amplifier. The basic physics is briefly described along with a mathematical model for each component. The chapter ends with a derivation of the delay differential equations that describe the feedback loop dynamics as well as a discrete-time map that describing the feedback loop when a digital signal processor is employed.

In Chapter 3, the dynamical behavior of an isolated feedback loop oscillator is examined experimentally and numerically as parameters are adjusted. We locate bifurcations – qualitative changes in behavior – as the feedback strength is steadily increased by probing the dynamics in the time-domain, the frequency-domain, and as time-delay embeddings. We construct bifurcation diagrams, and provide a number of metrics for dynamical complexity, including: maximal Lyapunov exponents, Kaplan-Yorke dimensionality, Shannon entropy, and Kolmogorov-Sinai entropy. These provide insights into the rate at which small features are amplified by chaos and help pin down the notion of predictability.

In Chapter 4, we describe a method for using synchronization of a numerical model to a recorded oscilloscope time-trace to make short-term predictions about the future time-series. Much of this work was published in Ref. [10]. A similar technique to experimentally measure convergence behavior of a network is in Refs. [8] and [58].

In Chapter 5, we introduce the notion of anticipated synchronization [59], in which the dynamics of a secondary or tertiary feedback loop can predict what will happen at a primary loop within the next one round-trip or two round-trips. In a

similar manner, a series of cascaded numerical simulations can be designed to lead an experimental time-series.

In Chapter 6, we perform a stability analysis on the adaptive synchronization technique proposed in Ref. [37]. The analysis is applied to an experimental three-node network of optoelectronic oscillators to predict which network configurations preserve synchrony even when the coupling strengths vary. This study is based on our results published in Refs. [42] and [52].

In Chapter 7, we are acquainted with optimal configurations of optoelectronic networks. We use measurements of the convergence rates on two-node networks to estimate convergence rates for large networks that agrees with full nonlinear numerical simulations of 50 nodes and experiments on four nodes.

In Chapter 8, the thesis is summarized and we discuss future directions in terms of further experiments and analyses.

Chapter 2

Components of an optoelectronic feedback loop

In the past fifty years, we have experienced a revolution in information and communication technology driven by a rapid commercialization of basic scientific discoveries. Lasers, optical fiber, and semiconductor electronics and optoelectronics are the backbone of the Internet and modern communication technologies. Optoelectronics have numerous advantages over traditional telecommunication practices including high bandwidth, speed, and efficiency, small footprints, and relatively simple operation. The optoelectronic feedback loops used as chaos generators in this thesis are offspring of the telecommunications industry – employing commercial-off-the-shelf devices in an unusual, yet easily replicable, way. In this Chapter, we introduce the basic physical principles underlying the operation of each of the elements within an isolated feedback loop, and we integrate the individual mathematical descriptions to formulate a model for the feedback loop dynamics.

2.1 Qualitative description of feedback loop components

Before we delve into a quantitative description of the optical, electronic, and optoelectronic devices, let us develop an intuitive sense for the operation of a feedback loop. Fig. 2.1 is an experimental schematic of an isolated feedback loop oscillator.

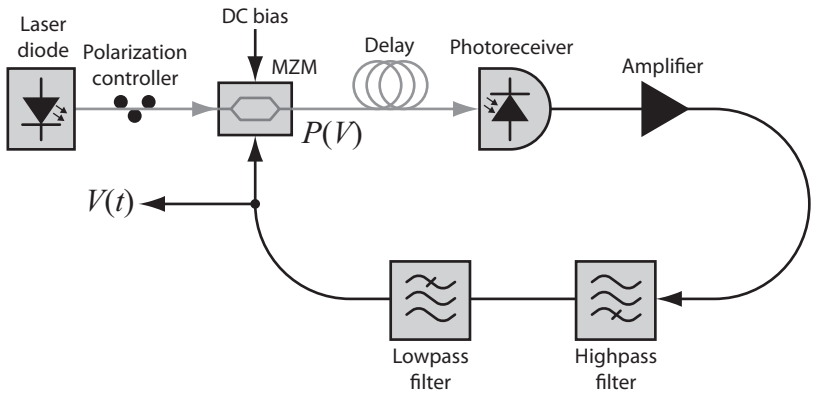

Figure 2.1: Schematic of an optoelectronic feedback loop.

A semiconductor laser diode emits a steady optical power into a fiber optic cable. The light beam is transmitted to a nearby optical intensity modulator (labeled MZM). This device has a single fiber-coupled optical input, a single fiber-coupled optical output, and an electronic voltage input. The optical transmission is an instantaneous nonlinear function of the voltage signal. This function $P(V)$ is the source of nonlinearity within the feedback loop; all other elements operate linearly.

Physically, the optical modulator is similar to a free-space interferometer. The optical signal is split equally between two paths, and the two beams are recombined at the output. If the two branches have exactly the same length, the beams recombine in-phase. If there is a path length difference of one half wavelength, then the beams undergo destructive interference, and no light is output. For this type of modulator, called a Mach-Zehnder modulator, the effective path lengths are controlled via an applied electronic voltage. The waveguides are constructed of lithium niobate, an electrooptic material whose refractive index depends on an applied electric field strength. The electric field is imposed with electrodes along the surface of

the electrooptic crystal. The direction of the electric field is flipped in each arm, so as to have equal and opposite refractive index shifts, and, thus, double the relative phase shift of the recombined beams. The intensity modulator exhibits an interferometric relationship in which the transmission versus applied voltage which is a cosine-squared function. The voltage required to go from full to zero transmission (i.e., a π relative phase shift) is denoted V_π and is determined by the electrooptic coefficient of the waveguide material and the length over which the electric field is applied and the distance between the electrodes. Typically, V_π is on the order of a few volts.

Next, the modulated optical signal is transmitted over fiber to a nearby photodetector which produces an electronic current proportional to the incident optical power. The output photocurrent is converted into a voltage which is subsequently filtered and then amplified by a high gain, high bandwidth linear amplifier. The electronic filters pass a band of frequencies above a frequency f_1 and below a frequency f_2 and strongly attenuate components of the voltage signal outside of this band. Finally, the filtered and amplified voltage is imposed as the modulation voltage to the optical modulator, completing the feedback loop.

The time required for the optical and electronic signal to make a round-trip around the feedback ring is τ and is determined by the length of the optical fiber between the modulator and detector and the length of coaxial cable between the detector, filters, amplifiers, and modulator. For the experimental results presented here, the round-trip time is on the order of tens to hundreds of nanoseconds, compared to filter time-scales of approximately $(2\pi f_1)^{-1} \sim 160$ ns and $(2\pi f_2)^{-1} \sim 2$ ns.

We note that these parameters are easily scalable to much faster [6] or much slower time-scales [8].

It is seen that the dynamical behavior of the modulated light signal is determined by the intensity of the same light signal at an earlier point in time. The feedback strength – qualitatively, how much of the present state is determined by a value of the state in the distant past – can be varied by changing the loop gain, changing the laser power, or including controllable optical or electronic attenuators. In Chapter 3, we will study the dynamics of this feedback loop as the feedback strength is ramped up from zero. The interaction of nonlinearity (via an optical intensity modulator), time delay, and bandwidth limitation provides a wide range of different output waveforms of varying complexity.

2.2 Semiconductor laser diode

A laser is an optical source that emits photons via stimulated emission as a coherent beam. Laser light has extremely high spectral purity, high directionality, and high intensity [12]. All lasers consist of a gain medium having a population inversion with an excess of atoms in an excited state inside of a resonant cavity which is typically a pair of mirrors of high reflectivity. A semiconductor laser uses a forward-biased diode as a gain medium [60]. A dc injection current maintains a large population of charge carriers (electrons and holes) near the diode junction which emit photons upon recombination. Semiconductor lasers have advantages compared with other types of lasers, including: a small size, simplicity in operation,

high efficiency, they are readily connected to electronic circuits, and they are mass-manufactured.

An edge-emitting laser diode is designed as a waveguide structure that is well-suited for coupling into a fiber optic cable. A narrow slab waveguide is formed by sandwiching different semiconductor layers, and the ends are cleaved to act as mirrors. The semiconductor geometry is called a double heterojunction, because it is designed to confine both the optical modes and carriers in an overlapping active region. One common laser diode is a Fabry-Perot laser, which emits photons into a large number of axial modes. The optical spectrum has a set of equally spaced peaks with their frequency spacing given as the standing-wave condition $\Delta f = v/(2L)$ where v is the speed of light within the semiconductor cavity and L is the length of the cavity. In telecommunication applications, the laser wavelength must be carefully controlled, and typically distributed feedback (DFB) lasers are employed. In a DFB laser diode, a periodic grating is constructed along the semiconductor interface and replaces the end mirrors. The grating only reflects a narrow band of wavelengths, and thus the cavity only lases into the single mode which overlaps with both the reflectivity and gain bands. DFB lasers are used as the optical sources for the optical feedback loops in this thesis (manufactured by FITEL and Bookham). The lasers have a central wavelength of approximately 1550 nm.

The light from a laser diode is generated by a supplied electric current I. Each diode is characterized by a lasing threshold current I_0, above which the laser emits photons via stimulated emission. As the pump current is increased beyond I_0, the output optical power increases more or less linearly with the drive current. In

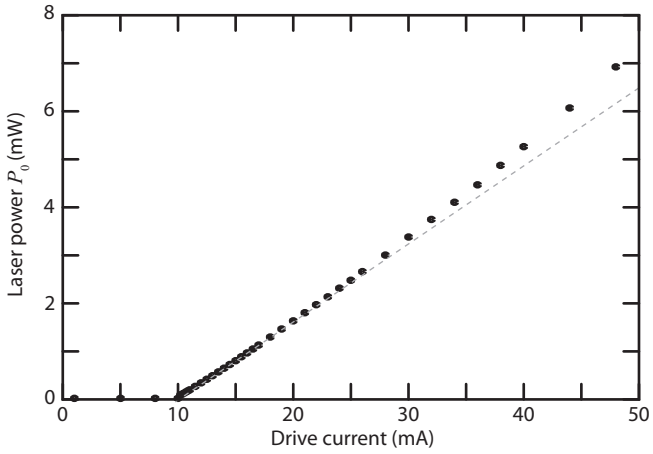

Figure 2.2: Laser diode output power vs. drive current. The threshold current I_0 is approximately 10 mA. Above I_0, the output optical power increases approximately linearly with drive current. The data points were measured from a Bookham LC25W-C laser diode and the dashed curve is a best fit.

Fig. 2.2, we plot the measured output power as the drive current is increased from below threshold to well above threshold. A simple model [61] based on rate equations for carrier density and photon density can capture this result as well as describe some simple laser gain dynamics such as relaxation oscillations and responses to current modulation at different drive frequencies. However, the detailed dynamical behavior of semiconductor lasers as we modulate at high speed is more complex [12] and can not be summarized by a linearized small-signal model. Modulation of the drive current can result in complicated spiking behavior, long transient responses, and distortion.

The study of a time-delayed feedback loop where an electrical feedback signal is imposed as a current modulation to a semiconductor laser diode has been explored in Ref. [26]. In Refs. [3], [7], and [62], a semiconductor laser is operated with an additional external mirror such that the output light signal is re-injected

into the laser cavity. The optical output is an irregular signal that reveals an intricate interaction between chaotic dynamics and amplification of microscopic random noise [63]. There is no complete analytic model that can show good quantitative agreement with experimental measurement, making it difficult to fully diagnose the observed behavior. In the series of experiments presented in this thesis, we operate the laser diode at a steady state point with output power P_0, and we ignore dynamical features and optical noise in our numerical models.

2.3 Single-mode optical fiber

Fiber optics are used to transmit data over long distances with low losses, little distortion, and high speed. Optical signals are insensitive to RF interference and mechanical vibration. The cables are lightweight, flexible, and inexpensive. For these reasons, fiber optics is the standard for global communication, with a single strand of optical fiber able to transmit several terabits of information per second over a distance of many kilometers [21].

A fiber optic cable is a thin glass rod surrounded by a plastic protective buffer. The glass is composed of an inner portion called the core and an outer portion called the cladding. The core and cladding have different refractive indices such that a light beam injected into the core will be guided along due to total internal reflection. Snell's law for refraction describes how light bends at an interface between two dissimilar transmission media and is used to calculate the critical angle above which refraction is impossible. In optical fiber, a light ray is incident on the cladding at

an angle greater than the critical angle of about 7 degrees, so the ray is completely reflected and remains within the core. Historically, John Tyndall was one of the first to demonstrate the principle of guided light via total internal reflection within a narrow stream of flowing water at the Royal Institution Christmas Lecture in 1861 [64].

Single-mode fiber (SMF) allows for transmission of light along only a single path. Multi-mode fiber, on the other hand, allows for numerous signals of the same optical frequency to be sent over a single fiber. The number of allowed modes is a function of the diameter of the code and cladding, with a larger diameter supporting more modes of operation. SMF has a core diameter of 8–12 μm, a cladding diameter of 125 μm, and a coating diameter of 250 μm. SMF has high performance with respect to bandwidth and attenuation, principally because it is completely insensitive to modal dispersion. SMF can transmit more than 40 Gb/s over a single optical channel, and by using wavelength division multiplexing – in which multiple signals are injected at slightly different optical wavelengths – one SMF cable can transmit at data rates greater than 1 Tb/s. At 1550 nm, where losses due to Rayleigh scattering, IR absorption, and molecular resonances are minimized, a signal is attenuated by less than 0.2 dB per kilometer. At high optical power levels, nonlinear effects in optical fiber can cause undesirable effects such as self phase modulation, stimulated Raman scattering, and stimulated Brillouin scattering [65]. In the experiments described in this thesis, the optical power is low and the lengths of optical fiber is short enough as to ignore these effects.

SMF exhibits some degree of birefringence, meaning that it has a non-isotropic,

polarization-dependent refractive index. The birefringence properties are unpredictable and vary along a length of fiber due changes in mechanical stresses such as bends, temperature gradients, and irregularities in the shape of the core. Much of telecommunications is insensitive to polarization, so SMF is appropriate. However, optical intensity modulators require a polarized input, so the signal between a source laser and a modulator is often carried over polarization-maintaining fiber (PMF). PMF has stress rods embedded within its fiber cladding which break the circular symmetry of the core. Thus, two distinct polarization axes are maintained throughout the waveguide.

2.4 Fiber polarization controller

A polarization controller is installed between the source laser and modulator, since the modulator required a polarized input. A polarization controller transforms an arbitrary input polarization state into an arbitrary output polarization state.

A fiber polarization controller is a simple and novel invention that exploits the birefringence of SMF [66]. A birefringent crystal (such as fused silica in fiber optics) has two optical axes along which light components travel at different speeds. Birefringence, also called double refraction, is observed when an ordinary axis (or slow axis) has a different refractive index from that of an extraordinary axis (or fast axis). An injected light wave is resolved into these two axes, and, at the output, there is a phase difference between the components, and thus a modified state of polarization from that of the original beam. In a fiber polarization controller, SMF

is looped into three independent spools with relatively tight radii. The looping of the fiber causes stress and induces birefringence. By twisting the paddle onto which the fiber is looped, the principal axes of the SMF are rotated with respect to an injected polarization vector. We emphasize that the birefringence is due to stress of the loop and not the twisting of the paddles. Each loop follows the same principles as those of a fractional wave plate (also called a retarder) in classical optics [67]. Hence a loop is called a fiber retarder. Three loops allow for complete control of a polarization state. In terms of classical optics, first a quarter-wave plate transforms the input to a linear polarization, next a half-wave plate rotates the linear state, and finally another quarter-wave plate transforms to an arbitrary polarization.

A given rotation on a polarization controller paddle performs an unpredictable retardance. In practice, the output intensity of the optical modulator is observed and the three paddles are iteratively adjusted to maximize the throughput at the beginning of an experiment.

2.5 Mach-Zehnder intensity modulator

As described in §2.1, an integrated Mach-Zehnder modulator is an interferometric device whose optical transmission $P_{\text{out}}/P_{\text{in}}$ is a function of an applied voltage V. The electrooptic material used to form a relative phase shift within the two arms of the interferometer is lithium niobate, which has a large electrooptic coefficient r_{33} and is transparent over the optical communication spectrum. At the input, the incident beam is polarized to orient the oscillating field along with extraordinary

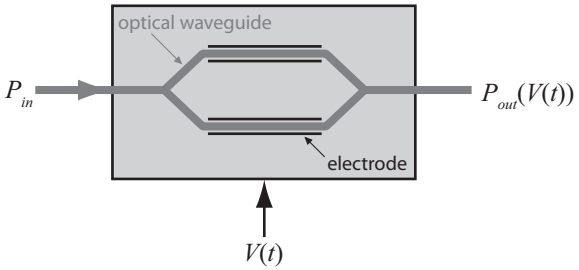

Figure 2.3: Mach-Zehnder optical intensity modulator. The input optical field is split between two waveguides made of lithium niobate. An applied electric field on the waveguides causes a phase shift in the two branches. The two beams recombine and interfere at the output.

axis $\hat{\mathbf{z}}$. The input light is described by

$$\mathbf{E}_{\text{in}} = \sqrt{P_{\text{in}}} e^{i(ky-\omega t)} \hat{\mathbf{z}} \tag{2.1}$$

where $\hat{\mathbf{z}}$ is a unit vector in the direction of polarization, y is the propagation direction, k is the wavenumber, ω is the angular frequency, and P_{in} is the power of the injected light. The input signal is split equally at a Y-branch, with $\mathbf{E}_{\text{in}}/\sqrt{2}$ propagating along each arm. A schematic of a modulator is depicted in Fig. 2.3.

First, consider the situation when no external electric field is applied to the waveguides. Each arm accumulates a phase term of $e^{i\Delta\phi_0}$ due to the path length with $\Delta\phi_0 = 2\pi n_{\text{e}} L/\lambda$ where n_{e} is the unmodified refractive index of lithium niobate, L is the length of each arm, and λ is the wavelength of the light. The two waves combine constructively at the output Y-branch, as the phase factor makes no contribution to $P_{\text{out}} = \langle |\mathbf{E}_{\text{out}}|^2 \rangle$, with $\mathbf{E}_{\text{out}}$ the vector sum of the two phase-shifted fields. Thus, $P_{\text{out}}/P_{\text{in}} = 1$. For a real modulator, there are unavoidable insertion losses. More importantly, the two arms may not have exactly the same path lengths L causing an additional phase shift in one arm.

Now consider the case when a dc electric field of strength $E_{\rm z}$ is applied across the two arms of the interferometer. The field is applied to each arm in an opposite direction, i.e. it is applied in the $+\hat{\mathbf{z}}$ direction for one arm and in the $-\hat{\mathbf{z}}$ direction for the other. Lithium niobate experiences a shift in its refractive index $n_{\rm e} \rightarrow n_{\rm e} + \Delta n_{\rm e}$ given by

$$\Delta n_{\rm e} = 2\pi n_e^3 r_{33} E_{\rm z} \frac{L}{\lambda} \tag{2.2}$$

where r_{33} is electrooptic coefficient, $E_{\rm z} = V/d$ is the dc field, V is the applied voltage, and d is the distance between electrodes supplying the field. In one arm, the phase will see an additional phase of $\Delta\phi = 2\pi\Delta n_{\rm e} L/\lambda$ and the other arm will see the opposite phase shift $-\Delta\phi$. The combined optical power is

$$\begin{aligned} P_{\rm out}(V) &= \frac{P_{\rm in}}{4}\langle |e^{+i\Delta\phi} + e^{-i\Delta\phi}|^2 \rangle & (2.3) \\ &= P_{\rm in}\cos^2\left[\frac{\pi V}{2V_\pi}\right] & (2.4) \end{aligned}$$

where we have defined the halfwave voltage

$$V_\pi \equiv \frac{d\lambda}{2n_{\rm e}^3 r_{33} L}. \tag{2.5}$$

For lithium niobate $n_{\rm e} = 2.2$ and $r_{33} = 30$ pm/V. For a typical modulator, $L = 5$ cm and $d = 100$ μm. Optical communications often uses $\lambda = 1550$ nm, as described in §2.3. With these values, $V_\pi = 4.85$ V. For commercially available modulators, V_π is typically between 3 and 6 volts.

Eq. (2.4) implies that at $V = 0$ (no applied voltage), $P_{\rm out} = P_{\rm in}$. A more realistic model for the Mach-Zehnder intensity modulator transfer function is

$$P_{\rm out}(V) = \eta P_{\rm in}\cos^2\left[\frac{\pi V}{2V_\pi} + \phi_0\right] \tag{2.6}$$

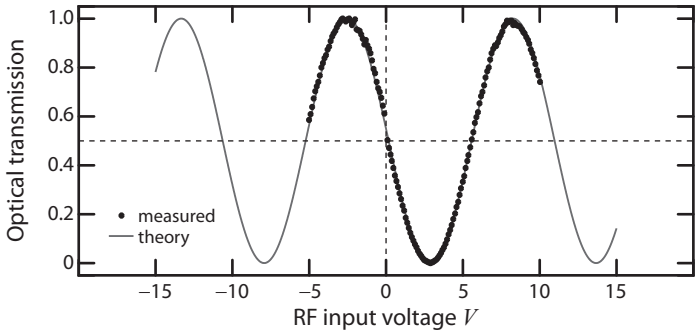

Figure 2.4: The Mach-Zehnder modulator transfer function is a interferometric $\cos^2$ relationship. The output power P_{out} is modulated by an applied voltage V. The points are measured from an JDSU modulator normalized to the maximum output power. The solid line is a best fit with $V_\pi = 5.40$ V and $\phi_0 = 0.735$.

where η is a loss factor and ϕ_0 is a bias term. We may shift the bias by adding a dc voltage to the V to set ϕ_0. Often, ϕ_0 is chosen to be $\pi/4$ so that an ac coupled modulation voltage can drive the modulator from complete transparency ($P_{\rm out} = \eta P_{\rm in}$) to complete extinction ($P_{\rm out} = 0$). The insertion loss η is typically 3 to 6 dB. We note that a Mach-Zehnder modulator can respond to fast changes in the modulator voltage $V = V(t)$ up to tens of GHz making them ideally suited for optical data transmission. These devices are in widespread use by the telecommunications industry since they have none of the problems associated with fast switching of the injection current of a semiconductor laser (as discussed in §2.2).

In Fig. 2.4, we plot the measured transmission function normalized to the maximum output of a Mach-Zehnder modulator manufactured by JDSU with $V_\pi = 5.40$ and $\phi_0 = 0.735$. In Fig. 2.5, the output function for a Lucent Technologies modulator is shown on a logarithmic scale. The insertion loss is about -6.3 dB, corresponding to $\eta = 0.21$. This model has a electronically variable optical attenuator integrated into the package which increases the insertion loss.

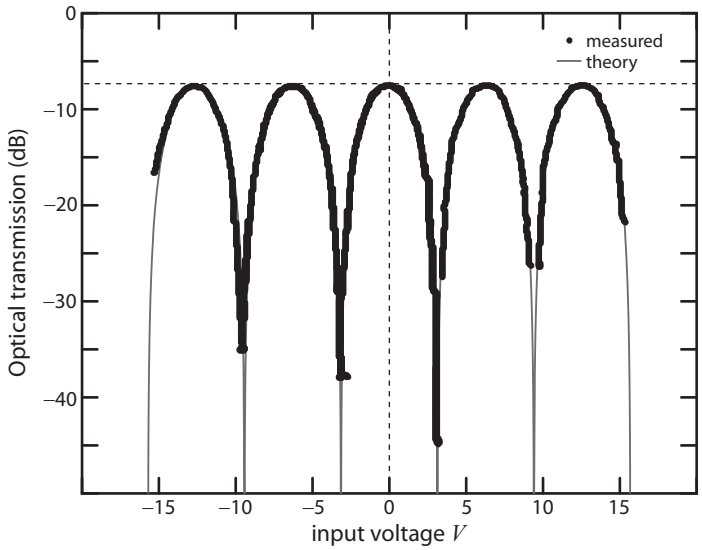

Figure 2.5: Mach-Zehnder modulator extinction characteristics. Data points are for a JDSU moduluator and the solid curve represents a transfer function with $V_\pi = 3.14$ V, $\phi_0 = 0$, and insertion loss 6.3 dB. The extinction ratio is approximately 28 dB.

2.6 Photodetection

A photodetector is an optoelectronic device that outputs an electrical signal in response to incident light. It consists of a photodiode which generates a photocurrent by absorption of photons and a transimpedance or current-to-voltage amplifier. The output voltage V is linearly proportional to the incident optical power P.

The most important electrical property of a diode is its ability to rectify. For optoelectronics, the use of a diode is different; they can be used for photodetection or as light emitters such as LEDs or lasers (as discussed in §2.2). The diode structure is a good way to collect electrons and holes generated by optical absorption and turn the result into an electric current. A reverse-biased photodiode has little current output in the absence of light, but efficiently generates a photocurrent from absorbed photons. An unbiased diode junction can be used to harvest electrical power from

light, as in a solar cell [68].

A photodiode is characterized by its quantum efficiency η_{q} (defined as the number of electrons produced per incident photon) and responsivity S (the photocurrent per unit incident optical power). A well-designed photodiode absorbs essentially all the incident photons and thus achieve close to $\eta_{\mathrm{q}} = 1$. The responsivity, measured in units of A/W, is given as

$$S = \frac{\eta_{\mathrm{q}} q}{\hbar\omega} \tag{2.7}$$

where q is the charge of an electron and $\hbar\omega$ is the quanta of energy delivered by a single photon. The fiber-coupled InGaAS photodiodes used in this set of experiments have a responsivity of 0.9 A/W at 1550 nm. Typically, the transimpedance gain G_{TIA} is on the order of 1000 V/A. Thus a $P = 0.2$ mW optical signal will produce a dc voltage of $V = G_{\mathrm{TIA}} SP = 180$ mV. However, the high-gain amplifier is ac-coupled, so it only passes fluctuating signals as an output voltage. For telecommunications-grade drives, the pass band typically goes from tens of kHz to many GHz.

2.7 Electronic amplification

The ac-coupled output voltage of the photodetector has an amplitude in the range of 10s of millivolts. The characteristic voltage for an optical modulator is $V_\pi \sim 5$ V. A voltage gain G_{amp} is required to boost the feedback signal to an appropriate level in order to observe interesting dynamics. A high-gain, broadband RF amplifier is employed. The MiniCircuits TIA-1000-1R8 has a rated gain of 38 dB within the band of 500 kHz to 1 GHz and provides sufficient power to drive the

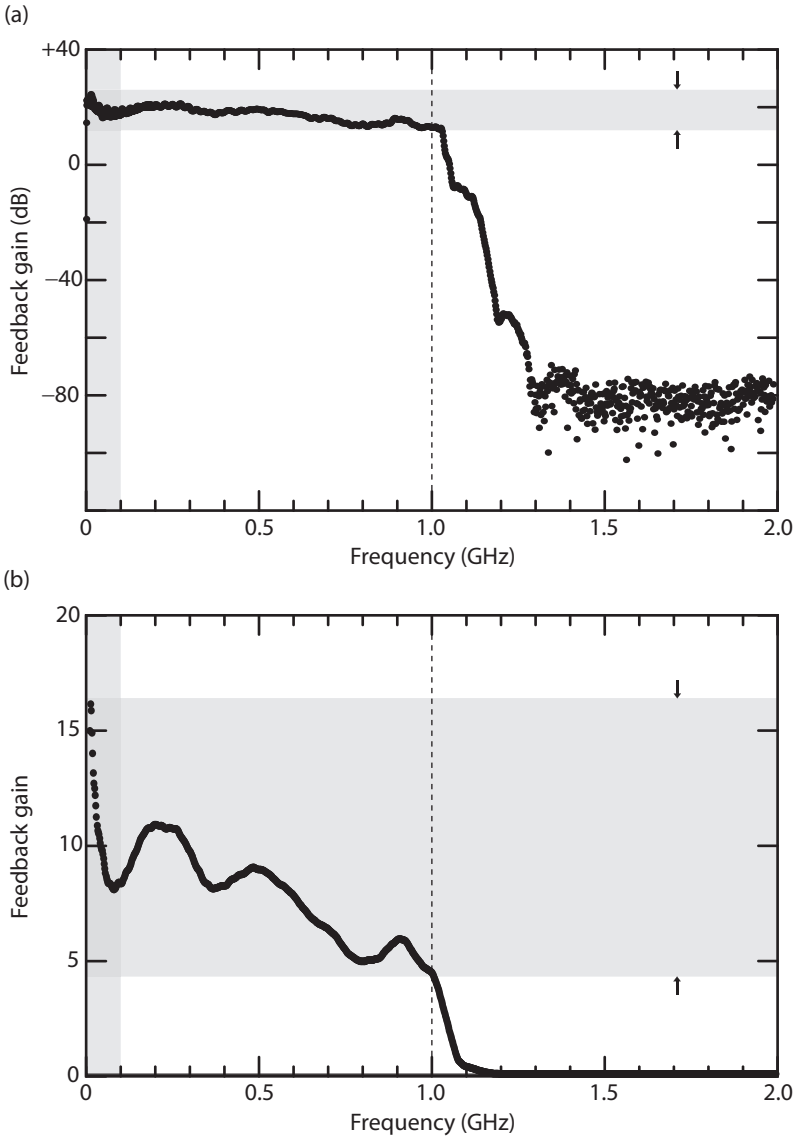

Figure 2.6: Feedback frequency characteristics without bandwidth limitation. (a) The feedback channel spans an electrical bandwidth of 500 kHz to 1 GHz with a gain ripple of about 6 dB. (b) On a linear scale, the feedback gain varies by a factor of 3 within the band.

modulator (a maximum of 35 dBm = 12.5 V into a 50 Ω impedance load).

A network analyzer is a test and measurement instrument that provides magnitude and phase response properties of a device or system. It outputs a swept sinusoid and uses analog detection to measure the amplitude and phase at each fre-

quency. The network analyzer test signal is injected as the modulator voltage and the amplifier output measured. In Fig. 2.6, the magnitude response is plotted for an open loop. For this measurement, a New Focus 1611 photodectector and a MiniCircuits power amplifier were used in the optoelectronic feedback path. The highpass cut-on frequencies are 30 kHz and 500 kHz respectively, and each has a lowpass cutoff frequency of 1 GHz. In (a), the magnitude is plotted on a semilogarithmic scale. As expected, the gain is relatively flat over the pass band and is strongly attenuated below and above it. In the pass band, there is a gain ripple of 3–6 dB, which is typical for a broadband, high-gain amplifier. The same data is plotted on a linear scale in (b). Here, we notice that a 3–6 dB gain ripple corresponds to large linear variation. A low frequency signal is amplified almost twice as strongly as a high frequency signal.

When the feedback loop is closed, interesting dynamical waveforms are observed. However, it is difficult to construct an analytic model that matches the observed behavior with sufficient accuracy for the studies presented in Chapters 4 and 5. The strong roll-off in feedback gain at low and high frequency can be modeled as high-order linear filters, but realistically capturing the details of the gain ripple within a model remains a challenge. Our solution is to modify the experimental system by intentionally restricting the bandwidth to a range where the gain ripple is small by incorporating a well-understood bandpass filter within the feedback path. This is the subject of §2.8.

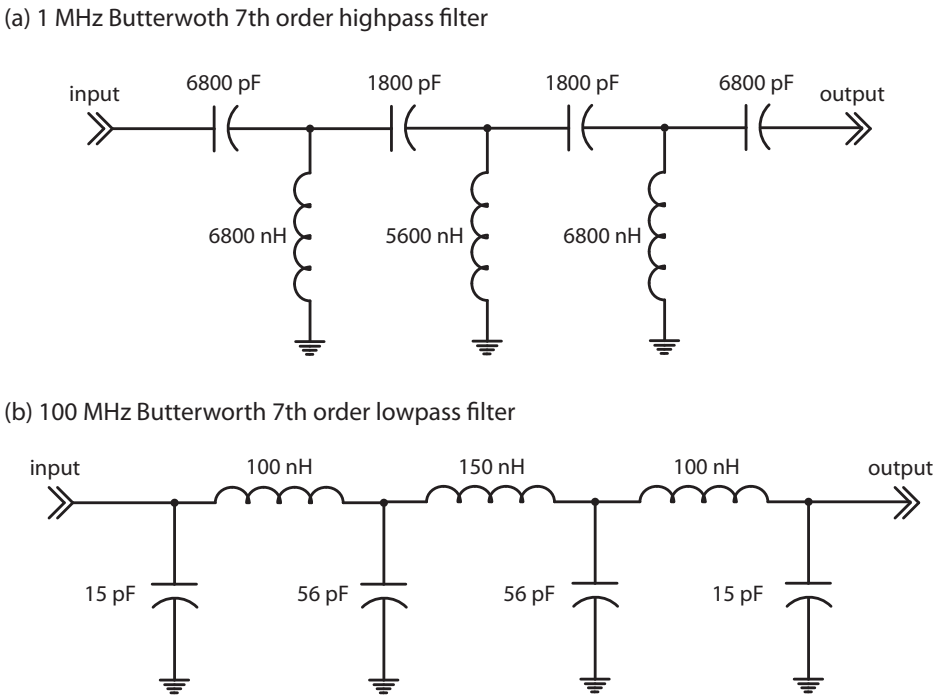

Figure 2.7: Circuit diagrams for passive Butterworth filters. (a) 7th-order highpass filter with cutoff frequency $f_1 = 1$ MHz. (b) 7th-order lowpass filter with cutoff frequency $f_2 = 100$ MHz.

2.8 Electronic bandpass filter

Restricting the feedback bandwidth has the key advantage that the frequency characteristics can be accurately described by an analytic model. We use a pair of cascaded passive filters: a 7th-order Butterworth highpass filter and a 7th-order Butterworth lowpass filter with cutoff frequences of $f_1 = 1$ MHz and $f_2 = 100$ MHz respectively. An Mth-order passive filter require M reactive elements (inductors and capacitors) to implement. In Fig. 2.7, the circuit diagrams for the two filters, each with 7 elements, are shown. These filters are designed to have 50 Ω input and output impedances.

Butterworth filters are designed to be minimally flat in the pass band. The

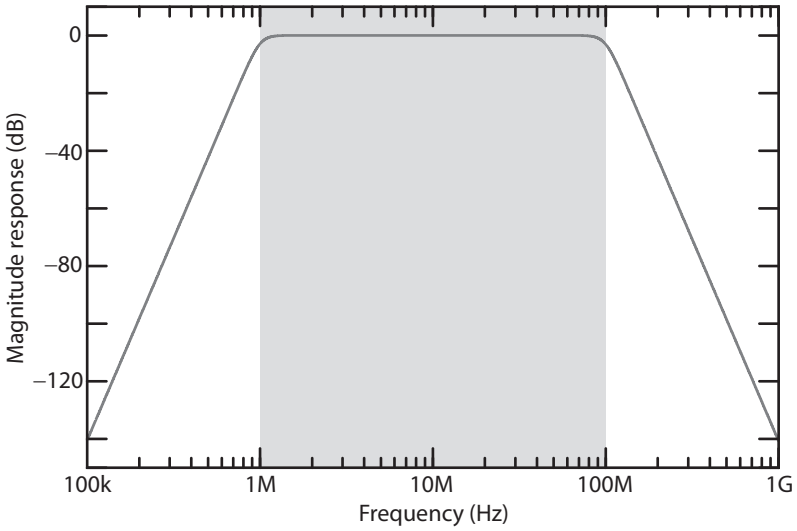

Figure 2.8: Calculated Butterworth bandpass filter transfer function with a pass band of 1–100 MHz.

calculated magnitude response for the combined 14th-order bandpass filter formed by connecting the highpass filter and lowpass filter in series is plotted in Fig. 2.8. As expected, for a 7th-order filter the rolloff is −140 dB/dec. The measured step response is plotted in Fig. 2.9(a). Mathematically, the step response is a convolution of a Heaviside function and the filter's impulse response, which uniquely describes a given filter. The calculated step response (Fig. 2.9(b)) matches the measured result. Thus, we can expect a mathematical model for these filters to describe their actual behavior, even in terms of their transient response.

A linear, time-invariant filter is defined by its Laplace domain transfer function

$$H(s) = \frac{B(s)}{A(s)}, \tag{2.8}$$

where the argument s is a complex frequency, and $B(s)$ and $A(s)$ are Mth order polynomials whose coefficients uniquely define the filter. For a given input voltage

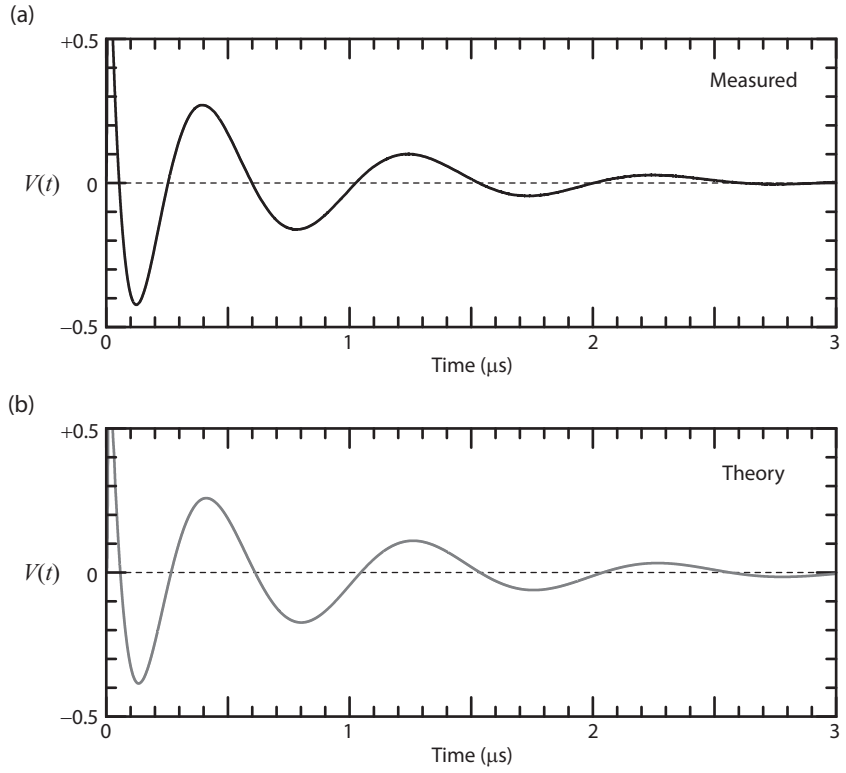

Figure 2.9: Butterworth filter step response. (a) Measured. (b) Calculated.

signal $V_{\text{in}}(t)$, the output $V_{\text{out}}(t)$ is given as

$$V_{\text{out}}(t) = \mathcal{L}^{-1}\Big\{H(s)\mathcal{L}\{V_{\text{in}}(t)\}\Big\}, \tag{2.9}$$

where $\mathcal{L}\{\bullet\}$ and $\mathcal{L}^{-1}\{\bullet\}$ are a Laplace and inverse Laplace transform respectively. An alternative representation is in the time-domain: an Mth-order filter's input–output relationship can be expressed by a single Mth-order ordinary differential equation or by M first-order differential equations and a single algebraic equation. In the latter representation, the equations are

$$\frac{d\mathbf{U}(t)}{dt} = \mathbf{A}\mathbf{U}(t) + \mathbf{B}V_{\text{in}}(t) \tag{2.10}$$

$$V_{\text{out}}(t) = \mathbf{C}\mathbf{U}(t) + \mathbf{D}V_{\text{in}}(t) \tag{2.11}$$

where $\mathbf{U}(t)$ is state space vector of length M. The filter matrices are $\mathbf{A}$, $\mathbf{B}$, $\mathbf{C}$,

and **D** which can be derived from the coefficients of $A(s)$ and $B(s)$. For the 14th-order bandpass filter described above, **A** is (14×14), **B** is (14×1), **C** is (1×14), and **D** is (1×1). For a strictly proper transfer function (for which the polynomial order of $B(s)$ is greater than the order of $A(s)$), $\mathbf{D} = 0$. The matrices for a given polynomial transfer function $H(s)$ can be directly computed using Matlab. For a filter with $M \geq 2$, there are many different state state realizations for the same transfer function $H(s)$, and, in practice, some representations may be numerically unstable.

2.9 Time delay

Time delay is due to the length of optical fiber between the modulator and detector and lengths of the RF cables between the individual components. The refractive index of SMF is $n_{\mathrm{SMF}} = 1.47$, so the light signal propagates at $v = c/n = 0.204$ m/ns. For copper coaxial cable with a solid dielectric, $n_{\mathrm{coax}} \approx 1.52$ so the signals travels at $v = 0.198$ m/ns. For the experiments described in Chapters 3 and 4, the total measured round-trip time delay τ is 22.45 ns, corresponding to a total length of fiber and RF cable of about 5.5 m.

A method to have much longer time delays (applied in the experiments described in Chapters 6 and 7) without requiring an impractical bundle of cables is to use a combination of an analog-to-digital convertor (ADC), a bank of digital shift registers, and a digital-to-analog converter (DAC). A digital signal processing (DSP) board (Spectrum Digital DSK6713), originally designed for audio processing,

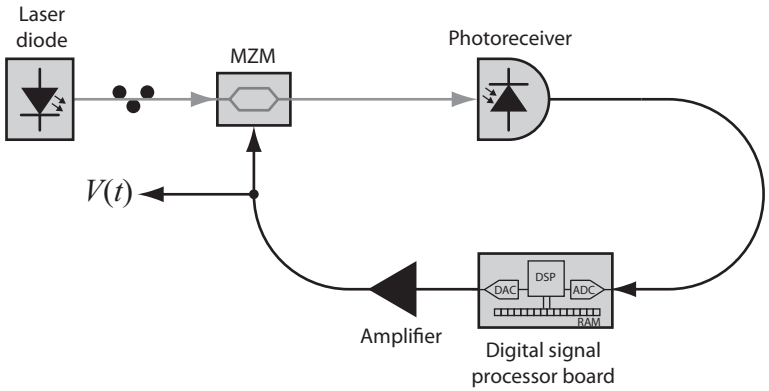

Figure 2.10: Schematic of an optoelectronic feedback loop using a DSP board for delay and filtering.

packages all these components along with a programmable microprocessor. Signal delays of milliseconds to minutes are possible by continuously storing the sampled signal in a memory buffer for a programmed number of sample intervals.

The ADC and DAC are capable of recording and transmitting analog signals at up to 48 kHz when the sample rate is set to 96 kilosamples/s. To use a DSP board for delay, one must modify the frequency characteristics of the rest of the feedback loop to operate at audio speeds. Principally, the transimpedance and voltage amplifiers must respond to low frequency inputs. This is achieved using operational amplifier (LM741) circuits for both. The analog filter (described in §2.8) is replaced with a digital filter programmed on the DSP, with a pass band from a few Hz up to tens of kHz. Fig. 4.13 is a schematic of a DSP-based feedback loop. The details for the DSP-based optoelectronic feedback loop are presented in Refs. [8], [42], and [69]. We note that scaling down the frequencies into the audio range and using a DSP board within the feedback architecture greatly increases flexibility and controllability. More importantly, the system uses only low-cost and

widely-available components, making this an ideal system for experiments involving numerous realizations of identical systems. Using a high performance DSP system or a mixed-signal field-programmable gate array, the same feedback operations could be performed at hundreds of megahertz.

2.10 Continuous-time delay differential equation model

In this section, we merge the mathematical descriptions of the individual components that form a complete optoelectronic feedback loop into a single delay differential equation model. Here, we consider a loop with analog filters described in §2.8. This model captures all the salient features of the dynamics by incorporating the nonlinearity, time delay, and bandwidth limitation. It provides very good quantitative agreement with the experimental observations, as will be presented in Chapter 3. However, we emphasize that this simple model is imperfect and neglects effects which may be essential in some circumstances. The model does not include electronic and optical noise terms, hysteresis due to time-varying parameters, or feedback gain ripple.

Since the system is a loop, the dynamics may be modeled at any point in the loop. It suffices to consider variables representing the output voltage of the electronic filter V_{out} and the state space vector of the filter $\mathbf{U}$ to determine the solution everywhere in the loop. Tracing along the experimental schematic (Fig. 2.1), the output of the filter is amplified by a gain G_{amp}. The voltage $V(t) = G_{\text{amp}} V_{\text{out}}(t)$ is applied to the modulator as the modulation voltage. We note that, in reality, the

delay is distributed throughout the loop, but for modeling purposes it is adequate to assume an instantaneous transfer between components and one single lumped delay τ. The optical power is modulated by the drive voltage with a response given by Eq. (2.5):

$$P(t) = \eta P_0 \cos^2\left[\frac{\pi G_{\text{amp}} V_{\text{out}}(t)}{2V_\pi} + \phi_0\right], \tag{2.12}$$

where P_0 is the steady optical power injected into the modulator. Next, this optical signal is incident on the photodetector with a linear responsivity S and gain G_{TIA}. In the real situation, the photodetector output voltage is highpass filtered. Since the dominant source of bandwidth restriction is the 14th-order Butterworth filters which have cutoff frequencies well above and below every other component, it is reasonable to disregard all other filtering operations (at the photodetector and RF amplifier). A dc-coupled version of the photodetector output voltage is:

$$V_{\text{PD}}(t) = G_{\text{TIA}} S \eta P_0 \cos^2\left[\frac{\pi G_{\text{amp}} V_{\text{out}}(t)}{2V_\pi} + \phi_0\right]. \tag{2.13}$$

This is precisely the input signal to the filter, after it has been delayed by τ. The complete feedback loop model is thus:

$$\frac{d\mathbf{U}(t)}{dt} = \mathbf{A}\mathbf{U}(t) + \mathbf{B} G_{\text{TIA}} S \eta P_0 \cos^2\left[\frac{\pi G_{\text{amp}} V_{\text{out}}(t-\tau)}{2V_\pi} + \phi_0\right] \tag{2.14}$$

$$V_{\text{out}}(t) = \mathbf{C}\mathbf{U}(t) \tag{2.15}$$

where we have used the fact that $\mathbf{D} = 0$ for the bandpass filter. Inserting Eq. (2.14) into (2.13), we have

$$\frac{d\mathbf{U}(t)}{dt} = \mathbf{A}\mathbf{U}(t) + \mathbf{B} G_{\text{TIA}} S \eta P_0 \cos^2\left[\frac{\pi G_{\text{amp}} \mathbf{C}\mathbf{U}(t-\tau)}{2V_\pi} + \phi_0\right]. \tag{2.16}$$

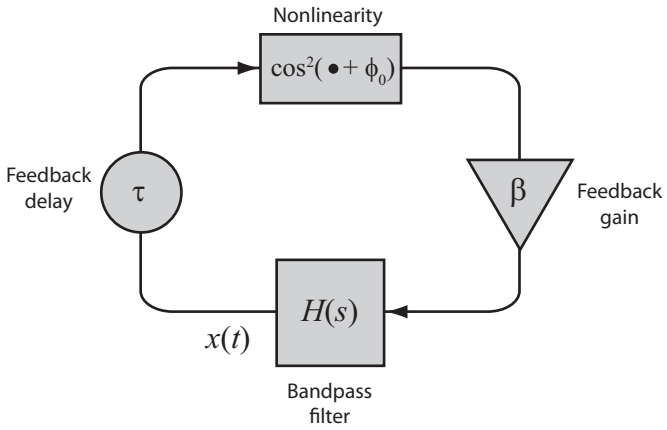

Figure 2.11: Mathematical block diagram for feedback loop model where $x(t)$ is the observed scalar variable.

We rescale the state space vector and filter output to form dimension variables:

$$\mathbf{u}(t) = \frac{\pi G_{\text{amp}} \mathbf{U}(t)}{2V_\pi}, \tag{2.17}$$

$$x(t) = \frac{\pi G_{\text{amp}} V_{\text{out}}(t)}{2V_\pi}. \tag{2.18}$$

We define a dimensionless feedback strength

$$\beta = \frac{\pi G_{\text{TIA}} G_{\text{amp}} \eta S P_0}{2V_\pi} \tag{2.19}$$

that measures the strength of the time-delayed, nonlinearly transformed filter output that returns to the filter. We measure β as the round-trip small signal gain when the modulator is biased at $\phi_0 = \pm\pi/4$. Notice that β is proportional to laser power P_0. The dimensionless equations are:

$$\frac{d\mathbf{u}(t)}{dt} = \mathbf{A}\mathbf{u}(t) - \mathbf{B}\beta \cos^2[x(t-\tau) + \phi_0], \tag{2.20}$$

$$x(t) = \mathbf{C}\mathbf{u}(t), \tag{2.21}$$

where $x(t)$ is proportional to the modulation voltage $V(t)$ and $P_0 \cos^2[x(t) + \phi_0]$ is the optical signal output by the modulator. The negative sign in front of β indicates

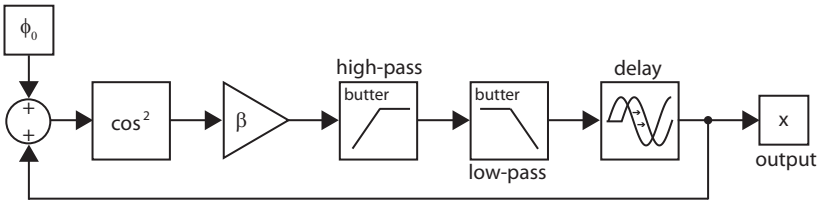

Figure 2.12: Simulink block diagram for feedback loop.

that the loop has negative feedback since the transimpedance amplifier is inverting.

Eq. (2.20) and (2.21) are a realistic physical model for the optoelectronic feedback loop dynamics. A mathematical block diagram is a good way to illustrate the most important feature of the model, as depicted in Fig. 2.11. The output of the filter $x(t)$ returns as an amplified, time-delayed, nonlinearly transformed version of itself.

Eq. (2.20) and (2.21) can be numerically iterated using a DDE solver routine. This is a similar to an ODE solver in which the time axis is discretized with a time step dt. For higher-order methods (such as Heun's method or the Runge-Kutta method), one complication involves how to estimate the solution $x(t)$ between the mesh points. A typical scheme is to use spline interpolation for estimation. For this initial value problem the initial conditions must be specified for $\mathbf{u}(t)$ at $t = 0$ and for $x(t)$ on the interval $(-\tau, 0)$ with a spacing dt. Thus, the initial state is described by $14 + \tau/dt$ numbers.

Simulink, a graphical programming environment, has a vast library which is ideal for simulating the evolution of this delay dynamical system. An image of the Simulink block diagram used for modeling the optoelectronic feedback is Fig. 2.12. The Simulink diagram resembles the mathematical block diagram.

2.11 Discrete-time map equation model

When a DSP board is used to implement the feedback delay and filter operations, the physical model is similar to that of the continuous-time case. In fact, one can effectively use the same model by appropriately selecting the set of matrices $\{\mathbf{A}, \mathbf{B}, \mathbf{C}, \mathbf{D}\}$ for the particular digital filter realization and scaling the delay τ. However, under some circumstances an accurate representation requires transforming the analog filter to a digital filter operating in discrete time. We note that this transformation must be undertaken in order to program the DSP, and thus a discrete time model is actually an exact description of the filter. Instead of considering the variable $x(t)$ whose domain is all of time t, the discrete time solution is given only at the sample times $nT_\mathrm{s} = n/f_\mathrm{s}$ where T_s is the time interval between successive samples of the ADC, f_s is the sampling rate, and n is an integer. The time-series $x[n]$ is given by a map equation with the iterate $x[n+1]$ a function of the past iterates: $x[n], x[n-1], \ldots$.

The design of a digital filter that mimics an analog filter is presented in Refs. [8], [42], and [69]. The basic transformation takes the Laplace domain transfer function $H_\mathrm{a}(s)$ to its z-domain counterpart $H_\mathrm{d}(z)$. A major distinction between these representations is that a digital filter has a strict upper bound for the bandwidth given as the Nyquist rate $f_\mathrm{N} = f_\mathrm{s}/2$, and for an analog filter, frequencies can go off to infinity. If the desired lowpass cutoff frequency f_2 is well below f_N, then this aspect has minimal consequences, and hence the continuous-time equations are valid.

The discrete-time equations of motion can be motivated by drawing a mathe-

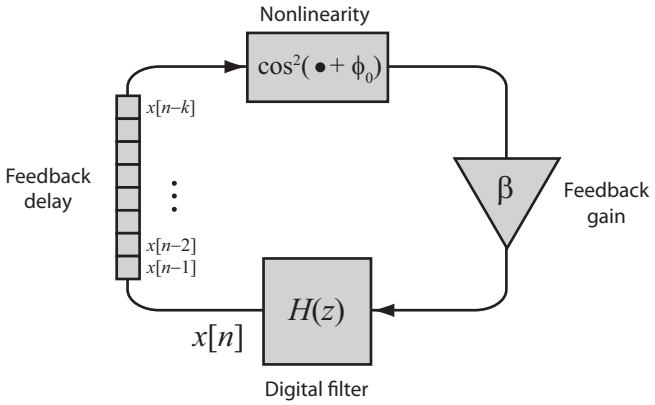

Figure 2.13: Mathematical block diagram for discrete-time feedback loop model.

matical block diagram (Fig. 2.13). $x[n]$ is the output of the filter at time n, and it returns as the filter input as $-\beta\cos^2(x[n-k]+\phi_0)$ where $k=\tau/T_s$ is the feedback delay in terms of length of the memory buffer. A generic digital filter can be written as:

$$x_{\text{out}}[n] = -\sum_{m=1}^{M} a_m x_{\text{out}}[n-m] + \sum_{m=0}^{M} b_m x_{\text{in}}[n-m] \tag{2.22}$$

where M is the order of the filter and the $2M+1$ coefficients $\{a_m, b_m\}$ are specific to the filter design. For the simplest bandpass filter ($M=2$) with $f_s = 24$ kHz, $f_1 = 100$ Hz, and $f_2 = 2.5$ kHz, the parameters are $a_1 = -1.4962$, $a_2 = 0.5095$, $b_0 = -b_2 = 0.2452$, and $b_0 = 0$. Thus the discrete-time dynamics of the optoelectronic feedback loop are described by the map:

$$x[n] = -a_1 x[n-1] - a_2 x[n-2] - b_0\beta(\cos(x[n-k]+\phi_0) - \cos(x[n-k-2]+\phi_0)). \tag{2.23}$$

This map is an extremely simple and elegant formulation that encapsulates all the salient features of the time-delay feedback loop dynamics. By iterating x while varying the parameter β, one can see a striking array of complex waveforms (presented in Refs. [8] and [69]).

2.12 Summary

1. The modular components of an optoelectronic feedback loop are ubiquitous in telecommunication networks and are thus widely available at low-cost.

2. The physics of each component is well understood and conducive to numerical modeling.

3. By imposing a bandwidth restriction on the feedback path with an electronic bandpass filter, we avoid modeling the complicated gain ripple behavior of the RF amplifier.

4. The time scales of a feedback loop (bandwidth and time delay) can be modified to operate anywhere from the audio to microwave range.

5. A digital signal processing board allows for real-time control and exact replication of system parameters.

Chapter 3

Optoelectronic chaotic dynamics

In Chapter 2, we reviewed the physics underlying the components that make up an individual optoelectronic feedback loop oscillator, and we presented a mathematical model based on delay differential equations or difference equations that describes the physics. In this Chapter, we study the output behavior $x(t)$ as the feedback strength parameter β is varied. The other parameters are fixed as $\phi_0 = \pi/4$, $f_1 = 1$ MHz, $f_2 = 100$ MHz, and $\tau = 22.45$ ns unless otherwise noted. Experimental time traces are compared with numerical solutions in the time-domain, frequency-domain, and as time-delay embeddings. The transition to chaos as β is increases is identified via a bifurcation diagram and spectral signatures. The complexity of the output waveforms is estimated by calculating the maximal Lyapunov exponent h_1, the spectrum of Lyapunov exponents $\{h_j\}$, the Lyapunov dimension D_{L}, the information entropy H_{S}, and the Kolmogorov-Sinai entropy rate h_{KS}. These metrics provide some insight into the expected predictability of a dynamical system (the subject of Chapter 4).

3.1 Route to chaos

After the optoelectronic feedback loop has been closed, an output voltage proportional to $x(t)$ is observed and recorded by a high-speed digital oscilloscope.

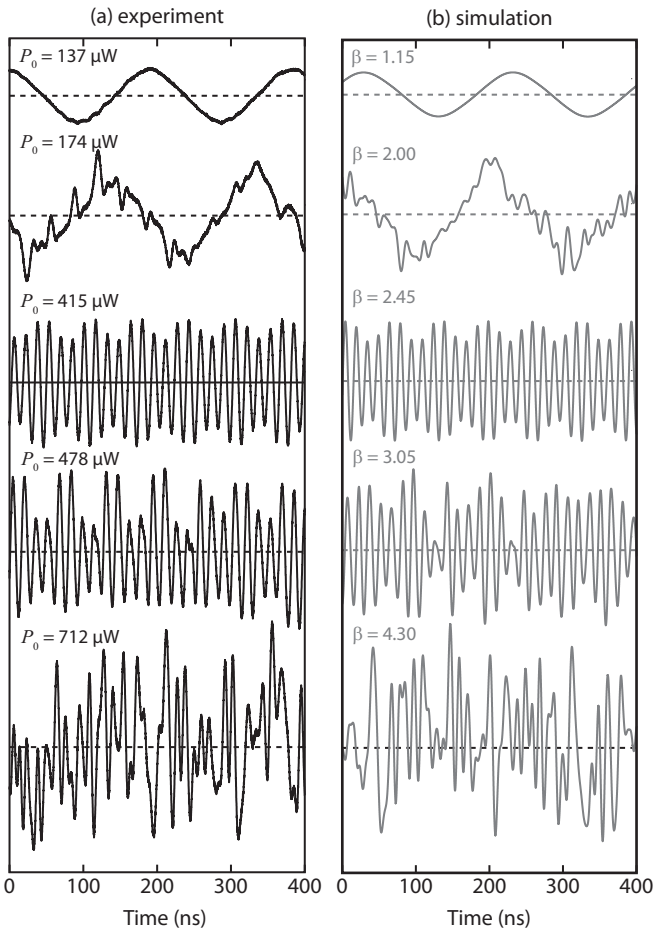

Figure 3.1: (a,b) Experimental (simulated) dynamics for a range of feedback strengths.

By incrementally increasing the injected laser power P_0 (by tuning the laser drive current), we see $x(t)$ transition from a flat line at 0 V to sinusoidal oscillations that steadily increase in amplitude to types of other periodic oscillations to more complex waveforms and finally to a signal that resembles band-limited white noise. Some of these transitions evolve gradually and others are abrupt. In Fig. 3.1(a), we plot a selection of these waveforms within this sequence. The top trace has an input power of $P_0 = 137$ μW and has oscillations that are much slower than the round-trip time. The bottom trace, with $P_0 = 712$ μW, displays no regular periodicity

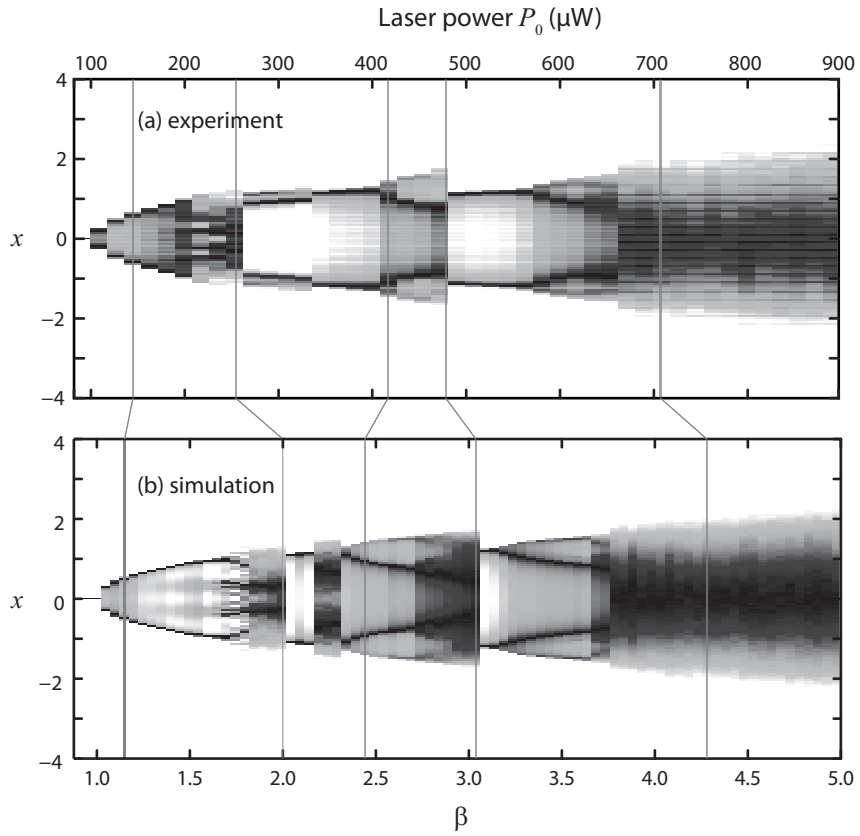

Figure 3.2: Bifurcation diagrams as the feedback strength is increased. (a) From experimental time traces for increasing laser power P_0. (b) From numerical time-series as the parameter β is increases. The vertical lines point to time-series that have matching behavior.

or apparent structure. Fig. 3.1(b) plots numerically integrated time-series (Eqs. (2.20) and (2.21)) for a series of feedback strength β, where each simulation was begun from random initial conditions and a long transient period was discarded. Each experimental trace is seen to have a numerical partner that shares its basic temporal features. We conclude that the model is adequate for representing the real system's behavior, and we may expect that analytical studies of the mathematical model will have real physical consequences.

The route to chaos is summarized with a bifurcation diagram. A histogram

of each time-series $x(t)$ is computed. The histograms are shown on a gray scale in Fig. 3.2. Each column is the histogram for a single parameter value (P_0 for experimental time-series in (a) and β for simulations in (b)). The black level corresponds to amplitudes that are visited often and the white level means that there are no counts for that bin. For $\beta < 1$, $x(t) \approx 0$ for all t, so the histogram has a delta-like peak. For $1 < \beta < 1.6$, the time-series are sinusoidal, spending the most time at the peaks and troughs. Thus these histograms have two strong peaks at $\pm x_0$. In fact, analysis of the model equations prove that there is a Hopf bifurcation at $\beta = 1$, with the periodicity related to ratio of the feedback delay τ to the lowpass time constant $\tau_2 = 1/(2\pi f_2)$ [2, 6]. For $\beta > 3.8$, the histograms show no preferential amplitude levels and resemble zero-mean Gaussian distributions.

For each experimental time-series, we find a matching region on the simulation bifurcation diagram (as indicted by the vertical lines on Fig. 3.2). However, the expected scaling $\beta \propto P_0$ does not hold. We must skew and stretch this relationship to match the shape of the bifurcation sequences. We infer that the numerical model is imperfect most likely due to the absence of ripple in the feedback gain frequency properties which exist in the experimental system. When the experimental time-series takes a form with strong peaks in the frequency spectrum, some peaks are subject to a greater amplification than others. So, the effective experimental feedback strength β_{eff} varies depending on the waveform dynamics. On the other hand, the numerical model assumes a unity gain for the filter throughout its pass band.

The spectral density of a time-series $x(t)$ is calculated by a fast Fourier transform (FFT) algorithm. For each of the time-series in Fig. 3.1, the corresponding

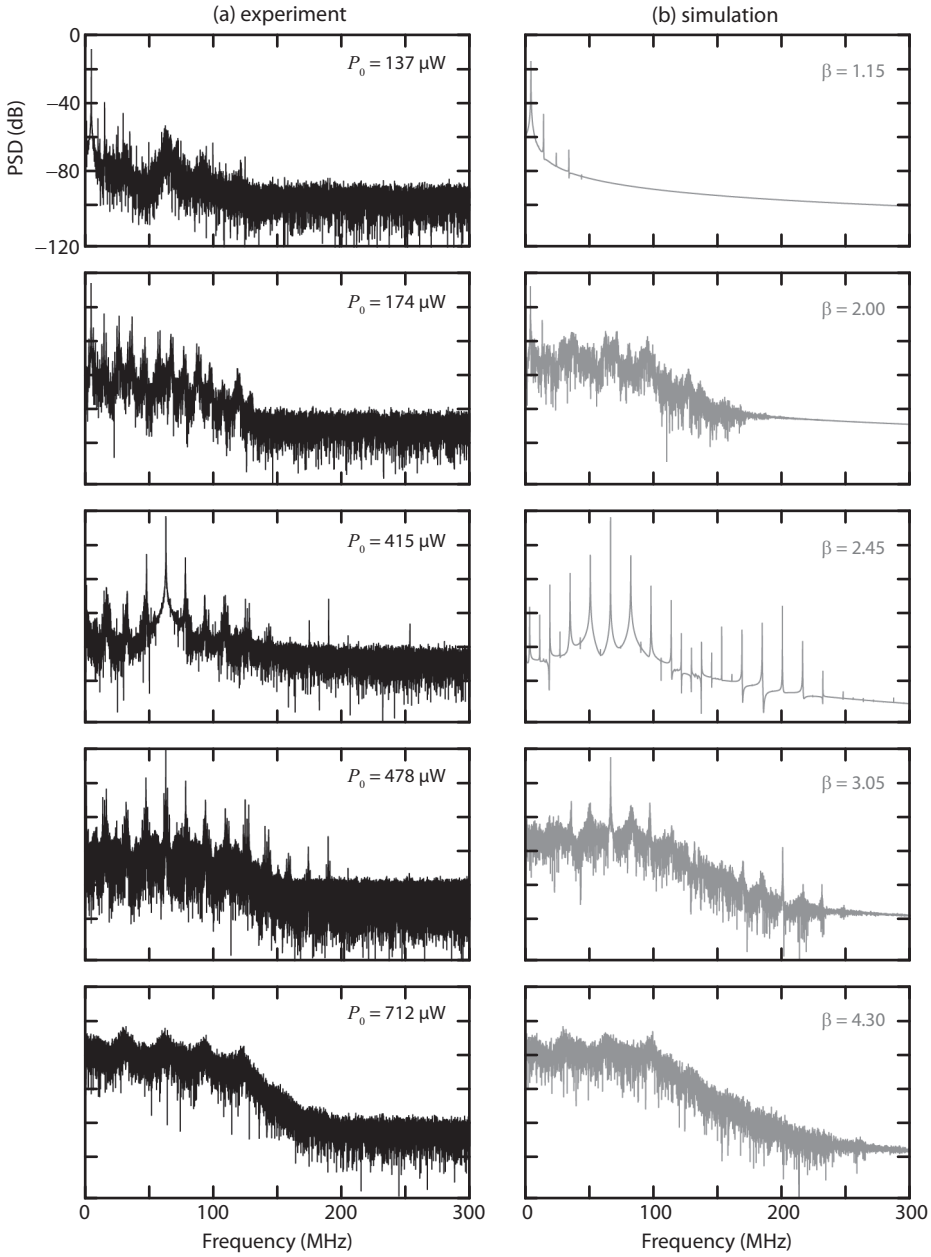

Figure 3.3: (a,b) Experimental (simulated) power spectral densities for a range of feedback strengths.

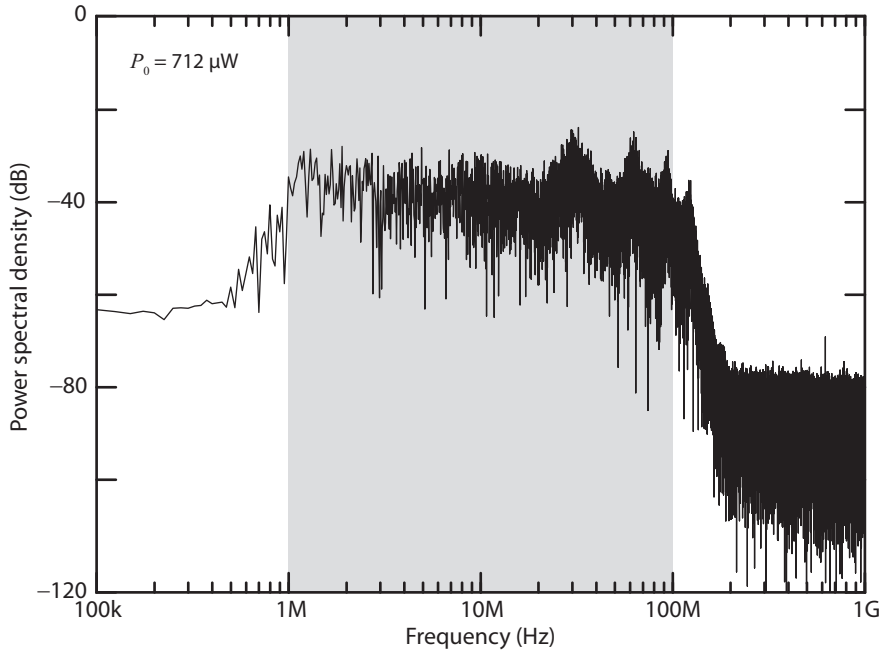

Figure 3.4: The PSD for $P_0 = 712$ μW has features of band-limited noise.

power spectral density (PSD) is plotted in Fig. 3.3. Again, we see an equivalence between the experimental and simulated spectral features. At low feedback strength, there are strong dominant peaks. As the feedback strength is increased, the noise floor rises up and eventually fills the entire pass band of 1–100 MHz. This is a signature that is often observed in a transition from non-chaotic to chaotic dynamics.

In Fig. 3.4, the PSD for $P_0 = 712$ μW is shown with a logarithmic frequency axis. This spectrum resembles white noise within the bandpass filter band with only a few dominant spectral modes. In Ref. [6], this property is systematically studied for the case when the modulator is biased at $\phi_0 = 0$ and with an ultra-wide band feedback channel spanning six orders of magnitude (10 kHz – 10 GHz). For this case, it is analytically derived that there remain no linearly stable periodic modes embedded within the dynamics.

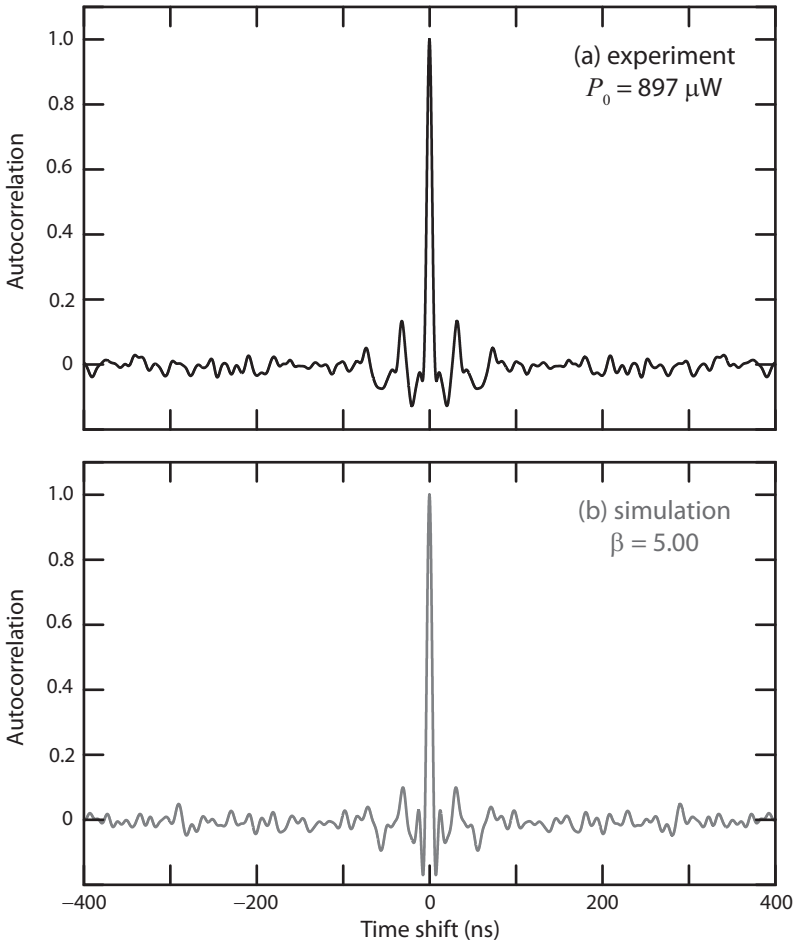

Figure 3.5: Autocorrelation functions for (a) experimental time-series with $P_0 = 897$ μW and (b) simulated time-series with $\beta = 5$.

An autocorrelation function (ACF) is used to diagnose periodic comb-like structures in a FFT. In Fig. 3.5, the ACFs of the experimental time-series with $P_0 = 897$ μW and the simulated time-series with $\beta = 5$ are displayed. These show remarkable agreement, including for the fine details near zero time-shift. Even for this relatively high feedback strength, it is evident that there is local structure in the dynamics within a window of about 50 ns. For true white noise lowpass filtered at 100 MHz, the correlation will decay around 10 ns. However, the ACF displays no long-term correlations, implying that the state has a short memory of about two

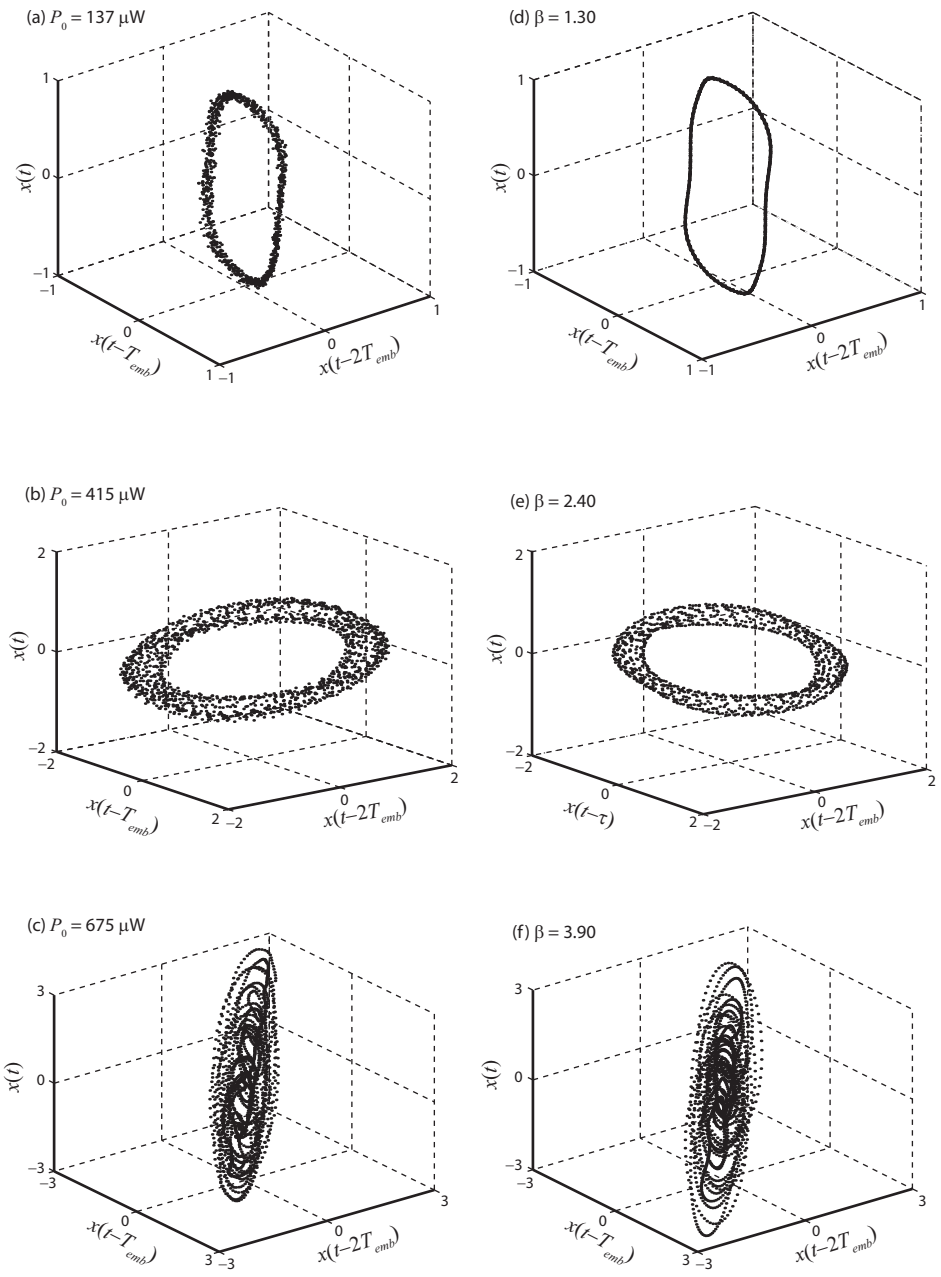

Figure 3.6: Time-delay embedding for experimental and simulated time-series. (a,d) $T_{\mathrm{emb}} = 20$ ns, (b,e) $T_{\mathrm{emb}} = 10$ ns, (c,f) $T_{\mathrm{emb}} = 1$ ns.

round-trips.

One way to find structure and temporal patterns within a scalar dynamical signal is with a time-delay embedding. We consider an orbit within a d-dimensional phase space made up of delayed coordinates: $(x(t), x(t-T_{\rm emb}), \ldots, x(t-(d-1)T_{\rm emb}))$. To view such a trajectory, we must look at a projection with $d = 3$. For periodic, quasiperiodic, or low-dimensional chaos, one can choose $T_{\rm emb}$ properly to reveal a geometric pattern that symbolizes the dynamics. For high-dimensional chaos, it may not be possible to find structure for any $T_{\rm emb}$ with a three dimensional embedding. In Fig. 3.6, we plot time-delay embeddings for three parameter values (three from experiment, three from simulation). For a periodic solution ($P_0 = 137$ μW), the embedding is a one dimensional limit cycle. For $P_0 = 415$ μW, we see a more complex shape. For $P_0 = 675$ μW, the orbit remains bounded in a region but does not conform to a specific shape.

In Figs. 3.1–3.6, we presented experimental measurements from a high-speed feedback loop and corresponding simulation results from iterating a continuous-time model. In particular, the route to chaos was examined as the feedback strength parameter β was increased while all other parameters (phase bias, time delay, and filter bandwidth) remained fixed. In general, one must repeat this procedure to encapsulate the bifurcation sequence while varying another parameter or for a different set of the fixed parameters. The measurements and numerics were also obtained for a slow-speed system which employed a DSP board to implement a time delay of $\tau = 1.5$ ms and digital bandpass filter with passband $(0.1, 2.5)$ kHz. This system exhibits a similar route to chaos, and its bifurcation diagram is presented in Refs.

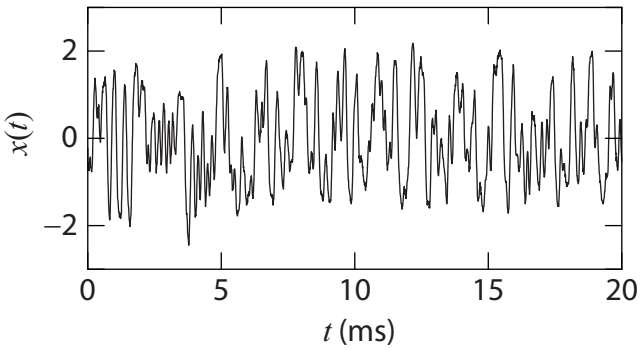

Figure 3.7: Chaotic time-series from DSP-based feedback loop.

[8] and [69]. In Fig. 3.7, we provide a representative time-series trace when the feedback strength β is tuned high enough to be in a regime of robust chaos. The time-scales involved are in the tens of μs to tens of ms range. This is the region of parameter space where experiments on adaptive synchronization (Chapter 6) and optimal synchronization (Chapter 7) were performed. In Ref. [8], the dynamical complexity was quantified at the time delay τ was varied while the feedback strength was fixed. In Ref. [6], the system behavior was systematically studied as the bias parameter ϕ_0 was varied.

3.2 Measures of complexity

3.2.1 Maximal Lyapunov exponent

The maximal Lyapunov exponent (MLE) h_1 is the average growth rate of the separation between nearby trajectories in phase space. For non-chaotic attractors, h_1 is negative or zero since two nearby initial conditions will either converge or maintain the same distance. For a chaotic attractor, two initial conditions diverge

from one another exponentially fast, so h_1 is positive. The inverse of h_1 is called the Lyapunov time and is a measure of the average time-scale for which an observed trajectory will realistically predict the behavior of its original phase space neighbors. For low-dimensional chaos, the MLE can be estimated from a measured scalar time-series [70, 71]. These schemes involve constructing a phase-space of delay coordinates and finding the average rate at which nearest neighbors diverge. This time-series analysis method fails for high-dimensional chaos, because a finite length time-series will include few nearby phase-space points. The conventional method for estimation of an MLE involves integration of a linearized numerical model [72]. In this Section, we outline this technique. In Chapter 4, we introduce a new way to estimate MLEs that uses a hybrid of experimental time-series and nonlinear numerical modeling. In principle, this new method could be applied in situations where there is no numerical model but two systems can be synchronized.

Consider a continuous-time dynamical system given by the evolution equation

$$\frac{d\mathbf{z}}{dt} = \mathbf{F}(\mathbf{z}). \tag{3.1}$$

Our goal is to determine how points nearby to $\mathbf{z}$ at time t diverge as t increases. We perform a linearization about the solution $\mathbf{z}(t)$ to see how a linear perturbation $\delta\mathbf{z}(t)$ grows or decays:

$$\frac{d\delta\mathbf{z}}{dt} = D\mathbf{F}(\mathbf{z})\delta\mathbf{z}, \tag{3.2}$$

where $D\mathbf{F}$ is the Jacobian of $\mathbf{F}$ evaluated along the trajectory $\mathbf{z}(t)$. For a chaotic trajectory, we expect $|\delta\mathbf{z}| \sim e^{+h_1 t}$, and thus keep track of the growth rate as:

$$h_1 = (t)\frac{1}{t}\ln\frac{|\delta\mathbf{z}(t)|}{|\delta\mathbf{z}(0)|}. \tag{3.3}$$

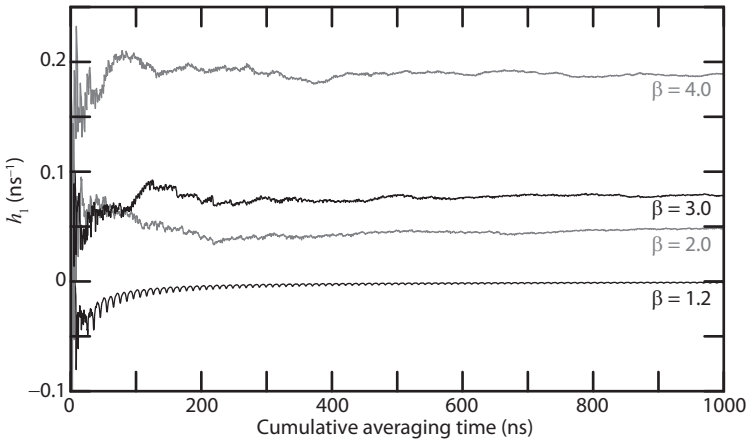

Figure 3.8: Maximal Lyapunov exponent computation. After an initial transient period, the computation settles to provide a good estimate of h_1.

Since Eq. (3.2) is linear, we choose the initial length as $|\delta\mathbf{z}(0)| = 1$ without loss of generality. Since the growth rate is exponential, $|\delta\mathbf{z}(t)|$ may overflow, so we periodically renormalize the growth vector and track the growth factor

$$\alpha_j = |\delta\mathbf{z}(t_j)|, \tag{3.4}$$

where $t_j = j\Delta t$ and $\delta\mathbf{z}(t_j) \to \delta\mathbf{z}(t_j)/\alpha_j$. By running the simulation for a long time, $\mathbf{z}(t)$ will visit all regions of the attractor, and thus

$$h_1 = \frac{1}{\Delta t}\langle \ln \alpha_j \rangle \tag{3.5}$$

is a good estimate for the global MLE [73].

The delay differential equations that model the optoelectronic feedback loop are

$$\frac{d\mathbf{u}(t)}{dt} = \mathbf{A}\mathbf{u}(t) - \mathbf{B}\beta\cos^2[x(t-\tau)+\phi_0], \tag{3.6}$$

$$x(t) = \mathbf{C}\mathbf{u}(t). \tag{3.7}$$

To solve these equations numerically, the system is iterated with a time step dt, so

that the solution is available only at discrete points in time as $\mathbf{u}(j \cdot dt)$ and $x(j \cdot dt)$. The variational equations are:

$$\frac{d\delta\mathbf{u}(t)}{dt} = \mathbf{A}\delta\mathbf{u}(t) + \mathbf{B}\beta \sin 2[x(t-\tau) + \phi_0]\delta x(t-\tau), \tag{3.8}$$

$$\delta x(t) = \mathbf{C}\delta\mathbf{u}(t), \tag{3.9}$$

which are conditional upon the solution $x(t)$. The state of the variational mode at time t conditional to the state $x(t)$ is

$$\delta\mathbf{z}(t) = \begin{pmatrix} \delta\mathbf{u}(t) \\ \delta x(t-dt) \\ \delta x(t-2dt) \\ \vdots \\ \delta x(t-\tau) \end{pmatrix} \tag{3.10}$$

which has dimensionality $14 + \tau/dt - 1$ where 14 is the order of the bandpass filter and thus the linearized state space vector $\delta\mathbf{u}$. Note that for this computation, one must choose the time step dt to be a fraction of the round-trip delay τ. In the same manner as described above, we compute the phase space growth as $|\delta\mathbf{z}(t)|$ to determine the MLE h_1 ($|\bullet|$ is the Euclidean norm).

In Fig. 3.8, we plot the growth rate h_1 for different feedback strengths β as the cumulative averaging time increases. After an initial transient period, the averaging settles to give a good estimate of h_1. The first 1 μs is plotted, but the full calculation was performed by averaging over a total time of 10 μs.

In Fig. 3.9, we plot the calculated h_1 as a function of β. At $\beta \sim 4$, the MLE is around 0.02 ns^{-1}, which implies a prediction horizon time of about 50 ns or just

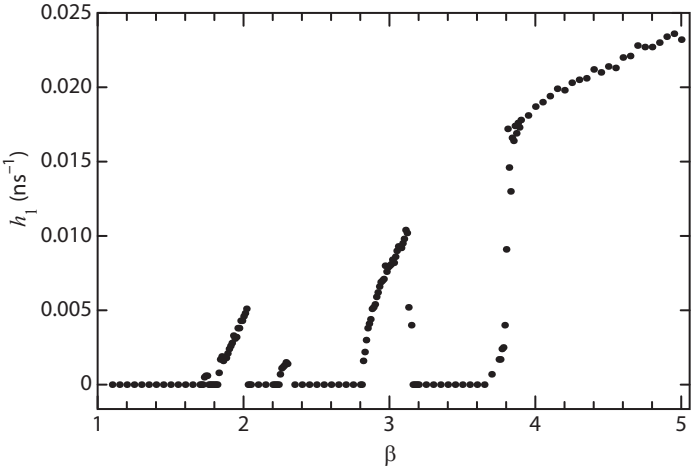

Figure 3.9: Maximal Lyapunov exponent computed for increasing feedback strengths.

over two round-trips.

3.2.2 Spectrum of Lyapunov exponents

At each point **z** along a chaotic orbit within its d-dimensional attractor, one can find an orthonormal basis whose vectors are ranked in terms of their rates of phase space expansion. The directions and growth rates vary throughout the attractor, but the ranked set of average growth rates $h_1 \geq h_2 \geq \cdots \geq h_d$ – called the spectrum of Lyapunov exponents (LEs) – is useful for estimating fractal dimension of a chaotic attractor with the Kaplan-Yorke formula and for estimating the Kolmogorov-Sinai entropy rate [73]. For chaotic motion, the largest Lyapunov exponent of this set, is positive and strongly dominates all measures of phase space growth. Hence, h_1 is the suitable metric for quantifying a system's predictability. The sign of an LE h_k determines if a small perturbation along a particular phase space direction will grow or decay. The number of positive LEs is a metric for chaoticity; a system with

at least two positive LEs is termed hyperchaotic.

To numerically calculate the spectrum of LEs from a linearized model (Eq. (3.10)), one considers d variational equations

$$\frac{d\delta\mathbf{z}_k}{dt} = D\mathbf{F}(\mathbf{z})\delta\mathbf{z}_k, \tag{3.11}$$

$k = 1, 2, \ldots, d$, where the $\delta\mathbf{z}_k$'s are initially chosen to be orthonormal vectors $\delta\mathbf{z}_k(0) \cdot \delta\mathbf{z}_\ell(0) = 0$. The set of starting states is typically chosen as

$$\delta\mathbf{Z}(0) = \begin{bmatrix} \delta\mathbf{z}_1(0) & \delta\mathbf{z}_2(0) & \cdots & \delta\mathbf{z}_d(0) \end{bmatrix} = \mathbf{I}_d \tag{3.12}$$

where $\mathbf{I}_d$ is the identity matrix. After iterating these conditional states to a time t, one finds that each of the $\delta\mathbf{z}_k$(t)'s aligns along the direction associated with maximal expansion. To obtain d independent growth rates with each corresponding to a unique direction at each point in phase space, one must eliminate the role of this preferential mode. Periodically, at time $t_j = j\Delta t$, one performs a Gram-Schmidt or QR decomposition procedure on $\delta\mathbf{Z}(t_j)$ to maintain orthogonality [73]. These routines also normalize the vectors to unity length and thus automatically provide the growth rates $\alpha_j^{(k)}$. After running the program for a long time, one calculates the d LEs as

$$h_k = \frac{1}{\Delta t}\langle \ln \alpha_j^{(k)} \rangle_j. \tag{3.13}$$

In Ref. [74], a method based on experimental time-series analysis is presented for extracting the spectrum of LEs. However, for a system with many positive LEs, we have found this computation is inaccurate and often unsuccessful.

For a time-delay system, the spectrum of LEs follows much the same procedure as for the MLE computation, by defining a phase space in terms of delay coordinates.

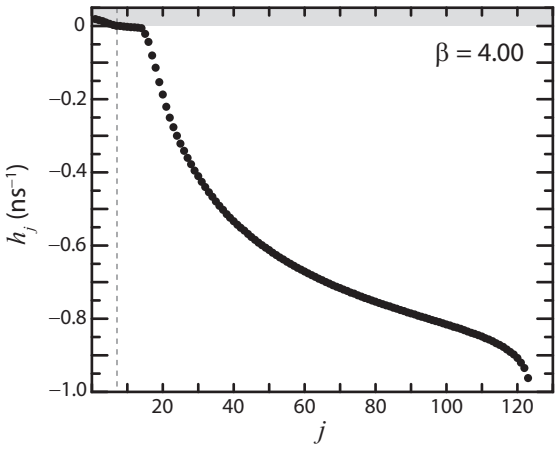

Figure 3.10: Lyapunov spectrum for $\beta = 4$.

This method was first advanced by Farmer who tested it with the Mackey-Glass differential equations [23]. We note that for a phase space that goes as $d \sim \tau/dt$, where τ is the physical delay and dt is the numerical time step, performing an orthonormalization on a $d \times d$ matrix every $\Delta t/dt$ time steps is a computationally expensive exercise. QR decomposition is found to be more efficient at this task than Gram-Schmidt orthogonalization [75].

In Fig. 3.10, we plot the Lyapunov spectrum for the DDEs modeling as opto-electronic feedback loop with $\beta = 4$. For this computation, $dt = \tau/113 = 0.1987$ ns and $\tau = 22.45$ ns, so the phase space dimension is $d = 14 + 113 - 1 = 126$. For these parameters, there are seven positive LEs with an MLE of $+0.0187$ ns^{-1}.

3.2.3 Lyapunov dimension

The fractal dimension is a quantitative characterization of the geometric structure of a complex orbit. Further, it provides a lower bound on the number of scalar variables required to construct a system of equations that models an observed dy-

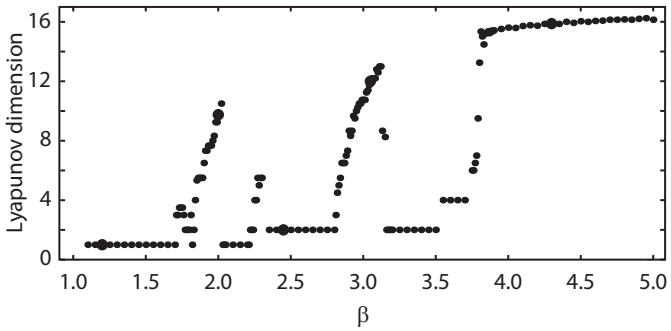

Figure 3.11: Calculated Lyapunov dimension D_{L} as a function of feedback strength β

namical process [73]. For a delay system, for which an artificially large phase space is formed by sampling a set of delay coordinates, the fractal dimension can be useful for optimally selecting an efficient data set that encapsulates all the essential dynamical features.

The Kaplan-Yorke conjecture associates the spectrum of LEs with fractal dimension [73]. In other words, a set of dynamical quantities ($\{h_j\}$) that measures sensitivity to initial conditions is also seen to relate to topologic measures. After directly computing or estimating via time-series analysis the h_j's, the Lyapunov dimension is calculated as

$$D_{\mathrm{L}} = K + \frac{1}{|h_{K+1}|}\sum_{j=1}^{K} h_j \tag{3.14}$$

where the h_j's are sorted in descending order and K is the largest integer for which

$$\sum_{j=1}^{K} h_j \geq 0. \tag{3.15}$$

In Fig. 3.11, the Lyapunov dimension D_{L} is plotted for the optoelectronic feedback loop as a function of the feedback strength β. The dimensionality has windows in the parameter β in which the complexity within phase space shoots up

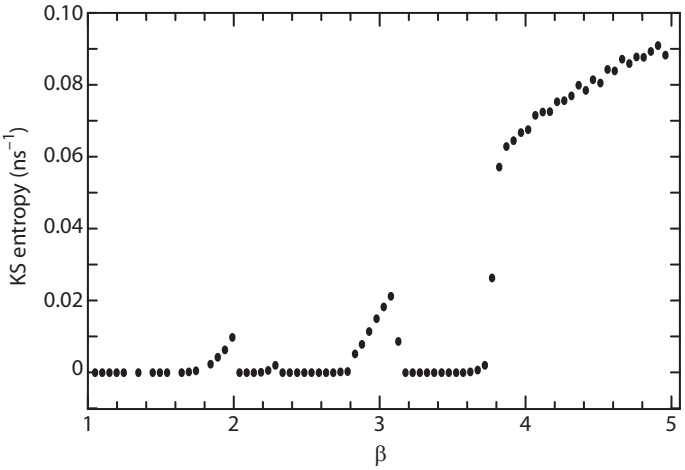

Figure 3.12: Calculated KS entropy as a function of feedback strength β.

($1.7 \geq \beta \geq 1.8$, $2.8 \geq \beta \geq 3.1$). For $\beta \geq 4$, the dimensionality saturates at 16–17, even though 126 phase space axes where used for the computation.

It is observed that Lyapunov dimension for many time delay systems increases directly with the time delay parameter, i.e $D_{\mathrm{L}} \propto \tau$ [23]. Computations for the discrete-time delay map equations (Eqs. 2.23) show that this is indeed the case for the optoelectronic feedback loop. The results for τ spanning an order of magnitude is presented in Ref. [8].

3.2.4 Kolmogorov-Sinai entropy

Entropy is another quantity, like the MLE, that serves to quantify chaos. The Kolmogorov-Sinai (KS) entropy estimates the average rate of information creation by an evolving orbit $\mathbf{z}(t)$. The essence of chaos is the amplification of microscopic uncertainty or noise to the macro level. A practically undetectable perturbation $\delta\mathbf{z}(0)$ displaces an orbit as $\mathbf{z}_1(t) \to \mathbf{z}_2(t)$, and thus a small amount of information

$\delta\mathbf{z}(0)$ evolves into a finite set of information $(\mathbf{z}_2(t) - \mathbf{z}_1(t))$. From this description, it is seen that KS entropy is intimately related to the LEs – the rate at which trajectories diverge. The estimate for the KS entropy rate is

$$h_{\mathrm{KS}} = \sum_{\{h_j > 0\}} h_j, \tag{3.16}$$

i.e. that sum of only the positive LEs [73].

In Fig. 3.12, we plot the KS entropy for the optoelectronic feedback loop. For non-chaotic dynamics, there are no positive LEs, and hence no information is created as time progresses. In the fully chaotic regime, the KS entropy increases to 1/(11 ns), signifying that the information expands by a fold of e every 11 ns.

KS entropy may be an important measure in the burgeoning field of random number generation using high speed chaotic sources [7, 76, 77]. If the KS rate is fast compared to the sampling rate, then a deterministic chaotic signal may have some statistical properties of randomness. In fact, by threshold detecting the output of some chaos generators, the resultant bit sequence can pass stringent tests for randomness [7]. KS entropy may find use as a gauge for estimating how random-like a given chaotic signal is. Unlike a true random source, which is quantum mechanical in nature, the unpredictability of chaos is not fundamental – the state is not a probabilistic wavefunction that collapses upon measurement but one that is uniquely defined and completely governed by deterministic (and perhaps stochastic) rules in which small inaccuracies compound to make the state hard to predict in practice.

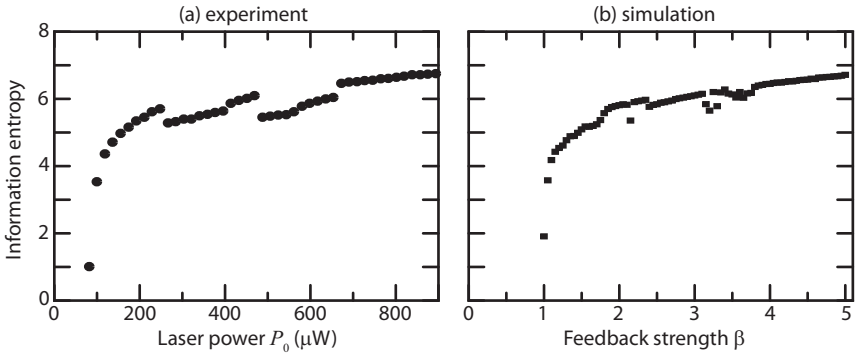

Figure 3.13: Shannon entropy H_{S} as a function of feedback strength from (a) experimental time-series and (b) numerically simulated time-series.

3.2.5 Information entropy

Shannon entropy H_{S} is a basic information theoretic quantity that measures the uncertainty associated with a sequence of numbers [78]. H_{S} is usually measured in bits, and a more complex sequence necessarily requires more bits, with a lower bound given by H_{S}, to encode its patterns. From a scalar time-series $x(t)$, one can compute a probability mass function of amplitude values $P(x_b)$ where x_b is a bin for which $P(x_b)$ counts all instances of $x(t)$ that fall within $(x_b - \Delta x_b/2, x_b + \Delta x_b/2)$. $P(x_b)$ is a normalized histogram (as represented as a gray scale image in the bifurcation diagrams above, Fig. 3.2) such that $\sum_b P(x_b) = 1$. The Shannon entropy is

$$H_{\mathrm{S}} = -\sum_b P(x_b) \log_2 P(x_b). \tag{3.17}$$

H_{S} is plotted as a function of feedback strength β in Fig. 3.13. In (a), the same experimental time-series used to draw the experimental bifurcation diagram are used. In (b), we plot the Shannon entropy obtained from examining simulated time series. The chaotic time-series have $H_{\mathrm{S}} \sim 7$ bits.

Information theory finds a place in nonlinear dynamics in terms of a set of statistical tools that impart how information is shared and transferred among the myriad variables of a dynamical systems, especially networks of coupled chaotic oscillators. Mutual information [78] and Schrieber's transfer entropy formulation [79] are tools that are applicable to diagnosing connectivity strengths and directionality of causality between interacting nodes even when there is little knowledge of the underlying physical processes [80, 81].

3.3 Summary

1. The optoelectronic feedback loop exhibits a wide range of dynamical behaviors as the feedback strength is varied for a fixed time delay.

2. Above a critical feedback strength, the system outputs a robust hyperchaotic signal.

3. A numerical model based on delay differential equations shows excellent agreement with experimental observations.

4. The spectrum of Lyapunov exponents provide a quantitative description of chaotic behavior, including measures of predictability, dimensionality, and the rate of information creation.

5. Well-controlled experiments on the complexity, predictability, and synchronizability of this prototype time-delay system can provide insights into a large class of dynamical systems.

Chapter 4

Using synchronization for time-series prediction

In the preceding two chapters, it has been asserted that numerical simulations can be made to realistically mimic the observed bifurcation sequence of an opto-electronic feedback loop oscillator and analysis provides insights into the underlying dynamical complexity. Synchronization is a bridge that merges the overlapping approaches of experimentation, simulation, and analysis for powerful and practical applications. Using synchronization, we can finely tune simulation parameters to match experimental settings, precisely set the current state, and make accurate forecasts of future yet unobserved states. In this Chapter, we present a method that drives a computer model into synchrony with a recorded oscilloscope time trace by detecting the proper system parameters and constructing the full multidimensional state from only the observed scalar variable. After a complete oscilloscope acquisition data stream is injected into the model, the reconstructed state can be used as an initial condition for an independently run model. The model is designed to predict the next states of the real experimental system. By comparing the real output with predictions, we measure as the error increases and the solutions diverge. A wide distribution of divergence rates implies that predictability varies throughout a chaotic attractor with some initial conditions more amenable to predictions than others. This experiment-to-simulation synchronization method quantifies local

predictability within a specific phase space region of interest, namely the current location. This method relies on a mathematical model standing in as a numerical replica of a second dynamical system. We also show that a secondary experimental feedback loop can predict the time evolution of a primary loop. Hence, experiment-to-experiment synchrony is used to make predictions even when no mathematical model is available.

4.1 Open loop synchronization

For a given set of system parameters, a long time-series $V_1(t)$ is recorded on a high-speed digital oscilloscope. The data sequence is obtained by an 8-bit analog-to-digital converter at the oscilloscope's input. Thus the signal is sampled as $V_1(n \cdot T_S)$ where $T_\mathrm{s} = 1/f_\mathrm{s}$ is the sampling interval and with a finite resolution quantized into 256 discrete voltage levels. Only a subset of the 256 levels are occupied, yielding a more realistic resolution of about 7 bits. Furthermore, the samples $V_1(n \cdot T_s)$ include not only the desired dynamical signal but also a superposition of additive analog noise terms, which encompass 5 to 10 percent of the records, with the noise amplitude growing with oscilloscope bandwidth. It is a challenge to incorporate these limited and noisy observations into a numerical model.

For the experimental time-series presented in Chapter 3, the sampling rate was $T_\mathrm{s} = 0.1$ ns and the total record length was 50 μs. The numerical simulation were run with a time step of $dt = 0.005$ ns with a fifth-order fixed step Dormand-Prince DDE solver. When the oscilloscope time-series are read into the computer, the data

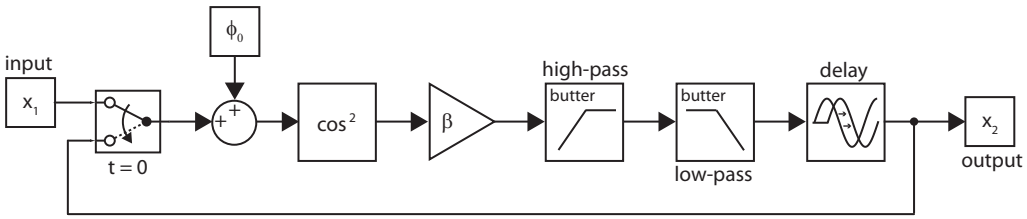

Figure 4.1: Simulink block diagram for open loop synchronization and time series prediction.

is first averaged with a boxcar moving average with a window of 0.4 ns to eliminate high frequency fluctuations outside the dynamical bandwidth. The voltages V_1 are then scaled by $\pi/(2V_\pi)$ to form the dimensionless variable x_1. The next step for incorporating x_1 into a numerical model is interpolating between the samples to estimate the signal at all the model mesh points: $x_1(n \cdot T_s) \rightarrow x_1(n \cdot dt)$ (following a spline interpolation procedure).

To achieve open loop synchronization, the numerical model is iterated with the feedback term replaced with the experimental measurement variable $x_1(n \cdot dt)$. In terms of continuous-time DDEs, the driven model equations are

$$\frac{d\mathbf{u}_2(t)}{dt} = \mathbf{A}\mathbf{u}_2(t) - \beta\mathbf{B}\cos^2[x_1(t-\tau)+\phi_0] \quad (4.1)$$

$$x_2(t) = \mathbf{C}\mathbf{u}_2(t) \quad (4.2)$$

where $\mathbf{u}_2(t)$ is the model's state and $x_2(t)$ is the scalar model output equivalent to the experimentally observed signal. If the model was a perfect representation of the behavior of $x_1(t)$ and the parameter set $\{\mathbf{A}, \mathbf{B}, \mathbf{C}, \beta, \phi_0, \tau\}$ were chosen exactly, then the model would synchronize unconditionally after a transient period as $(x_2 - x_1) \rightarrow 0$. However, the model is inexact, the real parameters are unknown, and the input data is limited and noisy, so the best scenario is for $x_1 \approx x_2$ with a relatively small

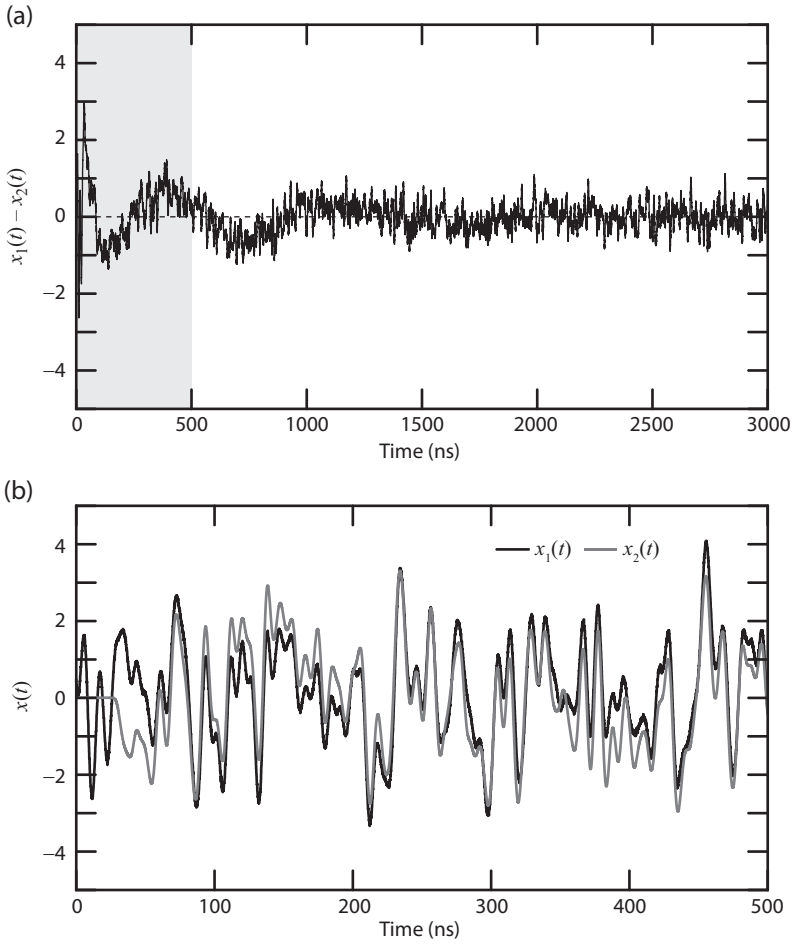

Figure 4.2: Open loop synchronization transient response. (a) $x_1(t)$ is the experimental time trace input into the model and $x_2(t)$ is the simulation output. (b) Synchronization error $x_1(t) - x_2(t)$ slowly damps at a time-scale determined by the bandpass filter.

synchronization floor $|x_1 - x_2|$.

Our numerical model is run within the Simulink environment, with its block diagram depicted in Fig. 4.1. Here, the boxcar averaged experimental input x_1 is input on the left hand side, and it subsequently undergoes the cosine-squared nonlinearity, a gain β, a bandpass filtering operation, and a time delay τ to form the simulation output x_2 on the right hand side.

Initially, the model state $\mathbf{u}_2(0)$ is chosen as a null vector. Hence, when the driv-

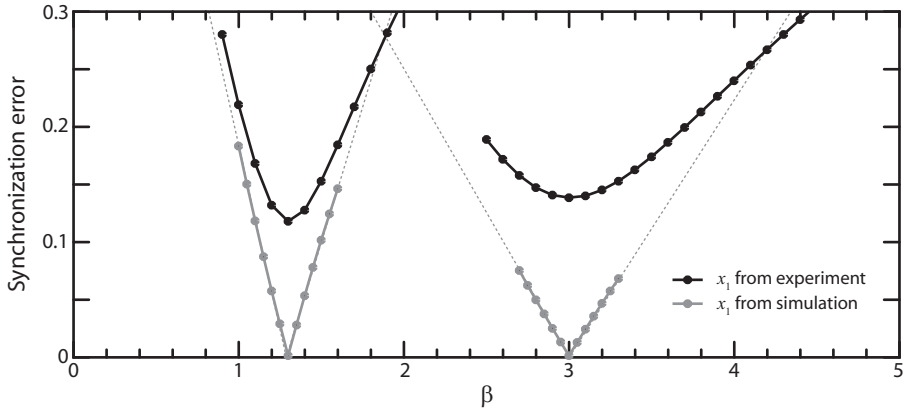

Figure 4.3: Open loop synchronization error as simulation feedback strength parameter is swept. The black curves are for two time-series taken with different laser powers $P_0 = 156$ μW (left) and $P_0 = 619$ μW (right). The gray curves are for two simulated time-series with $\beta = 1.3$ (left) and $\beta = 3.0$ (right). For this case, the synchronization error goes to zero for proper choice of β.

ing signal $x_1(t)$ causes a step-like response which rings down on a time-scale related to the highpass filter time constant. In Fig. 4.2(a), the difference $(x_1(t) - x_2(t))$ is plotted for the first 3 μs. The transient behavior closely resembles the step response of the 14th-order Butterworth bandpass filter (Fig. 2.9). After approximately 2 μs, the difference settles and open loop synchronization is achieved.

Synchronization error, a rms measure of the synchronization floor, provides a metric for the ability of the numerical model to reproduce the experimental sequence. To achieve the highest quality open loop synchronization, the parameters can be scanned to minimize the difference. As described in Chapter 2, the parameters for the filter and the delay are accurately known. The values for β and ϕ_0 are less certain, with knowledge of β being the least exact. In Fig. 4.3, we plot the synchronization error between experimental time series ($P_0 = 156$ μW, $P_0 = 619$ μW) and the simulation output as β is varied. There is a clear optimal value

β_{eff} for each data set ($\beta_{\text{eff}} = 1.3$, $\beta_{\text{eff}} = 3.0$). We emphasize that even though the experimental time traces are taken for incremental increases of laser power P_0 in uniform steps, we cannot maintain a linear scaling between P_0 and β_{eff} for the reasons outlined in §2.7. As the time-series are stepped through, it is seen that β_{eff} makes abrupt transitions as the dominant frequency modes shift, corroborating the analysis described in §3.1. When the experimental time-series $x_1(t)$ is replaced with a simulated time-series, for which this is an exact model, the minimum synchronization error goes to zero for the proper β value and rises linearly about the minimum. This feature is derived in Ref. [82] for open loop synchronization used in chaos communication [3]. In Ref. [83], a systematic procedure is developed for scanning an entire parameter space for optimal values for a possibly large set of parameters by minimizing a cost function.

In Fig. 4.2(b), we plot the first 500 ns after the experimental input has begun for the optimized feedback strength β_{eff}. After the initial transient period, the simulation output x_2 tracks the real data sequence x_1 to a remarkable degree. All the internal variables of the filter $\mathbf{u}_2$ have collapsed on to the real filter state which is unobserved. In summary, open loop synchronization allows us to efficiently assimilate a single scalar observed variable into a multidimensional model, reconstruct the time evolution of unobserved variables, and learn the optimal parameter values.

4.2 Time-series prediction

For each experimental time trace $x_1(t)$ recorded at a different laser power P_0, we find there is a feedback strength β_{eff} for which the simulation output becomes well-entrained to the experimental input, i.e. $x_2(t) \approx x_1(t)$. After open loop synchronization is achieved, the next step is to terminate the external drive signal to the simulation and to replace it with its internal copy. At a specific time, the feedback term is 'switched' from $-\beta \cos^2[x_1(t-\tau)+\phi_0]$ to $-\beta \cos^2[x_2(t-\tau)+\phi_0]$. We denote the switch time $t = 0$; however, we may perform the switch at any time. In practice, we choose the switch event to occur within time windows where the synchronization error $|x_1 - x_2|$ is relatively small. After $t = 0$, the simulation runs completely independently. In Fig. 4.1, the switch block represents the exchange of feedback variables at $t = 0$ in the Simulink simulation.

The simulation iterates $x_2(t)$ for $t > 0$ continue to track the real experimental observations. The model is able to predict states for which it does not directly have access, both in terms of the scalar output variable x_1 and the internal states $\mathbf{u}_1$. The term 'predict' is used somewhat loosely in that the real data has already been acquired and stored and the simulations do not necessarily run faster than real-time. Nevertheless, we regard this exercise is a proof-of-principle test of this simulation-prediction scheme.

For non-chaotic orbits, we expect that a closely entrained initial state will continue to track its driver even after the drive term has been discontinued. In Figs. 4.4 (a)–(f), we plot the pair of time-series $x_1(t)$ and $x_2(t)$ after $t = 0$. Indeed,

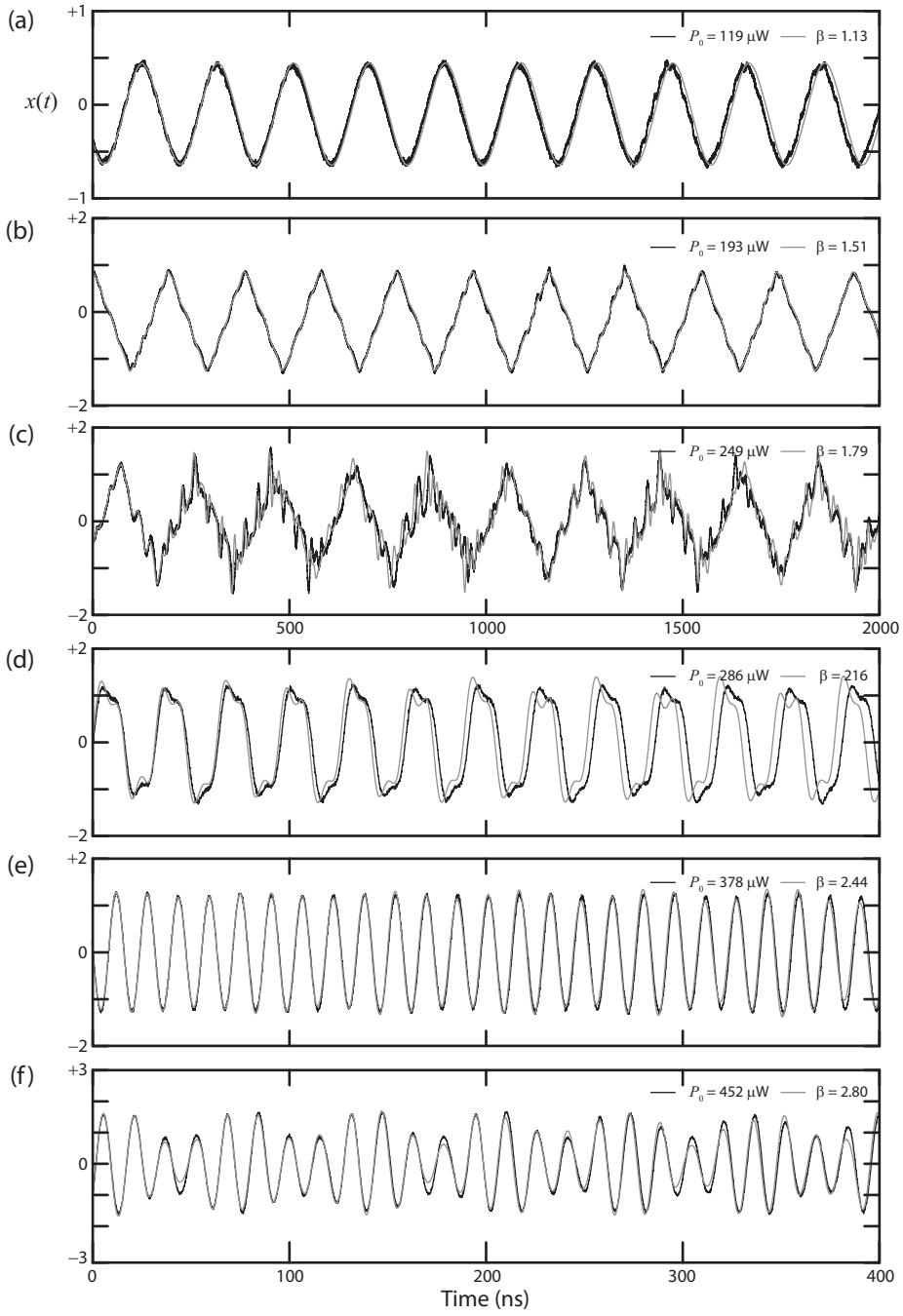

Figure 4.4: Time-series prediction for non-chaotic trajectories. For each panel, the black curve is the experimental time trace, and the gray curve is the output from the prediction model after the driving term has been terminated at $t = 0$. The laser power P_0 that each data was taken for and the simulation β parameter are labeled at the upper right of each panel.

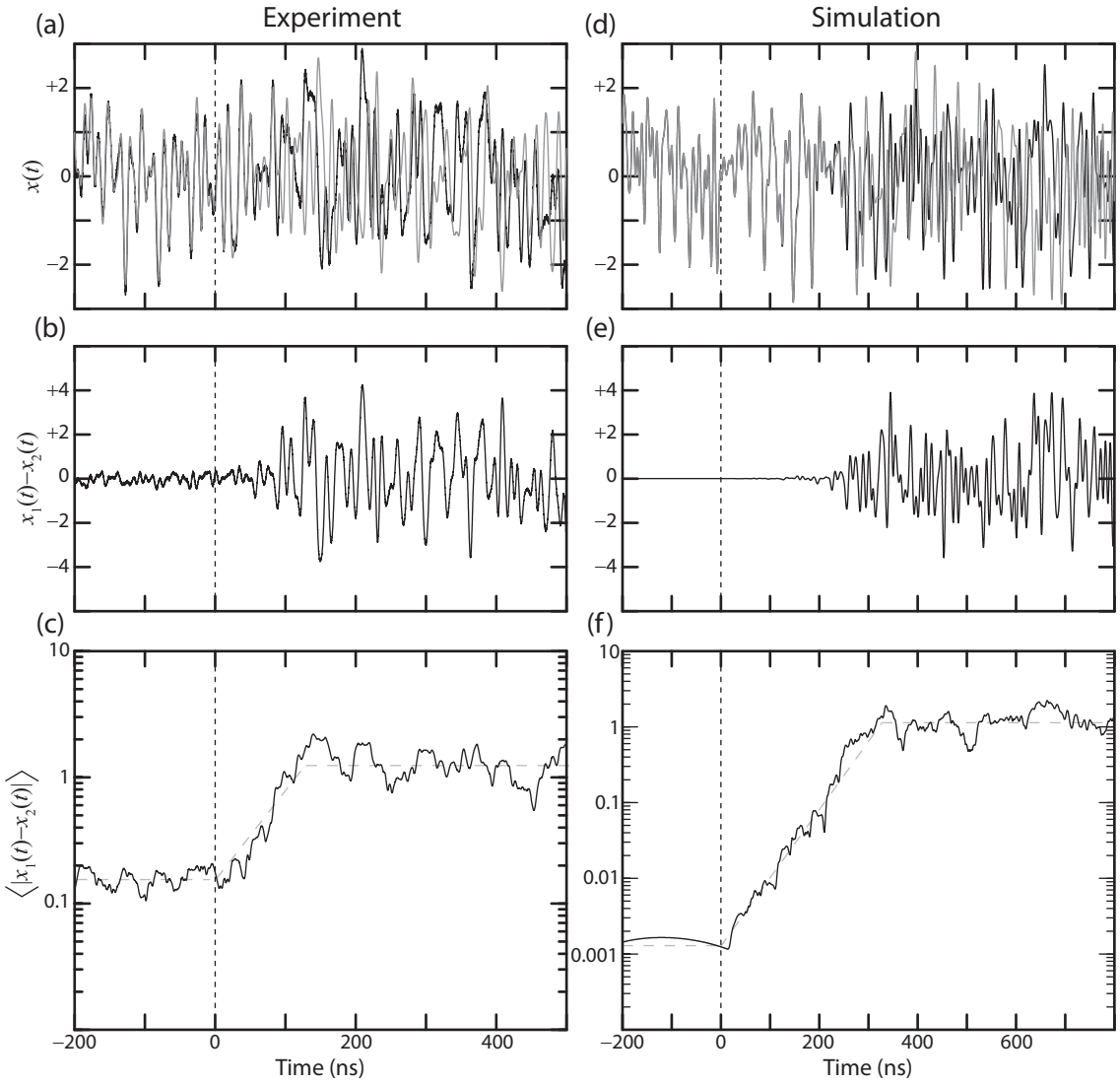

Figure 4.5: Time-series prediction for chaotic trajectories. (a) Results from experimental time-series $x_1(t)$. For $t < 0$, the model output $x_2(t)$ is driven by the input $x_1(t)$, and for $t > 0$, the model providing predictions. The difference grows remains small for $t < 0$ and grows exponentially for $t > 0$. (b) Corresponding results for $x_1(t)$ from simulation.

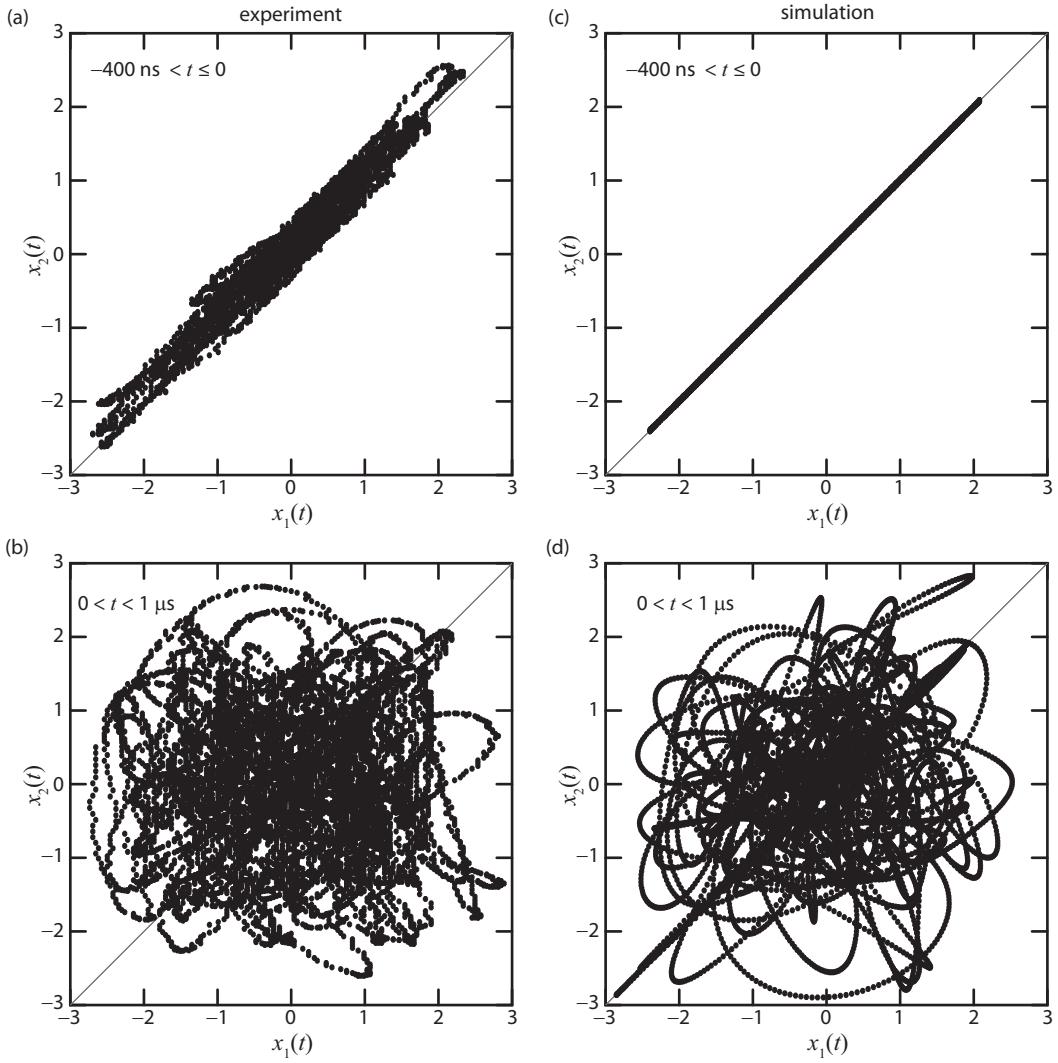

Figure 4.6: Synchronization plots during open loop synchronization and divergence. (a,c) $t < 0$, (b,d) $t > 0$.

the two trajectories in each plot remain closely aligned. However, it is evident that there is a loss of phase coherence which gradually develops as expected for slight parameter mismatches or an imperfect model.

For chaotic dynamics, the two initially nearby states at $t = 0$ must diverge. In the long term, $x_1(t)$ and $x_2(t)$ will lose any semblance of their shared history. In the short term, x_2 tracks x_1 but the trajectories quickly march away from one another. The size of the window with fairly matched evolutions is determined by how close the initial states at $t = 0$ are and the underlying chaotic dynamics, characterized by the MLE.

In Fig. 4.5(a), we plot the evolutions of x_1 and x_2 just before the switch and just after. Before $t = 0$, the time-series follow one another in lock-step. After, there is a definite window with $x_1 \approx x_2$. The difference $x_1 - x_2$, which is the synchronization error before $t = 0$, is the forecast error after $t = 0$. The forecast error initially remains small, but eventually it grows to have the same amplitude as x_1 and x_2 signifying that there is no longer any coherent evolution. In (b), the same numerical experiment is performed with the driving term $x_1(t)$ formed from a simulation. In this case, the initial synchrony can be reduced by many orders of magnitude. Even so, small errors in the initial state are still amplified. The prediction window is lengthened, but eventually x_1 and x_2 separate. The exponential rate at which the prediction window grows is a measure of the local Lyapunov exponent, which is the subject of the next section. Another way to picture the divergence of chaos is with synchronization plots $x_2(t)$ vs. $x_1(t)$. In Figs. 4.6 (a) and (c), x_2 vs. x_1 is plotted for $t < 0$. In (a), where the experimental realization is shown, the width of the

data points about the line $x_2 = x_1$ is a gauge of the synchronization error between experiment and simulation. In (c), where x_1 comes from simulation, the data fall almost exactly on the $x_2 = x_1$ line. In (b) and (d), the orbits are plotted for $t > 0$. In this case, there is an initial set of points along the synchronization line, but the majority of points fall far off the line.

4.3 Prediction horizon times and distribution of finite time Lyapunov exponents

The exponential rate of divergence between the signals $x_1(t)$ and $x_2(t)$ is an estimate of the local MLE h_1. The multiplicative inverse of h_1 is the characteristic time-scale for which we can make accurate prediction, called the prediction horizon time. For a diverging pair, we can extract the prediction horizon time by finding the best fit line on a plot of $\ln\langle|x_1 - x_2|\rangle$ where $\langle\bullet\rangle$ denotes a boxcar moving average with a window of length 25 ns which is performed to rid inaccuracies due to zero crossing in $x_1 - x_2$. In Fig. 4.5(a), the lower pane depicts this exponential divergence as a line with positive slope on a semilogarithmic axis. The fit is only performed on a finite time window T since the prediction error saturates when the solutions x_1 and x_2 are as far away as possible on the bound attractor. In this case, we fit from $t = 25$ ns to $t = 75$ ns. In the lower pane of (b), the divergence is plotted in the same manner for an example of simulation-simulation synchronization. In this case, the initial error is much smaller, so the solutions take longer to reach saturation. However, we make the linear fit over the same window to make a comparison with

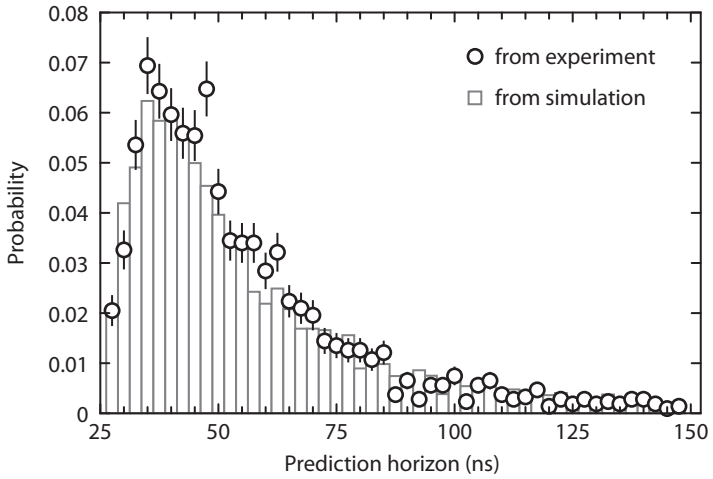

Figure 4.7: Distribution of prediction horizon times for $\beta = 4.0$. Results from using x_1 as an experimental time trace and a simulated time trace are compared.

the experiment-simulation results.

The same numerical exercise can be repeated many times by choosing the switch event as different points in the time-series $x_1(t)$. Both the initial error level and the rate of divergence varies for each trial. We study the distribution of divergence rates in more detail. In Fig. 4.7, we plot a histogram of prediction horizon times for $\beta_{\text{eff}} = 4.0$. For some trials, the experimental time-series can be reliably forecast for a period of greater than 100 ns or about four complete round-trips; while most initial states allow for forecasts of around 35 ns. The same computation was repeated with a simulation time-series for $x_1(t)$ and $\beta = \beta_{\text{eff}}$. The distributions of horizon times agree very well. We conclude that the statistics regarding predictability can be ascertained using the experiment-simulation synchronization method.

In simulation, we may vary the window T over which the exponential relation is fit. There is a well-known relationship between the width of the distribution of

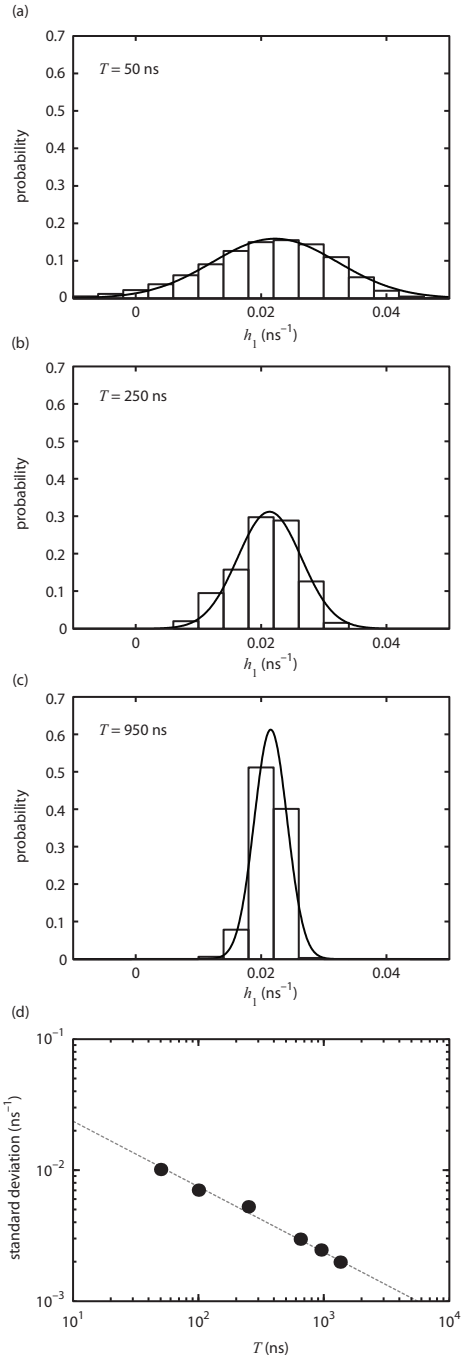

Figure 4.8: (a,b,c) Distributions of divergence rates for different fitting intervals T using continuous-time model. (d) Distribution width as a function of T.

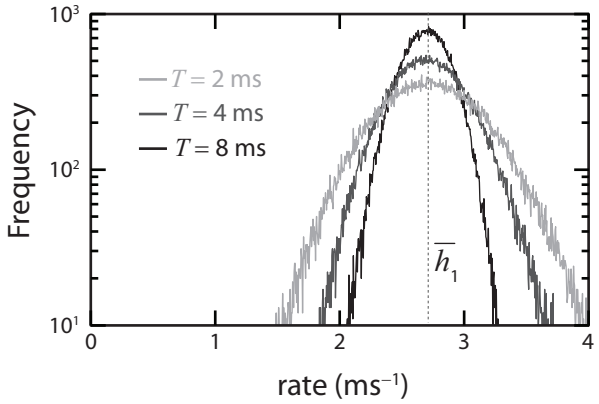

Figure 4.9: Distribution of divergence rates for different fitting intervals using discrete-time model.

finite-time Lyapunov exponents $P(h_1, T)$ and the fit time T. In particular, $P(h_1, T)$ follows a Gaussian distribution with a mean equal to the globally averaged MLE $\bar{h}_1$ and a standard deviation σ which goes as $1/\sqrt{T}$ [73]. In the limit $T \to \infty$, the distribution narrows to a delta peak at $h_1 = \bar{h}_1$. In effect, this means that the measurement is performed such that the trajectories x_1 and x_2 traverse all regions of the attractor. Structural effects of the chaotic attractor make the distribution deviate from the Gaussian shape in the tails far from $\bar{h}_1$. A comprehensive treatment of this feature is examined in Ref. [43, 84]. In Fig. 4.8 (a)–(c), we plot histograms $P(h_1, T)$ for fit time $T = 50$, 250 and 950 ns along with the best fit Gaussian. In (d), the standard deviation is plotted as a function T and the $\sigma \sim T^{-1/2}$ relationship is recovered.

The same sort of time-series based divergence rate evaluations were executed for the discrete-time map model (§2.11). In this case, the time-scales involved are orders of magnitude slower, in the ms rather than ns range. Here, the calculations are repeated 10^5 times. The distribution of $h_1 \sim \ln\langle|x_1[n] - x_2[n]|\rangle$ is plotted for different

time windows $T = (n_2 - n_1)/f_s$ in Fig. 4.9. The distributions $P(h_1, T)$ are displayed on a semilogarithmic scale, so a Gaussian function appears as a quadratic function. For these distributions, the deviations in the tails are evident. In Chapter 7, a similar method will be exploited to handle distributions of finite-time convergence rates for synchronizing networks upon enabling coupling.

4.4 Alternative methods for measuring phase space divergence from time-series

In the preceding section, an algorithm was introduced that estimates a local Lyapunov exponent by fitting an exponential curve $e^{+h_1 t}$ to the smoothed difference $\langle |x_1 - x_2| \rangle$. The conventional method for extraction of h_1 from the pair of divergence scalar variables x_1 and x_2 is to define a d-dimensional phase space of delay coordinates [85] for each variable as

$$\mathbf{X}_1(t) = \begin{bmatrix} x_1(t) \\ x_1(t - \Delta t) \\ x_1(t - 2\Delta t) \\ \cdots \\ x_1(t - (d-1)\Delta t) \end{bmatrix}, \; \mathbf{X}_2(t) = \begin{bmatrix} x_2(t) \\ x_2(t - \Delta t) \\ x_2(t - 2\Delta t) \\ \cdots \\ x_2(t - (d-1)\Delta t) \end{bmatrix},$$

and measuring the distance as $|\mathbf{X}_1(t) - \mathbf{X}_2(t)|$ where $|\bullet|$ is the Euclidean norm. For this measure, one must carefully select the time interval Δt and embedding dimension d. In this section, we compare the h_1's obtained from this delay embedding technique to the h_1's obtained from the smoothing technique of §4.3.

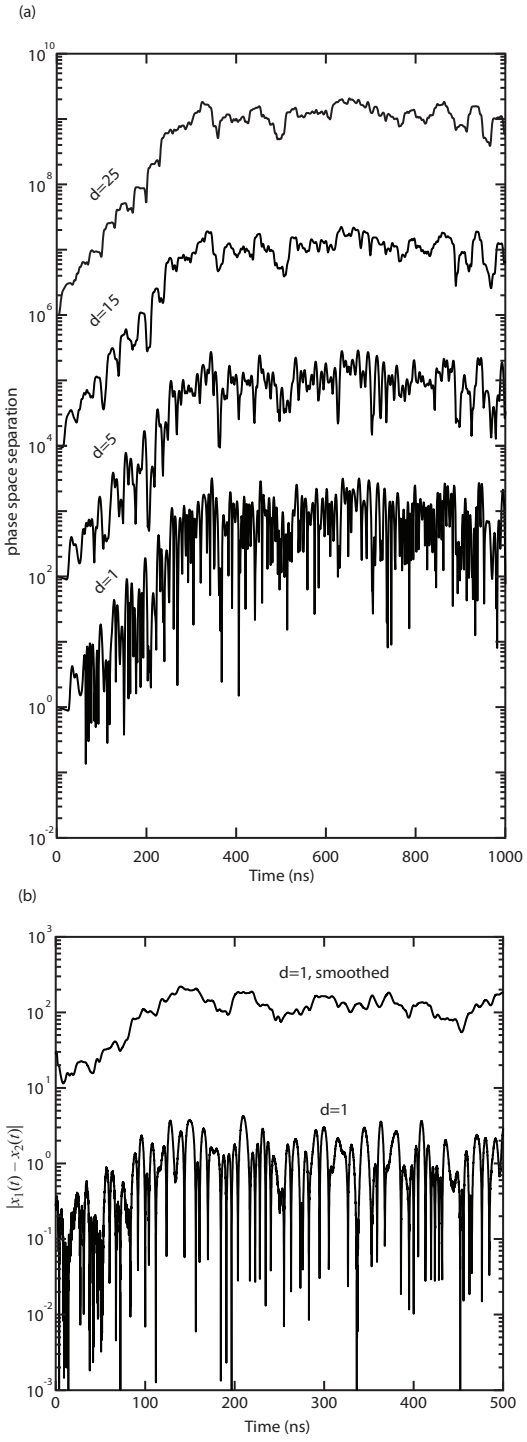

Figure 4.10: Extracting divergence rate h_1 from a pair of time-series $x_1(t)$ and $x_2(t)$. (a) Using d-dimensional phase space reconstruction with delay coordinates for d =1, 5, 15, and 25. (b) Comparison of $|x_1(t) - x_2(t)|$ with $\langle |x_1(t) - x_2(t)| \rangle$ where $\langle \bullet \rangle$ is a smoothing function with a window of $T = 25$ ns.

In Fig. 4.10(a), we plot the phase space distance as a function of time after the switch corresponding to two diverging time-series $x_1(t)$ and $x_2(t)$ from simulation. The interval Δt is chosen as 1 ns, and the distance is plotted for $d = 1$, 5, 15, and 25. Qualitatively, each of the traces have similar feature: a finite interval of exponential growth followed by saturation. However, for larger d, there are fewer dropouts due to $\mathbf{X}_1(t)$ being coincidentally near to $\mathbf{X}_2(t)$. The portions of linear growth on this logarithmic scale all have approximately the same slopes. Thus, each of these embeddings can be used to estimate h_1. In (b), we compare the divergence for $d = 1$ and for the smoothing method. Here, again, the slopes are approximately the same.

In Fig. 4.11, we compare the divergence rates for a series of simulation trials started from different initial states. In (b), a large fitting window of $T = 550$ ns is used and compared to using a $d = 25$ embedding. In this case, the rates agree almost exactly for each trial. In (a), a smaller fitting window of $T = 100$ ns is used. Here, there is some discrepancy between the measured rates. However, the rates are high correlated and agree on average.

From these examples, we conclude that these methods for measuring divergence properties agree on average. The smoothing method provides a good way to extract useful information from noisy experimental data.

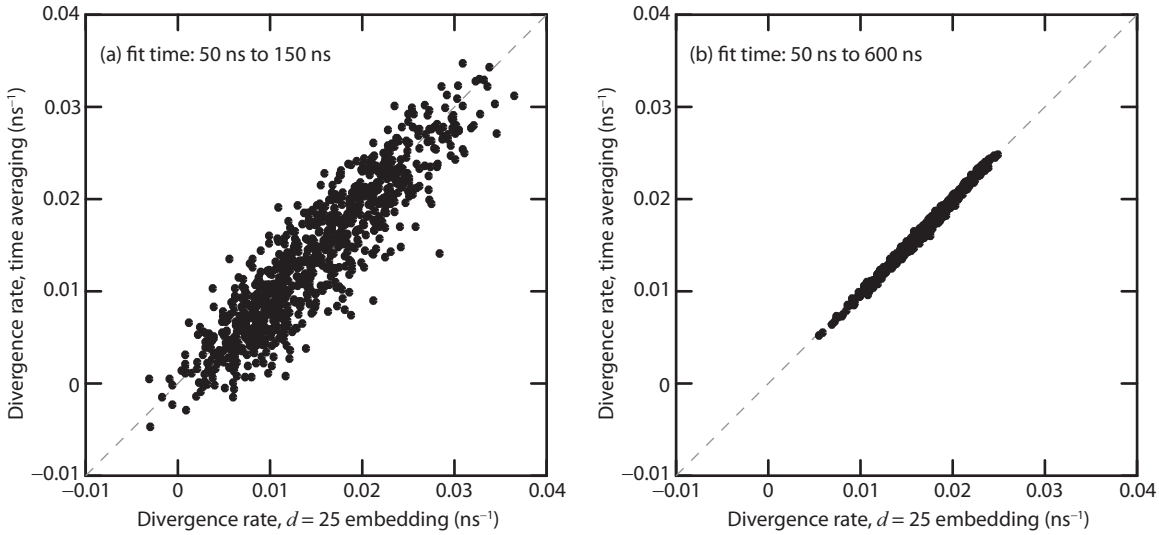

Figure 4.11: Comparison of extracted divergence rates h_1 using different methods. (a) Smoothing over 100 ns vs. a 25-dimensional delay phase space. (b) Smoothing over 550 ns vs. a 25-dimensional phase space.

4.5 Measured maximal Lyapunov exponents

The local LE h_1 for a pair of diverging trajectories measures the predictability in the region of phase space nearby to $(\mathbf{u}_2(t), x_2(t), x_2(t-\Delta t), \ldots, x_2(t-\tau))$. The distribution of local LEs $P(h_1, T)$ provides statistics regarding the variation of predictability throughout the entire attractor. The mean of the distribution $\bar{h}_1$ is an estimate of the global MLE – how initial conditions diverge on average. By repeating the synchronization-release experiment many times under different experimental conditions, we can measure the MLEs as a function of the feedback strength β. In Fig. 4.12, we plot the MLEs obtained through this hybrid experiment-simulation method along with the MLEs derives from direct computation of a linearized model (§3.2.1). The open circles are the estimates from $x_1(t)$ being an experimental time trace, and the open squares are from when $x_1(t)$ is a simulated time trace. All three

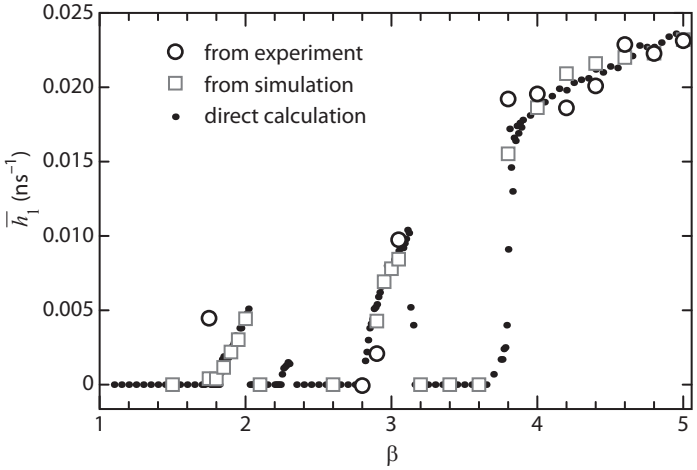

Figure 4.12: Average divergence rate $\bar{h}_1$ vs. feedback strength β.

sets of points overlap reasonably well. We conclude that this technique based on open loop synchronization is a new way to estimate global properties of a chaotic system. It attains an important balance between the application of real-world data streams and numerical modeling.

4.6 Prediction using a secondary experimental system

The routine described in this chapter can be applied even when there is no accurate numerical model for the chaotic dynamics under test. If two coupled systems can be forced into a synchronous state, then the properties of an isolated system's MLE can be experimentally measured. By synchronizing and subsequently interrupting the communication link, while simultaneously recording a scalar output variable from each system, the divergence rate can be extracted. By repeating this synchronization-then-release procedure many times, the measured distribution of h_1's can yield the global MLE $\bar{h}_1$ which characterized the underlying chaotic mo-

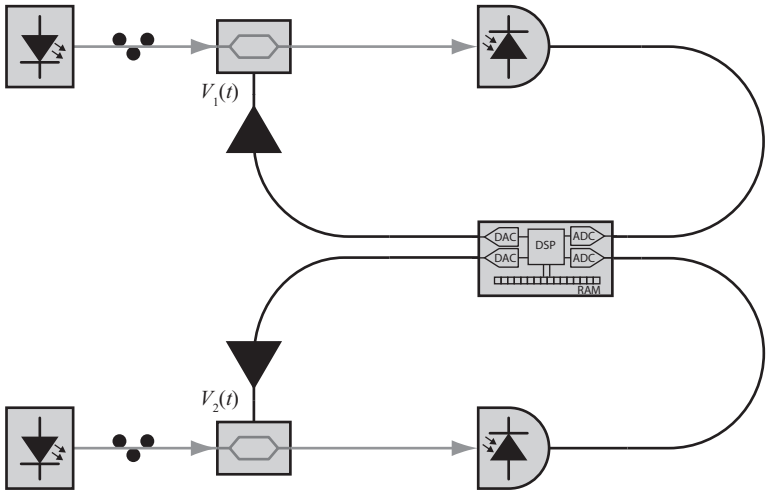

Figure 4.13: Schematic for synchronization-release experiment. The DSP board independently filters and delays the feedback signals for each loop, and it controls the coupling between the loops (strength and direction).

tion. For the proposed experiments, two nominally identical oscillators and a means to rapidly control the coupling flow are required. The coupling control can be in terms of a mechanical, an electronic, or an optical switch. The switching rate (the time-scale to go from enabled to disabled) must be fast compared to the chaotic dynamics. For example, using two high-speed analog optoelectronic feedback loops, an optical or electronic switch must toggle between on and off in a fraction of a nanosecond.

Fig. 4.13 is an experimental schematic that realizes two-node MLE-measurement task. Here, a single DSP board performs a digital filtering operation and imposes a time delay on the feedback signals for each oscillator, as described in §2.11. The ADC and DAC have two independent input and output channels respectively. The coupling from x_1 to x_2 and vice versa is fully controlled by the DSP program. At a specified sample time, the coupling terms can be immediately enabled or disabled.

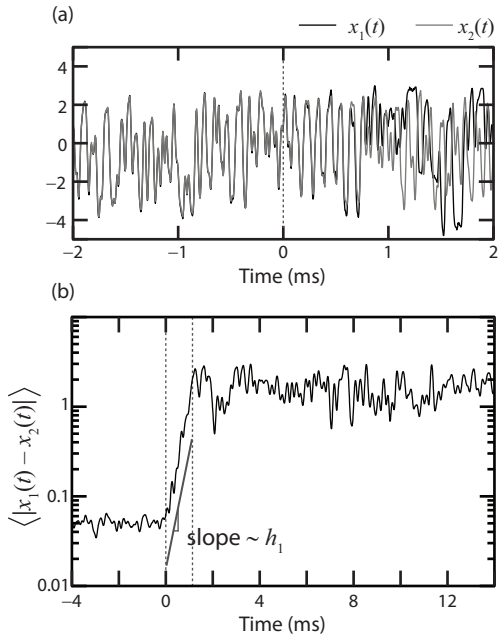

Figure 4.14: Divergence of two experimental systems. (a) The systems are uncoupled at $t = 0$, and the time-series x_1 and x_2 diverge for $t > 0$. (b) Extraction of experimental divergence rate h_1 over a finite window before the difference $|x_1 - x_2|$ saturates.

Fig. 4.14(a) plots the time-series $x_1(t)$ and $x_2(t)$ which are initially highly synchronized before $t = 0$, which marks time when the two oscillators are released. The signals exponentially diverge and the rate h_1 can be extracted from the experimental time-series, as depicted in (b). By repeating this experiment many times, a histogram analogous to Fig. 4.9 can be made.

4.7 Summary

1. Open loop synchronization of a numerical model to experimental observations is a data assimilation and parameter estimation technique.

2. A computer simulation initialized via open loop synchronization can make reliable forecast of high dimensional chaos.

3. The prediction horizon time varies with initial condition.

4. The maximal Lyapunov exponent can be ascertained by driving two systems into nearby phase space trajectories (by synchronization) and then observing their divergence upon terminating the coupling.

5. In principle, a replica experimental system can be used for measuring the distribution of local Lyapunov exponents.

Chapter 5

Anticipated synchronization

When two or more spatially-separated dynamical systems interact over channels that transmit signals at a finite speed, the network may exhibit achronal synchronization patterns. For example, a pair of bidirectionally coupled chaotic oscillators with a coupling delay τ_C may have a strong correlation at a time shift of τ_C and weak or no correlation at zero lag [86, 87, 88]. Detecting if a unique leader and follower relationship exists is a challenge, and there is evidence, in fact, that the role of each node can switch randomly [50]. Extrapolating from this two-node result, it may be expected that a large network of N chaotic oscillators with each coupling link having a nonuniform time delay τ_{ij} will exhibit an even more complicated dance, perhaps forming clusters that jump in and out of lagged synchrony. Thus, observations of long-range isochronal synchrony in neuronal systems [89, 90] is surprising and have been a source of motivation for numerous analytical [91, 92, 93], numerical [49], and experimental [48, 94] studies over the past decade. An understanding of how nature is arranged or how we may arrange nature such that stable zero-lag synchrony is maintained over long distances is useful from a fundamental perspective in regards to information processing in the brain and for applied purposes such as communication networks. A parallel focus over the past decade has been to elucidate the mechanisms responsible for anticipated synchrony – an intrigu-

ing type of achronal synchronization in which a set of nodes anticipates the future states of another. For example, response latency within the retina causes visual data not to reach the visual cortex for processing until 30-100 ms after a stimulus [95]. It has been suggested that an anticipation and prediction process by the cortex compensates for these delays [95, 96]. In this Chapter, we outline the key concepts pertaining to anticipated synchronization and present preliminary experimental and numerical examples from a network of optoelectronic feedback loops.

Anticipated synchronization occurs when the output of a time-delayed oscillator with internal delay τ_{11} is unidirectionally coupled into an identical oscillator with a coupling delay $\tau_{21} < \tau_{11}$. In this case, the output signal of the slave node $x_2(t)$ leads the output of the master node $x_1(t)$ by $\tau_{11} - \tau_{21}$. The signal of node 2 can then be unidirectionally coupled into an identical third node with coupling delay τ_{32}. Node 3 anticipates the output of the master node by $2\tau_{11} - \tau_{21} - \tau_{32}$. In the limit that the coupling delays $\tau_{j+1,j}$ are small compared to the internal delay τ_{11}, node 2 synchronizes to node 1 with a shift of approximately one round-trip delay and node 3 synchronized to node 1 with a shift of approximately two round-trip delays. In theory, this cascade can be repeated ad infinitum with each subsequent slave node anticipating the dynamics of the master by another multiple of τ_{11}. In essence, the chain of replica nodes are driven into synchrony with the master system without any effect on the master's dynamics, and they are predicting the future values of the driver system. Even if the chaos of the driver system is characterized by a prediction horizon time $1/h_1 < \tau_{11}$, the response nodes provide access to $x_1(t)$ at times greater than τ_{11} into the future. In theory, anticipated synchronization is

able to enhance the attainable prediction horizon to an arbitrarily long time. By replacing the identical replica nodes with a chain of numerical models, a computer can continuously predict the future states of the experimental system far in advance. In practice, there is a limit to how far into the future a chaotic oscillator's output can be reliably forecast using this anticipated synchronization scheme. Perturbations, mismatches, and noise propagate and intensify along the path of cascaded nodes, whether the nodes are physical or numerical. Since unidirectional coupling is employed, there is no chance for recovery as there would be for a bidirectional array.

The notion of anticipated synchronization was first advanced by Voss in Refs. [59] and [97]. The first experimental measurements on time-delayed electronic oscillators were also performed by Voss [98]. Experimental investigations have been published using a unidirectionally coupled pair of chaotic semiconductor lasers [99] and numerical models demonstrate anticipated synchronization for coupled neurons [100]. Stability of anticipated synchronization is the subject of Ref. [101]. Studies have considered the applicability of anticipated synchronization to the prediction problem [102] and the parameter estimation problem [103].

5.1 Anticipated synchronization between three optoelectronic feedback loops

As an experimental demonstration of anticipated synchronization of high-dimensional chaotic oscillators, we consider a closed loop optoelectronic feedback

loop as a master system and two cascaded open loop systems as slaves. The parameters of each loop, including the laser powers, half-wave voltages, and amplification factors, are tuned to be nominally identical. The electronic bandwidth is 1–100 MHz and the effective feedback strengths are $\beta \approx 4$. The internal feedback delay of the driver loop is $\tau_{11} = 72$ ns. Fig. 5.1 is a schematic of this setup. The modulation voltage of the master loop $V_1(t)$ is split off to also act as a coupling signal for the second node. The coupling delay τ_{21} is chosen to be smaller than τ_{11}. Note that the coupling signal may also be transmitted via an optical fiber by using an optical 1×2 splitter at node 1. The output voltage of the second node $V_2(t)$ is used as a modulation voltage for the third node, which outputs a voltage signal $V_3(t)$. The signals $V_1(t)$, $V_2(t)$, and $V_3(t)$ are observed on a fast oscilloscope. The communication delays are distributed throughout the network, and are estimated to be $\tau_{21} = 36$ ns and $\tau_{32} = 36$ ns.

In Fig. 5.2, we plot the normalized time-series $x_1(t)$, $x_2(t)$, and $x_3(t)$ measured simultaneously. There are obvious time-shifted correlations in the temporal patterns within the three signals; the dashed lines highlight some analogous features that appear in each time-series. In Fig. 5.3, we plot (a) the autocorrelation of $x_1(t)$, (b) the cross-correlation between $x_1(t)$ and $x_2(t)$, and (c) the cross-correlation between $x_1(t)$ and $x_3(t)$. All of these are normalized such that an autocorrelation equals 1 at zero lag. In (a), we find that the dynamics of isolated feedback loop with this parameter set has time-domain structure dictated by the round-trip time since there are strong peaks at $\pm\tau_{11} = \pm 72$ ns. Plot (b) confirms that x_2 leads x_1 by $\Delta T_2 = \tau_{11} - \tau_{21} = 36$ ns such that $x_2(t) \approx x_1(t + \Delta T_2)$. The correlation coefficient

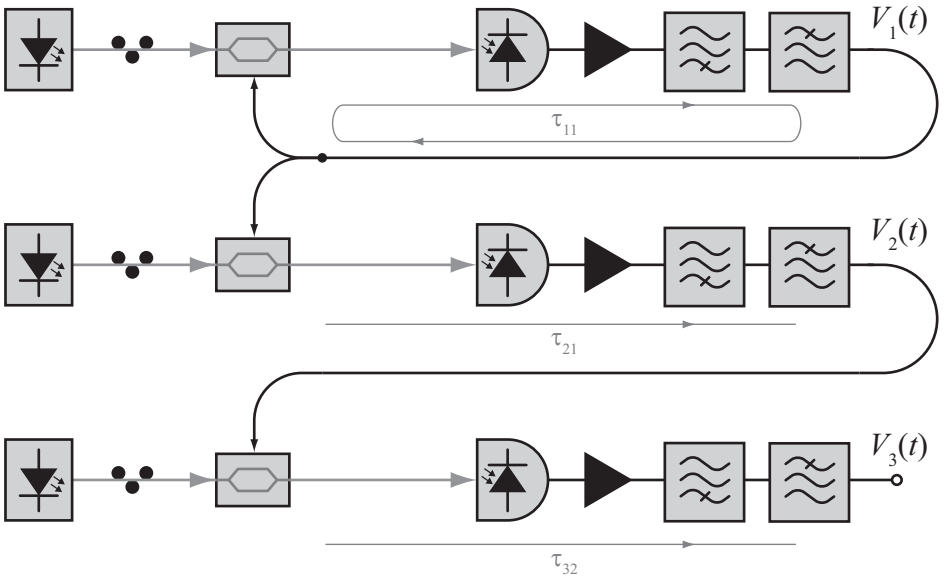

Figure 5.1: Schematic of three-node anticipated synchronization experiment. The top loop is closed and the two bottom systems anticipate the dynamics of the top one. The round-trip time of the top loops is τ_{11}, the delay from loop 1 to loop 2 is τ_{21}, and the delay from loop 2 to loop 3 is τ_{32}.

at this lag is 0.94, implying good lead synchronization. Plot (c) has a peak of 0.76 at $+\Delta T_3 = \tau_{11} - \tau_{21} - \tau_{32} = 72$ ns. The anticipated synchrony between x_3 and x_1 is not as good as between x_2 and x_1. In Fig. 5.4, we superpose the three time-series with x_1 and x_2 shifted forward in time by 36 and 72 ns respectively. Here, the anticipated synchrony is evident. Fig. 5.5(a) is a synchronization plot between x_2 and the time-shifted x_1. The data points fit well to a line but have a slope less than 1. The most likely cause is a mismatch between the bias parameters ϕ_0 of node 1 and 2. The corresponding synchronization plot between x_3 and x_1 in panel (b) has a much broader spread of points. The anticipated synchronization error grows larger for each node in the cascaded unidirectional network.

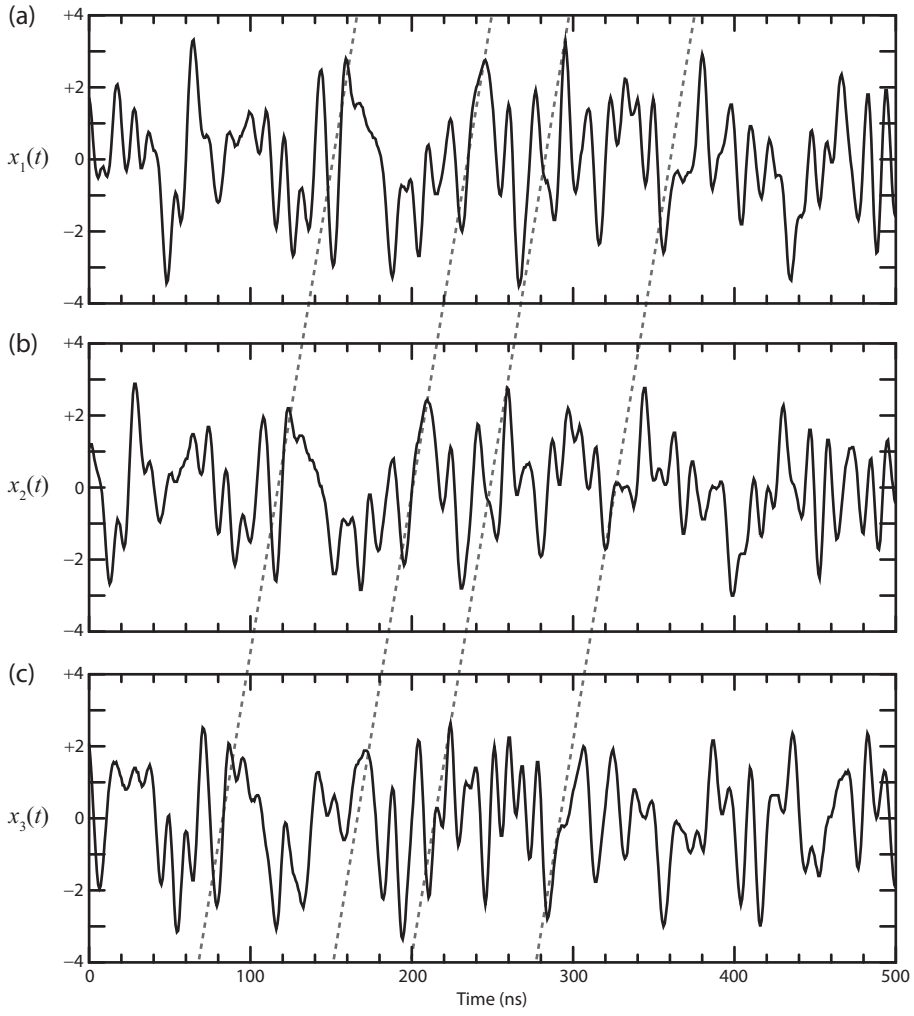

Figure 5.2: Experimental anticipated synchronization time-series. (a) Master dynamics $x_1(t)$. (b,c) Anticipated dynamics $x_{2,3}(t)$.

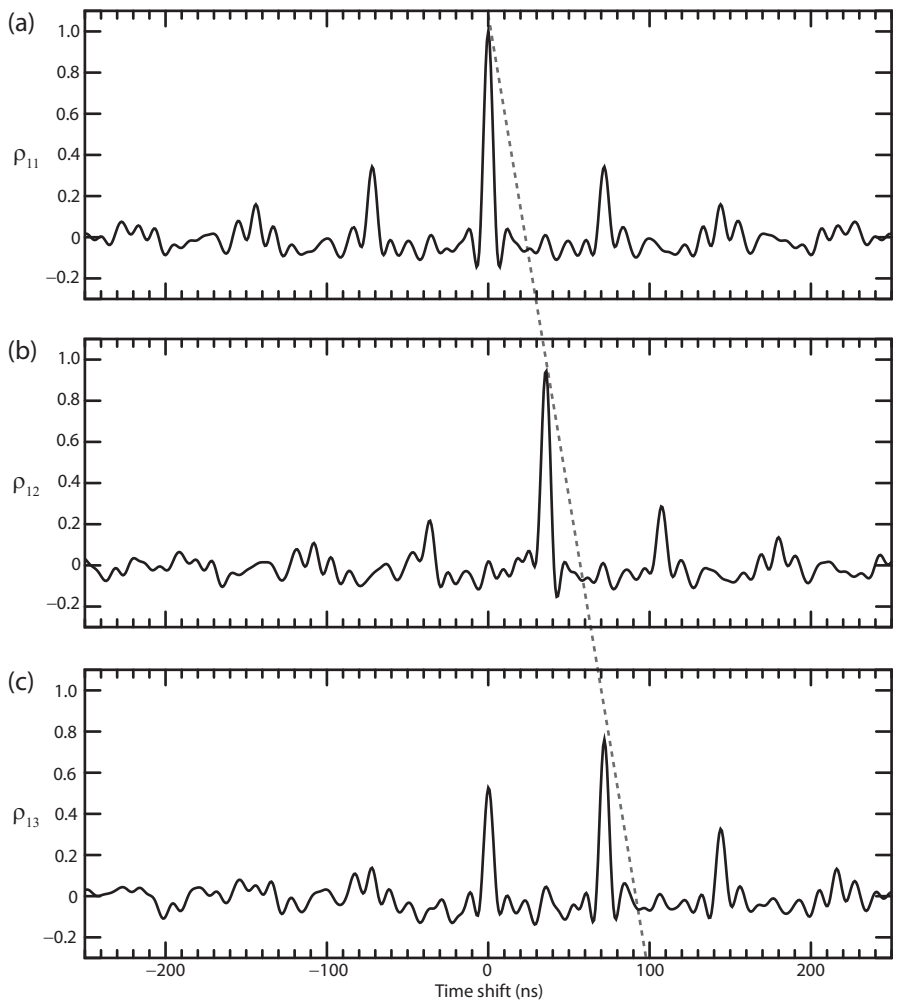

Figure 5.3: (a) Autocorrelation for x_1. (b) Cross-correlation between x_1 and x_2 has a peak at $\Delta T = 36$ ns. (c) Cross-correlation between x_1 and x_3 has a peak at $2\Delta T = 72$ ns.

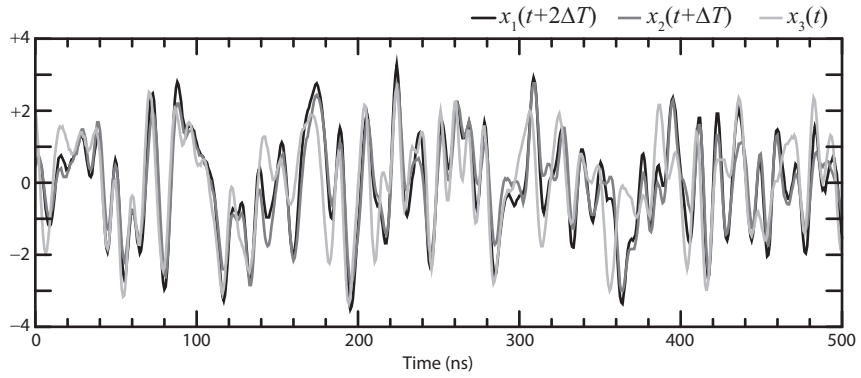

Figure 5.4: Time-shifted experimental time-series.

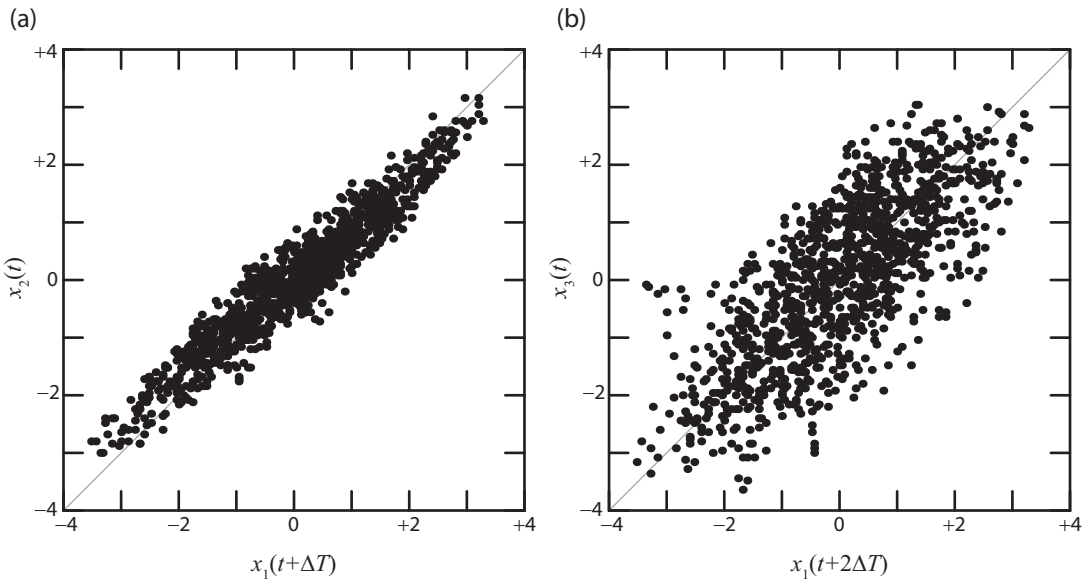

Figure 5.5: Synchronization plots (a) between x_2 and future x_1, (b) between x_3 and future x_1.

5.2 Anticipated synchronization of experimental time-series by cascaded numerical models

The replica nodes used for anticipated synchronization need not be physical. If a numerical model can mimic the input–output relationship of an open loop node with reasonable precision, then it can be synchronized to an acquired experimental signal $x_1(t)$. This procedure is equivalent to the open loop synchronization strategy examined in §4.1 except that the time-delay operation is withheld from the numerical model. Fig. 5.6 is the mathematical block diagram used by Simulink for this computation. The input time-series x_1 is input into an assembly of functions that replicate a single loop within a delay term (nonlinearity and bandpass filtering) to generate a solution x_2. Next x_2 is processed in the same manner to form x_3. Likewise, x_4 is calculated from operations on x_3. This cascade can be repeated as many

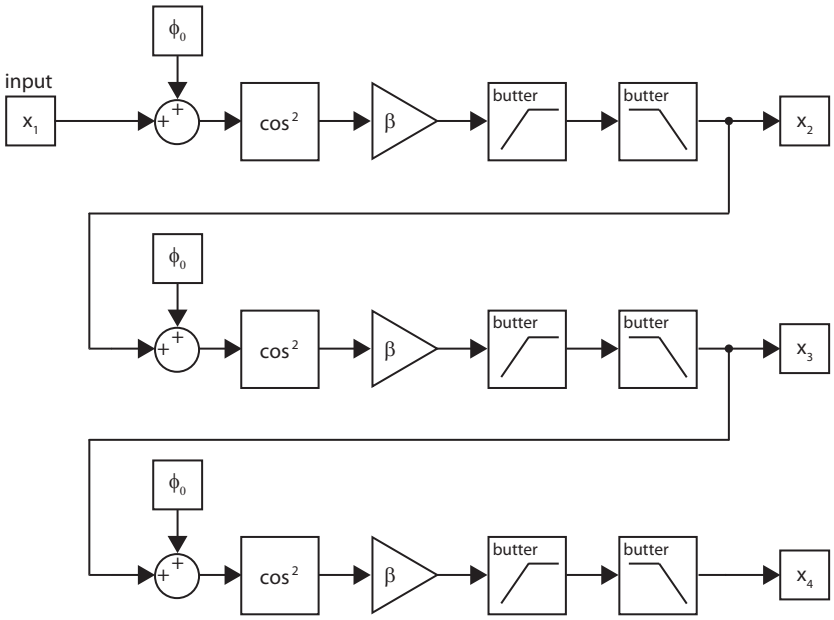

Figure 5.6: Block diagram for a numerical model that anticipates an experimental time-series.

times as desired. In terms of time-domain evolution equations, this set of solutions are given by:

$$\frac{d\mathbf{u}_2(t)}{dt} = \mathbf{A}\mathbf{u}_2(t) - \mathbf{B}\beta\cos^2[x_1(t)+\phi_0], \tag{5.1}$$

$$x_2(t) = \mathbf{C}\mathbf{u}_2(t), \tag{5.2}$$

$$\frac{d\mathbf{u}_3(t)}{dt} = \mathbf{A}\mathbf{u}_3(t) - \mathbf{B}\beta\cos^2[x_2(t)+\phi_0], \tag{5.3}$$

$$x_3(t) = \mathbf{C}\mathbf{u}_3(t), \tag{5.4}$$

$$\frac{d\mathbf{u}_4(t)}{dt} = \mathbf{A}\mathbf{u}_4(t) - \mathbf{B}\beta\cos^2[x_3(t)+\phi_0], \tag{5.5}$$

$$x_4(t) = \mathbf{C}\mathbf{u}_4(t). \tag{5.6}$$

In Fig. 5.7, we plot the time-shifted $x_1(t)$ along with the projected solutions $x_2(t)$, $x_3(t)$, and $x_4(t)$. Each subsequent node predicts one additional round-trip τ_{11} in advance but with reduced precision. This latter point is illustrated with the

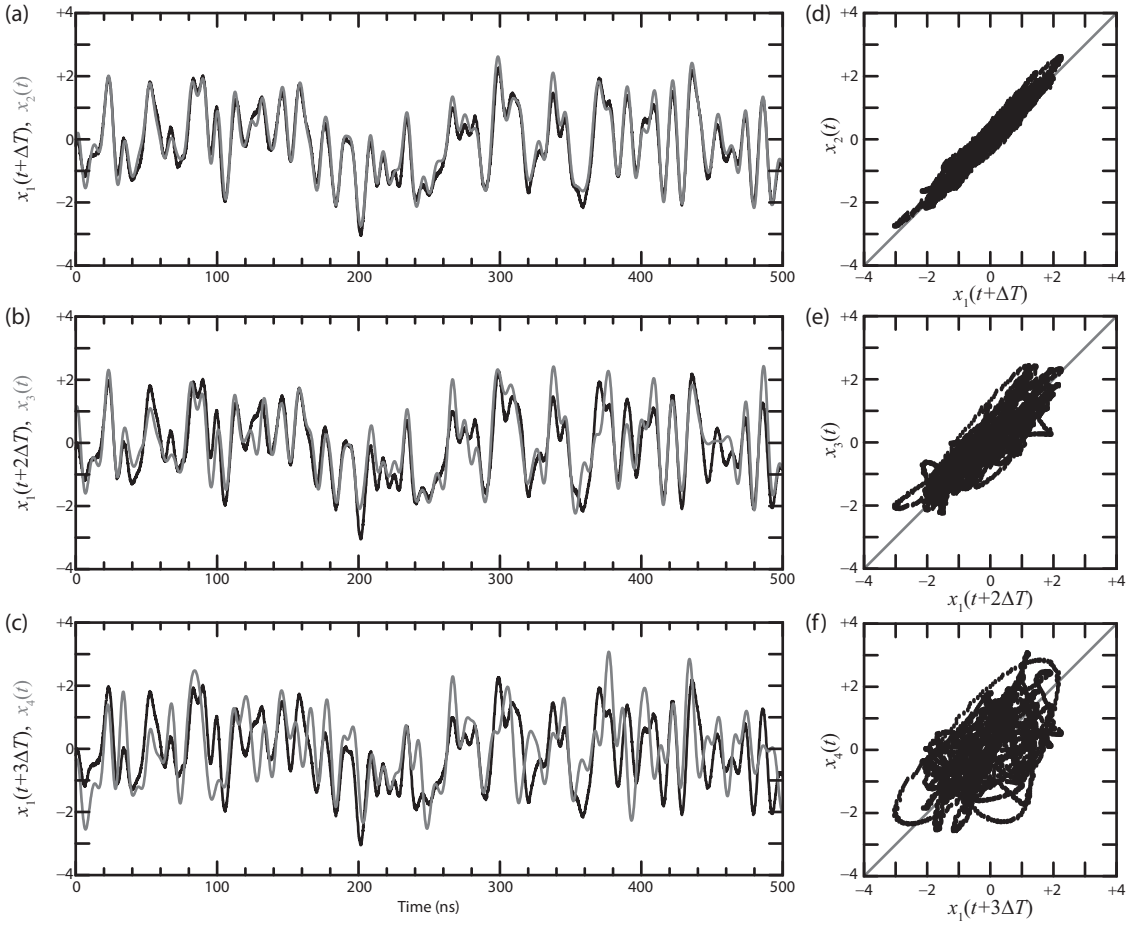

Figure 5.7: Anticipated synchronization of experimental data by a computer model. (a,b,c) Output time-series of first, second, and third cascaded node along with forward-shifted x_1. (d,e,f) Corresponding synchronization plots.

synchronization plots (b), (d), and (f) which become systematically broader.

Anticipated synchronization can be used to extend the prediction technique surveyed in Chapter 4 and Ref. [10]. The numerical model for an isolated optoelectronic feedback oscillator is relatively accurate, and it synchronizes to real experimental data with high precision. The prediction horizon time can be lengthened by using a series of cascaded numerical models rather than a single loop. At a specified time t, the experimental input $x_1(t)$ can be terminated and replaced by a delayed feedback term. The input to the first node $x_1(t)$ can be replaced with $x_2(t - \tau_{11})$. The cascaded series has more information about the history of the experimental system than a single loop, and may be able to make longer predictions with confidence.

5.3 Summary

1. Synchrony of a network with time-delayed couplings may be achronal (lead and lag) or isochronal (zero-lag).

2. Anticipated synchrony can occur for a unidirectional chain of oscillators, and it is practically useful for time-series prediction.

3. A network of optoelectronic time-delay oscillators is a good testbed system for experiments on anticipated synchronization.

4. We have experimentally demonstrated the phenomenon of anticipated synchronization with two cascaded oscillators.

5. If a numerical model can precisely reproduce the chaotic behavior of an oscillator, then it can be used for prediction by anticipated synchronization.

Chapter 6

Stability of adaptive synchronization[1]

An adaptive synchronization technique maintains synchrony on a network of chaotic oscillators even when the coupling strengths A_{ij} are a priori unknown and time-varying in possibly an unpredictable manner. In Ref. [37], an adaptive strategy was proposed in which each node in the network seeks to minimize a local measure of synchronization error via gradient descent. Operationally, a control system at each node manages the strength of the incoming signal r_i by applying a multiplicative weight. This weighting procedure ensures that a globally synchronous state is admitted. The signal r_i is assumed to be a linear superposition of the outputs of all the nodes. In Ref. [37], the adaptive technique was numerically verified to synchronize a network of low dimensional chaotic oscillators. In Ref. [5], the adaptive technique was experimentally demonstrated on a network of two unidirectionally coupled optoelectronic feedback loops with a fluctuating coupling strength $A_{12}(t)$. For a channel modulation of the form $A_{21}(t) = A_0 + \Delta A_0 \sin(2\pi F t)$, the quality of synchronization was systematically tested as a function of the amplitude ΔA_0 and frequency F. In Ref. [42], a bidirectionally coupled three-node network of optoelectronic loops was used to test the range of operation and applicability for sensing and tracking changes to the coupling strengths.

A pertinent question is how the adaptive technique and its associated time-

[1]Portions of this Chapter are modified excerpts from Ref. [42].

scales modify the stability of the synchronous state. Investigations into this topic are presented in Refs. [42] and [52] in which the master stability function formalism [30] was extended to incorporate the adaptive rule. In this Chapter, we outline the key results and apply them to a network of optoelectronic feedback loops. We also quantify geometrical symmetries of the derived master stability function. Recent results claim that the stability contours for a network of time-delay systems, for which optoelectronic oscillators are an example, have a specific, well-defined shape in the complex plane [55].

In §6.1, we review the adaptive synchronization strategy and presents its equations of motion and control as a discrete-time map. We apply the strategy to a network of optoelectronic feedback loops with DSP-based filtering, time delay, and control (see §2.11).

In §6.2, we derive the master stability function for the case of adaptive control and we compute the stability contours for a network of optoelectronic nodes.

In §6.3, we introduce an experimental three-node network with symmetric coupling strengths ($A_{12} = A_{21}, A_{23} = A_{32}, A_{31} = A_{13}$) that can be adjusted arbitrarily for $A_{ij} \geq 0$. We measure the range of stability for a given network configuration by measuring the synchronization error as a single coupling parameter is tuned, and we interpret the results based on the master stability function.

In §6.4, we consider numerical simulations on an adaptive network of $N = 25$ nodes and study the synchronous behavior for different control time-scales.

In §6.5, we review the main findings of Ref. [55] and quantify the rotational symmetry of the specific master stability function with time-delayed couplings de-

rived here.

6.1 Review of adaptive synchronization strategy

Here we present the equations for an adaptive network in discrete time. Let the state of node $i = 1, \ldots, N$ at time n be $\mathbf{x}_i[n]$. The coupled dynamics are the N map equations:

$$\mathbf{x}_i[n] = \mathbf{F}(\mathbf{x}_i[n-1]) + \varepsilon \mathbf{v} \sum_{j=1}^{N} A_{ij} H(\mathbf{x}_j[n-1]) \tag{6.1}$$

where we assume a scalar output function $H(\mathbf{x})$ which is added into the dynamics with the vector $\mathbf{v}$. We assume that node i only has access to the net coupling signal $r_i = \sum_{j=1}^{N} A_{ij} H(\mathbf{x}_j)$ and its local counterpart $H(\mathbf{x}_i)$ but not to each of the summands $A_{ij} H(\mathbf{x}_j)$ nor the individual matrix elements A_{ij}. Only if the row sums of the adjacency matrix $\mathbf{A}$ are uniform, i.e. $k_i \equiv \sum_{j=1}^{N} A_{ij} = k_0$ for all i, is a globally synchronous solution $\mathbf{x}_i[n] = \mathbf{s}[n]$ possible. If so, then the state

$$\mathbf{s}[n] = \mathbf{F}(\mathbf{s}[n-1]) + \varepsilon \mathbf{v} k_0 H(\mathbf{s}[n-1]) \tag{6.2}$$

defines motion on the $(N-1)$-dimensional synchronous manifold $\mathbf{x}_1 = \cdots = \mathbf{x}_N$. For network-based synchronization studies, it is often taken for granted that the row sum condition is satisfied. However, for an arbitrarily chosen network configuration, this is seldom case. Moreover, even if a network is initially tuned to have $k_i = k_0$ for all i, the uniform row sums are not preserved when there are changes in the A_{ij}'s such as an interrupted coupling path ($A_{ij} \to 0$ for a specific i and j) or temporal drift in coupling strengths ($A_{ij} \to A_{ij}[n]$).

One method to enforce the possibility of synchrony is to have each node weight the incoming net coupling term r_i by k_i. Then the effective coupling matrix is $A'_{ij} = A_{ij}/k_i$ and the condition $\sum_{j=1}^{N} A'_{ij} = 1$ is met by definition. (We assume $k_i > 0$ so that there are no problems with division by zero.) The adaptive technique described here seeks to construct real-time estimates of the k_i's, even as they vary in time: $k_i = k_i[n]$. Let $\bar{k}_i$ be the estimate of k_i. We reexpress Eqs. (6.1) as

$$\mathbf{x}_i[n] = \mathbf{F}(\mathbf{x}_i[n-1]) + \varepsilon \mathbf{v} \frac{1}{\bar{k}_i[n-1]} \sum_{j=1}^{N} A_{ij} H(\mathbf{x}_j[n-1]) \tag{6.3}$$

The update equations for $\bar{k}_i[n]$ are derived and motivated in Refs. [5], [37], [42], and [52], and they are:

$$\frac{1}{\bar{k}_i[n]} = \frac{p_i[n]}{q_i[n]}, \tag{6.4}$$

$$p_i[n] = z_0 p_i[n-1] + (1-z_0)(r_i[n] H(\mathbf{x}_i[n])), \tag{6.5}$$

$$q_i[n] = z_0 q_i[n-1] + (1-z_0)(r_i[n])^2, \tag{6.6}$$

where z_0 is a parameter that determines the time-scales for which $\bar{k}_i$ can successfully track variations in the coupling strengths. Explicitly, z_0 defines the smoothing factor for an exponentially weighted moving average of $(r_i[n] H(\mathbf{x}_i[n]))$ and $(r_i[n])^2$ for p_i and q_i respectively. The averaging window has a characteristic length of $(1-z_0)^{-1}$ samples or $T = T_{\mathrm{s}}(1-z_0)^{-1}$ where T_{s} is the interval between successive samples n and $n+1$. The range of z_0 is $(0,1)$ and a smaller value allowing for faster tracking (corresponding to a shorter averaging time T). However, as we describe in §6.2, the ability to track a faster variation comes at the cost of a reduced synchronization range.

In some situations, such an adaptive network can be designed to act as a sensor network. As such, the set of estimated row sums $\{\bar{k}_i[n]\}$ can be used to uniquely resolve each of the individual coupling terms $A_{ij}[n]$ in real-time. For a symmetrically coupled three-node network, it is possible to compute the three coupling strengths $A_{ij} = A_{ji}$ by algebraically solving the equations $\bar{k}_i = \sum_{j=1}^{3} \bar{A}_{ij}$, $i = 1, 2, 3$. Thus, if a centralized hub has access to $\bar{k}_1[n]$, $\bar{k}_2[n]$ and $\bar{k}_3[n]$, then the complete time-varying network topology $\mathbf{A}[n]$ can be ascertained.

We now outline how the adaptive synchronization technique is applied to a network of optoelectronic feedback loop oscillators. The uncontrolled equations of motion are a network-generalization of Eq. (2.23):

$$x_i[n] = -a_1 x_i[n-1] - a_2 x_i[n-2] - b_0 \beta \sum_{j=1}^{N} A_{ij}(\cos(x_j[n-k]+\phi_0) - \cos(x_j[n-k-2]+\phi_0)) \tag{6.7}$$

where $x_i[n]$ is the digital bandpass filter output of node i and $-\beta \cos^2(x_j[n-k]+\phi_0)$ is the output by node j delayed by k time units. Eq. (6.7) can be cast in the form of Eq. (6.1) by defining the state vectors $\mathbf{x}_i[n]$ as a set of delay coordinates incorporating the last $(k+2)$ iterates. The adaptive strategy is operationally applied by programming the DSP board installed at each node to solve for $p_i[n]$ and $q_i[n]$ and to scale the feedback strength as: $\beta \to \beta/\bar{k}_i[n] = \beta(p_i[n]/q_i[n])$. Here β plays the role of ε in Eq. (6.1). The specific details regarding the order of operations as implemented by the DSP and how to define $\mathbf{F}(\mathbf{x})$, $H(\mathbf{x})$, and $\mathbf{v}$ in terms of Eqs. (6.1) are presented in Ref. [42].

The adaptive strategy was implemented on a three-node network, as depicted

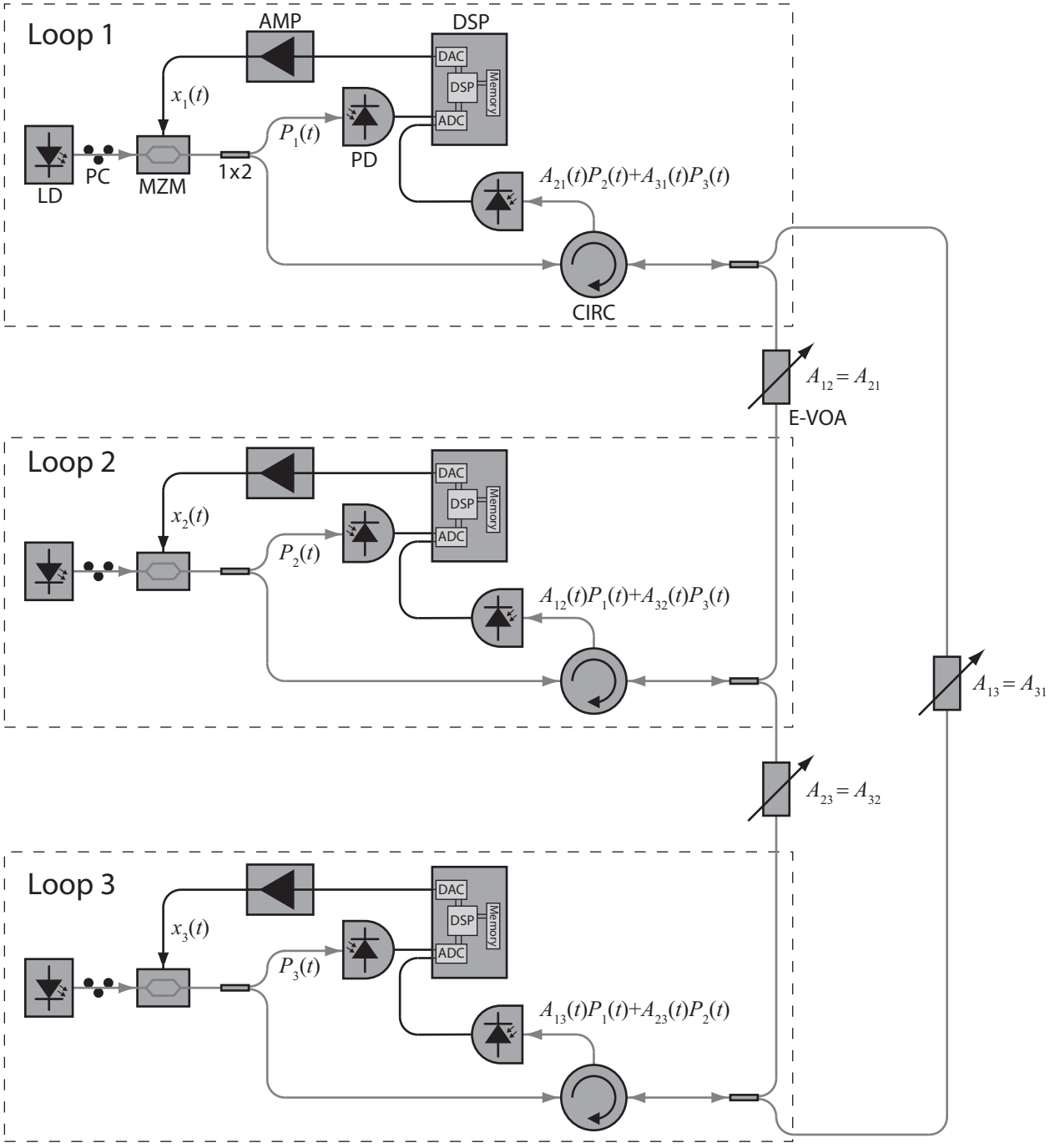

Figure 6.1: Experimental schematic of three-node network of optoelectronic feedback loops.

in Fig. 6.1. In this setup, the internodal communication is sent over bidirectional fiber optic channels. An optical circulator is used to transmit the signal from a node to the two other nodes and also to receive a superposed signal from the other two nodes. A bank of electronically variable optical attenuators allows for independent control of the symmetric coupling strengths $A_{ij} = A_{ji}$. In Refs. [42] and [69], the network's response to sudden changes in a single coupling channel and simultaneous changes in multiple channels are compared for a static network with fixed β's and an adaptive network which adjust the weight factors $1/\bar{k}_i$ in real-time. The adaptive network was able to adjust to and recover from coupling strength modulations and maintain synchrony, while for uncontrolled nodes synchrony was destroyed.

Here our focus is the relationship between network structure in terms of the eigenvalues of the matrix $\mathbf{A}$, the adaptive strategy response time in terms of z_0, and the range of synchronization in terms of specific coupling elements A_{ij}.

6.2 Stability analysis of adaptive networks

In this Section, we derive the master stability function for N coupled systems described by Eq. (6.4) under the control of the adaptive rule given by Eqs. (6.4)–(6.6). We follow the approach of Ref. [52], but described here in discrete time.

Eqs. (6.4)–(6.6) admit the synchronous solution $\mathbf{x}_i[n] = \mathbf{s}[n]$, for all i and n,

given by

$$\mathbf{s}[n+1] = \mathbf{F}(\mathbf{s}[n]) + \mathbf{v}\varepsilon H(\mathbf{s}[n]), \tag{6.8}$$

$$p_i[n] = k_i \langle H(\mathbf{s}[n])^2 \rangle_{z_0}, \tag{6.9}$$

$$q_i[n] = k_i^2 \langle H(\mathbf{s}[n])^2 \rangle_{z_0}, \tag{6.10}$$

where $\langle G \rangle_{z_0} = (1-z_0)\sum_{m=0}^{\infty}(z_0)^m G[n-m]$ is an exponentially weighted moving average of G. In the synchronous state, $q_i/p_i = \overline{k}_i = k_i$. By linearizing (6.4)–(6.6) about the synchronous solution (6.8)–(6.10), we obtain,

$$\begin{aligned}
\delta\mathbf{x}_i[n+1] &= \mathbf{DF}(\mathbf{s}[n])\delta\mathbf{x}_i(n) \\
&\quad + \mathbf{v}\varepsilon\Big[\frac{H(\mathbf{s}[n])}{k_i^2\langle (H(\mathbf{s}[n])^2\rangle_{z_0}}\xi_i(n) + \frac{\mathbf{D}H(\mathbf{s}[n])}{k_i}\sum_{j=1}^{N} A_{ij}\delta\mathbf{x}_j[n]\Big], \quad (6.11) \\
\xi_i[n+1] &= z_0\xi_i[n] \\
&\quad + (1-z_0)k_i\Big[k_i\delta\mathbf{x}_i[n] - \sum_{j=1}^{N} A_{ij}\delta\mathbf{x}_j[n]\Big]H(\mathbf{s}[n])\mathbf{D}H(\mathbf{s}[n]), \quad (6.12)
\end{aligned}$$

$i = 1, \ldots, N$, where we have introduced the variable $\xi_i \equiv k_i\delta p_i - \delta q_i$ and $\mathbf{DF} \equiv \partial\mathbf{F}/\partial\mathbf{x}$, $\mathbf{D}H \equiv \partial H/\partial\mathbf{x}$. Eqs. (6.11)–(6.12) constitute a system of $(m+1)N$ coupled equations where $\mathbf{x}_i$ is a state vector of length m. In order to simplify the analysis, we seek to decouple this system into N independent systems, each of dimension $(m+1)$. For this purpose we seek a solution where $\delta\mathbf{x}_i[n]$ is in the form $\delta\mathbf{x}_i[n] = c_i\delta\overline{\mathbf{x}}[n]$, where c_i is a time independent scalar that depends on i and $\delta\overline{\mathbf{x}}[n]$ depends on time but

not on i. Substituting this ansatz into Eqs. (6.11)–(6.12), we obtain,

$$\begin{aligned}
\delta\overline{\mathbf{x}}[n+1] &= \mathbf{DF}(\mathbf{s}[n])\delta\overline{\mathbf{x}}[n] \\
&\quad +\mathbf{v}\frac{\varepsilon}{c_i}\Big[\frac{H(\mathbf{s}[n])}{k_i^2\langle(H(\mathbf{s}[n])^2\rangle_{z_0}}\xi_i(n)+\frac{\mathbf{D}H(\mathbf{s}[n])}{k_i}\delta\overline{\mathbf{x}}[n]\sum_{j=1}^{N}A_{ij}c_j\Big], \quad (6.13)\\
\xi_i[n+1] &= z_0\xi_i[n] \\
&\quad +(1-z_0)k_i\Big[k_ic_i-\sum_{j=1}^{N}A_{ij}c_j\Big]H(\mathbf{s}[n])\mathbf{D}H(\mathbf{s}[n])\delta\overline{\mathbf{x}}[n]. \quad (6.14)
\end{aligned}$$

To make Eqs. (6.13)–(6.14) independent of i, we consider $\overline{\xi}(n)=\xi_i(n)/[(1-\lambda)k_i^2c_i]$ and

$$\sum_{j=1}^{N}A_{ij}c_j=\lambda k_ic_i, \quad (6.15)$$

where λ is a quantity independent of i. Namely, the possible values of λ are the eigenvalues defined by the equatuon $\mathbf{A}'\mathbf{c}=\lambda\mathbf{c}$, corresponding to linearly independent eigenvectors $\mathbf{c}=\begin{bmatrix}c_1 & c_2 & \cdots & c_N\end{bmatrix}$, where

$$\mathbf{A}'=\{A'_{ij}\}=\{k_i^{-1}A_{ij}\}. \quad (6.16)$$

From Eq. (6.16), we can see that λ is an eigenvalue of a new matrix $\mathbf{A}'$, i.e., a row-rescaled version of the original matrix $\mathbf{A}$. This gives

$$\begin{aligned}
\delta\overline{\mathbf{x}}[n+1] &= \mathbf{DF}(\mathbf{s}[n])\delta\overline{\mathbf{x}}[n] \\
&\quad +\mathbf{v}\varepsilon\Big[(1-\lambda)\frac{H(\mathbf{s}[n])}{\langle(H(\mathbf{s}[n])^2\rangle_{z_0}}\overline{\xi}(n)+\lambda\mathbf{D}H(\mathbf{s}[n])\delta\overline{\mathbf{x}}[n]\Big], \quad (6.17)\\
\overline{\xi}[n+1] &= z_0\overline{\xi}[n]+(1-z_0)H(\mathbf{s}[n])\mathbf{D}H(\mathbf{s}[n])\delta\overline{\mathbf{x}}[n], \quad (6.18)
\end{aligned}$$

which is independent of i but depends on the eigenvalues λ. Considering the typical case where there are N distinct eigenvalues of the $N\times N$ matrix $\mathbf{A}'$, we see that Eqs. (6.17) constitute N decoupled linear difference equations for the synchronization

perturbation variables $\delta\overline{\mathbf{x}}$ and $\overline{\xi}$. All the rows of $\mathbf{A}'$ sum to 1, therefore $\mathbf{A}'$ has at least one eigenvalues $\lambda = 1$, corresponding to the eigenvector $c_1 = c_2 = \ldots = c_N = 1$. For $\lambda = 1$, Eqs. (6.17) becomes

$$\delta\overline{\mathbf{x}}[n+1] = \Big[\mathbf{DF}(\mathbf{s}[n]) + \mathbf{v}\varepsilon\mathbf{D}H(\mathbf{s}[n])\Big]\delta\overline{\mathbf{x}}[n]. \tag{6.19}$$

This equation reflects the chaos of the reference synchronized state (6.8) and (because all the c_i are equal) is associated with perturbations that are tangent to the synchronization manifold and are therefore irrelevant in determining synchronization stability. Stability of the synchronized state thus requires Eq. (6.17)–(6.18) yield exponential decay of $\delta\overline{\mathbf{x}}$ and $\overline{\xi}$ for all the eigenvalues λ, excluding the 'irrelevant' $\lambda = 1$ eigenvalue.

The problem of stability of the synchronized solutions (6.8)–(6.10) for an arbitrary network of coupled systems evolving according to Eq. (6.3)–(6.6) can be evaluated using a master stability function $M(\lambda, z_0)$ that associates the pair (λ, z_0) with the maximum Lyapunov exponent of Eqs. (6.17)–(6.18) (i.e., the average growth rate of the vector $(\delta\overline{\mathbf{x}}, \overline{\xi})$ for a specific λ and z_0).

We now calculate the extended master stability function for a network of optoelectronic feedback loops described by the Eqs. (6.7) under adaptive control. It is found that it is essential to include the dynamics of the adaptive strategy; e.g. the smoothing parameter z_0 has a substantial effect in determining stability.

Fig. 6.2 is the master stability surface $M(\lambda, z_0) = M(\lambda^{(\mathrm{R})} + i\lambda^{(\mathrm{I})})$ for $z_0 = 0.99$ ($T = 4.17$ ms when $T_s = 1/24$ ms). There is a global minimum at $\lambda^{(\mathrm{R})}{=}\lambda^{(\mathrm{I})} = 0$ with $M(0) \approx -0.5$ ms^{-1}. An intersection with the $M = 0$ plane differentiates the

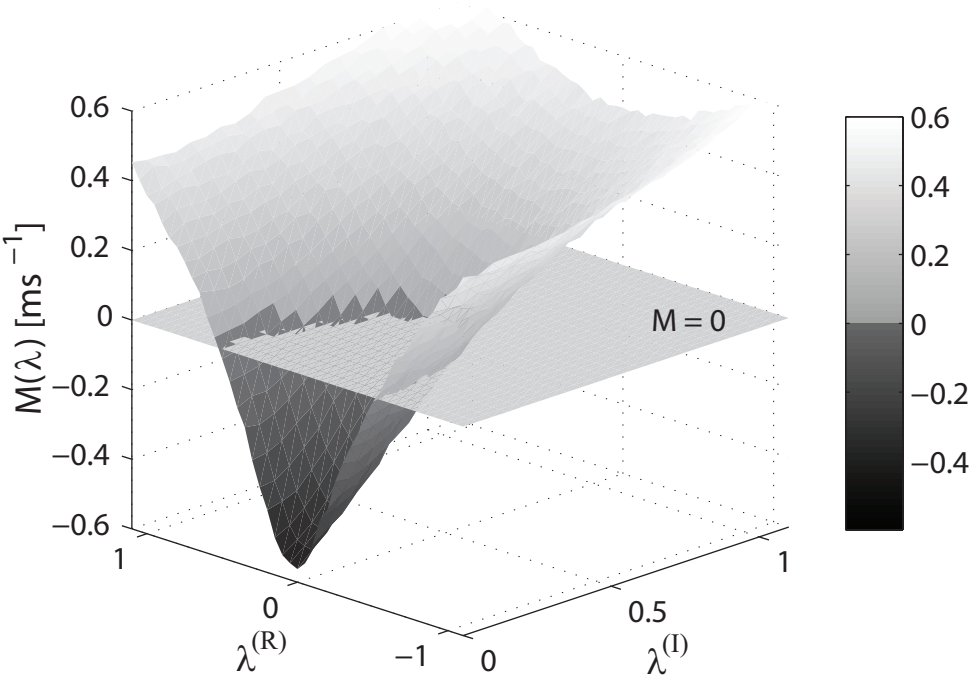

Figure 6.2: Master stability surface $M(\lambda, z_0)$ in as a 3D plot over the complex plane $(\lambda^{(\mathrm{R})}, \lambda^{(\mathrm{I})})$ for $z_0 = 0.99$. The intersection with the $M = 0$ plane defines the region of stability.

region of stability ($M < 0$) from the unstable region ($M \geq 0$). Note that the master stability function M has reflection symmetry about the real axis: $M(\lambda^{(\mathrm{R})} + i\lambda^{(\mathrm{I})}) = M(\lambda^{(\mathrm{R})} - i\lambda^{(\mathrm{I})})$, and thus we need only plot M in the half plane $\lambda^{(\mathrm{I})} > 0$ to get the full picture.

In Fig. 6.3(a), the same data is plotted as a color image. Red (blue) corresponds to regions with $M > 0$ ($M < 0$), and yellow and cyan correspond to $M \approx 0$. It is evident that the stability contour ($M = 0$) is approximately circular with a radius $\lambda_+ \approx 0.5$. In (b), we plot a cut of M along the real axis $M(\lambda^{(\mathrm{R})})$ for both $z_0 = 0.99$ and $z_0 = 0.95$ ($T = 0.83$ ms^{-1}). For a symmetric adjacency matrix $\mathbf{A}$, the eigenvalues λ_j will all be real, so only $M(\lambda^{(\mathrm{R})}, z_0)$ is required to determine stability.

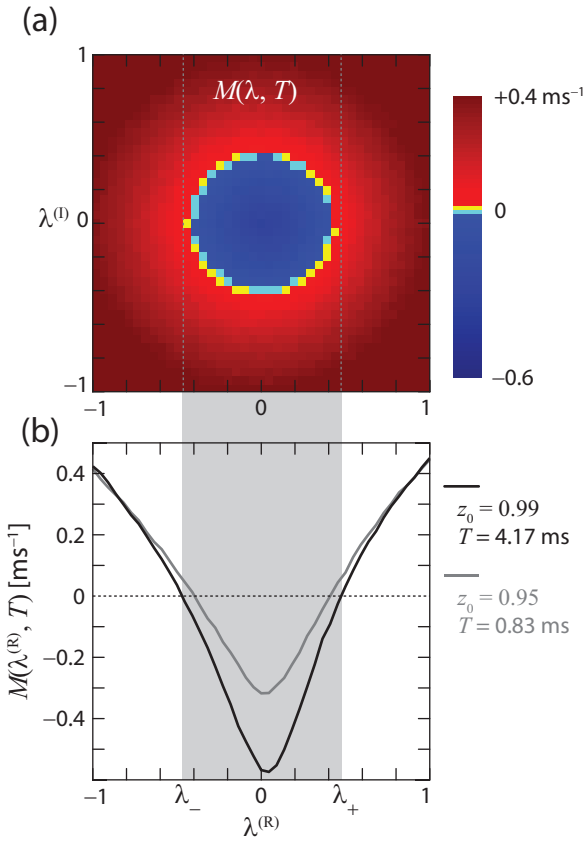

Figure 6.3: (a) Master stability function $M(\lambda^{(\mathrm{R})}+i\lambda^{(\mathrm{I})})$ as a color plot for $z_0 = 0.99$. The circle centered at $\lambda = 0$ defines the stable region with radius $\lambda_+ \approx 0.5$. (b) M along a cut of the real axis for $z_0 = 0.99$ and $z_0 = 0.95$. The stable region (λ_-, λ_+) is defined by $M < 0$.

The region of stability defined by $M(\lambda^{(\mathrm{R})}, z_0) > 0$ is the range (λ_-, λ_+), and this range is slightly larger for $z_0 = 0.99$.

6.3 Range of stability for adaptive three-node network

To experimentally investigate the range of stability, we consider the adaptively controlled three-node network as illustrated in Fig. 6.1. We fix $A_{31} = A_{13} = 0$ and $A_{23} = A_{32} = 1.5$, and we vary the third coupling parameter $A_{12} = A_{21}$ between 0

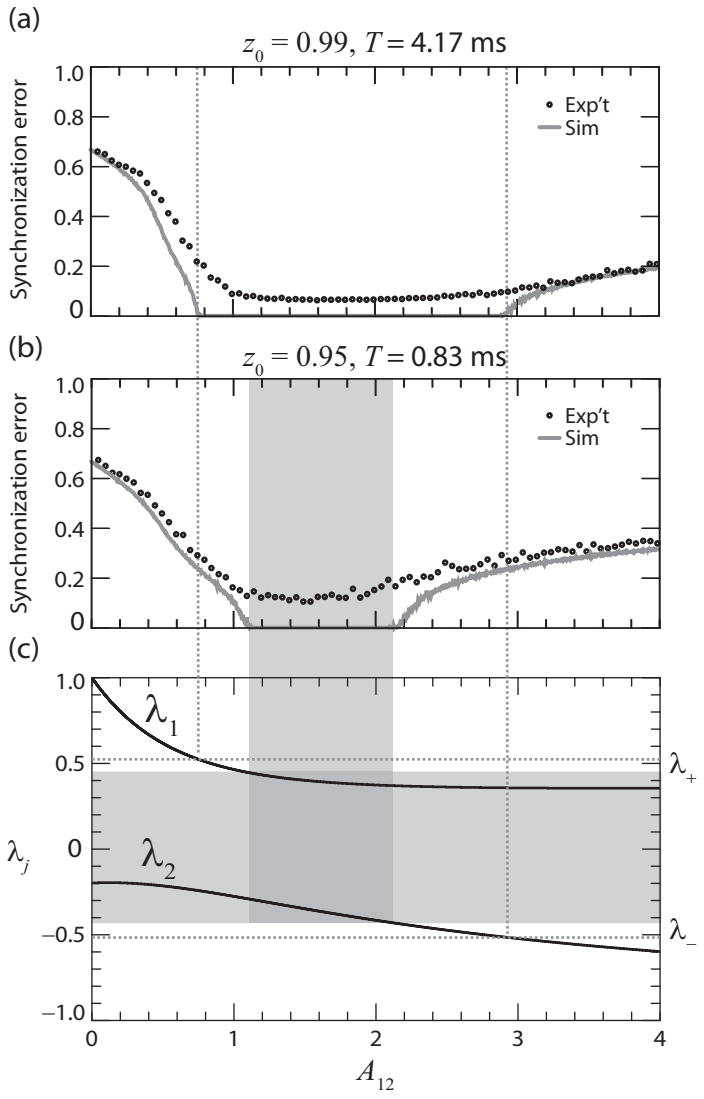

Figure 6.4: Synchronization error as A_{12} is scanned and $A_{13} = 0$, $A_{23} = 1.5$. (a) Synchronization error for $z_0 = 0.99$. (b) Synchronization error for $z_0 = 0.95$. (c) Relevant eigenvalues λ_1 and λ_2 for adjacency matrix $\mathbf{A}$. Only when both eigenvalues fall within the stable range (λ_-, λ_+) does the network synchronize.

and 4. At each point, we measure the average pairwise synchronization error

$$\theta = \frac{1}{N(N-1)} \sum_{i,j,i\neq j} \sqrt{\frac{\langle (x_i - x_j)^2 \rangle}{\langle x_i^2 \rangle + \langle x_j^2 \rangle}}, \tag{6.20}$$

which is 0 for an identically synchronized network and 1 for a network of uncorrelated nodes. In Fig. 6.4(a), the points are the experimentally obtained synchronization errors for $z_0 = 0.99$ and the corresponding solid curve is from numerical simulations. As indicated particularly by the simulations, there are upper and lower bounds for A_{12} for which stability is achieved. In (b), the same measurements and simulations were repeated with the smoothing parameter z_0 set to 0.95. The range of stability is dramatically reduced.

The range of A_{12} in which we observe synchronization for these two values of z_0 can be explained by using the master stability function $M(\lambda^{(\mathrm{R})}, z_0)$. The stability is related to the $(N-1)$ 'relevant' eigenvalues of the rescaled adjacency matrix $A'_{ij} = A_{ij}/k_i$. One eigenvalue of this matrix is one, since $\sum_j A'_{ij} \equiv 1$, and we regard this eigenvalue as irrelevant since it does not figure in the stability analysis. If the two relevant eigenvalues λ_1 and λ_2 fall within the range $(\lambda_-, \lambda+)$ predicted by analysis, then the synchronous solution is linearly stable. In Fig. 6.4(c), we plot λ_1 and λ_2 of $\mathbf{A}'$ as a function of A_{12}. The range of stability predicted by (λ_-, λ_+) (horizontal lines of $z_0 = 0.99$ and grayed region for $z_0 = 0.95$) matches the range of stability observed for A_{12} (vertical lines and grayed region).

The model described in §6.1 and §6.2 assumed a network of identical nodes. In any practical realization, parameter mismatches are unavoidable and will affect the synchronization behavior of the network. An important and nontrivial question is

how well the adaptive strategy works when there are small deviations from identicality of the nodes. Here, we find good agreement between our theoretical calculation which assumes identical nodes and experiments where there is some parameter tolerance. We conclude that the theory, as presented, is applicable for making realistic predictions about which actual networks will synchronize. Moreover, our stability theory, based on the master stability function formalism, can be extended to the case of mismatches in a network of nearly identical systems [104, 105, 106].

6.4 Numerical experiments of a 25-node network

As a further example, we numerically consider a network of optoelectronic systems in which we have a relatively large number of nodes ($N = 25$) and in which the couplings are directional; i.e. A_{ij} may differ from A_{ji}. For cases with $\mathbf{A}$ not symmetric the eigenvalues of $\mathbf{A}'$ may be complex. The two contours in Fig. 6.5 (a) and (c) indicate the region of the complex plane within which the eigenvalues of $\mathbf{A}'$ must fall in order to maintain synchrony, i.e., the region for which the master stability function, $M(\lambda, z_0)$ is negative. The contours were obtained with $z_0 = 0.99$ and $z_0 = 0.95$. When constructing the adjacency matrix, we randomly choose each of the A_{ij} to be either $1/7$ or 0, with probability 0.25 and 0.75, respectively; the diagonal elements A_{ii} are $1/7$. This choice of adjacency matrix yields a distribution of row sums for which the adaptive algorithm must compensate. The eigenvalues of $\mathbf{A}'$ are plotted in the complex planes in Fig. 6.5 (a) and (c). The $(N-1)$ relevant eigenvalues fall within the region for stable synchrony when $z_0 = 0.99$ (a)

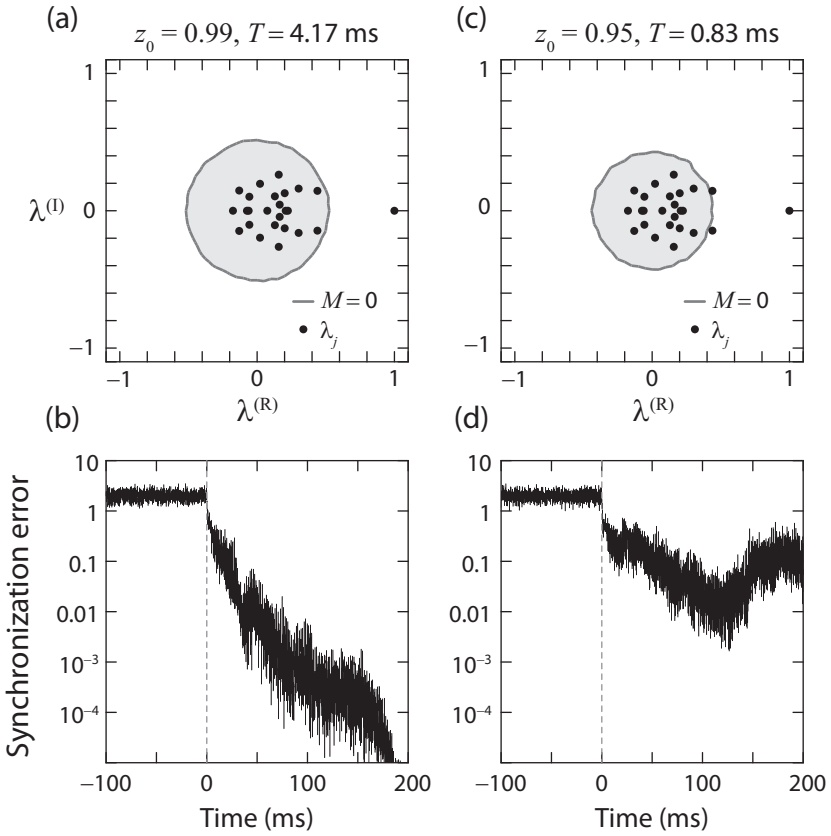

Figure 6.5: Stability of $N = 25$ node network. (a) Stability region in the complex plane for $z_0 = 0.99$ and eigenvalues for a 25-node network. All 24 relevant eigenvalues fall within the stability region. (b) At $t = 0$, the adaptive algorithm is enabled and the network exponentially converges into synchrony. (c) Stability region for $z_0 = 0.95$. The same eigenvalues for the same network is in (a) are plotted. In this case, there are two relevant eigenvalues outside the stability region. (d) When the adaptive routine is enabled for $z_0 = 0.95$, the synchronization error does not tend to zero.

but not when $z_0 = 0.95$ (c). In Fig. 6.5(b), we initially run the full network of N nodes without enabling the adaptive strategy. For $t < 0$, the synchronization error is large. The control is enabled at $t = 0$. The adaptive algorithm pulls the network into synchrony from initially uncorrelated states with an exponential convergence rate that is related to the eigenvalue of $\mathbf{A}'$ with the largest associated relevant transverse Lyapunov exponent. The same numerical experiment was performed with $z_0 = 0.95$

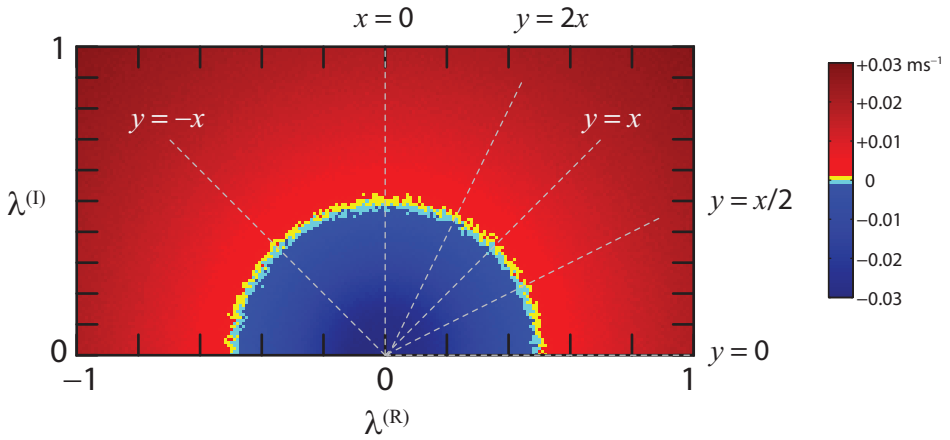

Figure 6.6: Master stability function $M(\lambda)$. The dashed lines are the six cuts plotted in Fig. 6.7.

shown in Fig. 6.5(d). In this case, failure to achieve synchronization was observed, as predicted by the master stability function.

6.5 Symmetries of master stability function

Flunkert et al. analyzed generic properties of the master stability function $M(\lambda)$ when a fixed communication delay τ is imposed uniformly for all the coupling channels, i.e. $H(\mathbf{x}_j) = H(\mathbf{x}_j(t-\tau))$. In the limit of large delay (τ greater than the characteristic time scale of the chaotic orbit), $M(\lambda)$ is claimed to have a simple universal structure within the complex plane. In particular, $M(\lambda)$ is rotationally symmetric about the origin $\lambda = 0$. It is a monotonically increasing function of the distance from the origin r and changes sign from negative to positive at a critical radius r_0. In order to have stable synchrony, all the eigenvalues λ_j of the adjacency matrix $\mathbf{A}$ must have magnitude with $|\lambda_j| < r_0/\varepsilon$ where ε is an overall coupling strength (as in Eq. (1.2)). There may also exist a radius r_b for which un-

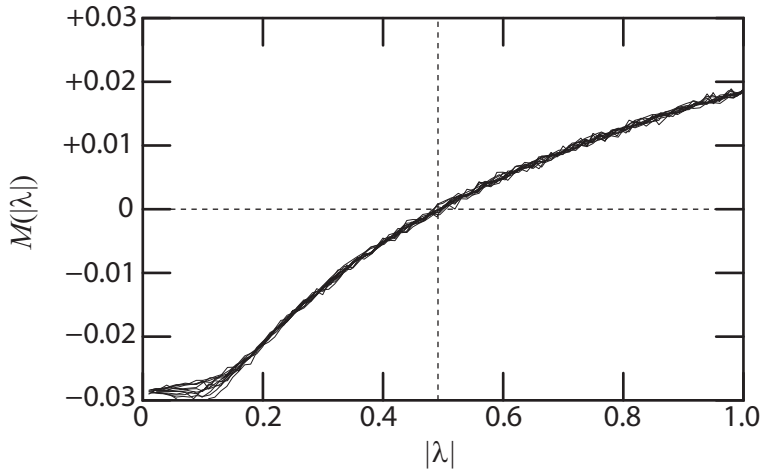

Figure 6.7: $M(\lambda)$ along different lines starting from the origin $\lambda = 0$. All the curves overlap and go through zero at a critical value $r_0 = \lambda_+$.

stable periodic orbits embedded within the chaotic attractor cause the synchronized solution to become linearly unstable and thus cause a bubbling transition [107]. In the Flunkert paper, the theory is numerically verified for a network of chaotic semiconductor lasers with delayed feedback and delayed coupling.

Here, we quantify the rotational symmetry of the master stability function derived for time-delayed optoelectronic chaotic oscillators. The coupling and feedback delay for this DSP-based system is $kT_\mathrm{s} = 36T_\mathrm{s} = 1.5$ ms where $f_\mathrm{s} = 1/T_\mathrm{s} = 24$ kHz, and the dynamical variations of the chaos are at time scale limited by the lowpass filter time constant $\tau_2 = (2\pi f_2)^{-1} = 64$ μs where $f_2 = 2.5$ kHz. Thus the delay τ is about 25 times larger than the characteristic time-scale, and the Flunkert hypothesis applies to the stability function.

In Fig. 6.6, we plot $M(\lambda)$ for the case without an adaptive control rule. The stable region is a circle with radius $\lambda_+ \approx 0.48$. In Fig. 6.7, we plot M along different linear cuts starting from the origin (for the lines $y = 0$, $y = x/2$, $y = x$, $y = 2x$

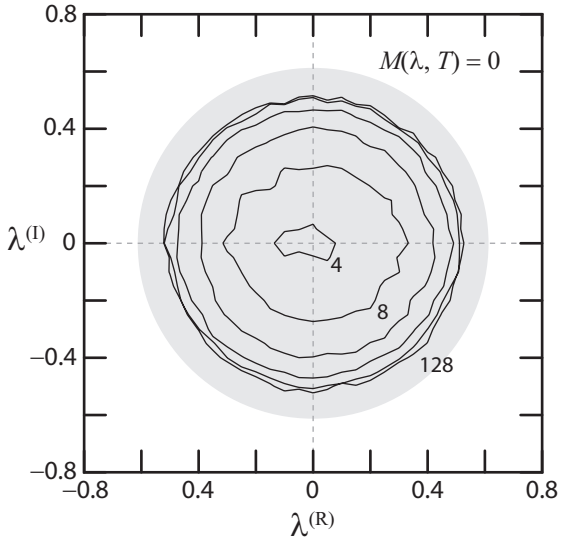

Figure 6.8: Stability contours $M(\lambda, z_0) = 0$ for different values of z_0. The six contours are for z_0 such that the averaging window $(1 - z_0)^{-1}$ is 4, 8, 16, 32, 64, and 128 time steps. For shorter averaging times, the rotational symmetry is broken.

and $y = -x$ where $\lambda = x + iy$, as depicted by dashed lines in Fig. 6.6). All of these curves fall roughly on top of one another; thus M is indeed rotationally symmetric.

To further examine the shape for time-delayed master stability functions, we calculate the stability contours $M = 0$ as we vary the adaptive control time-scale coefficient z_0. We expect that as $z_0 \to 0$ the region of stability shrinks and as $z_0 \to 1$ the region asymptotically approaches the uncontrolled case. In Fig. 6.8, the contours for $(1-z_0)^{-1} = 4$, 8, 16, 32, 64, and 128 are plotted. For the latter four examples, the shape closely resembles a circle. For the 4 and 8 cases, where the region of stability is focused closely near $\lambda = 0$, the circular symmetry is broken. The adaptive control algorithm introduces a new time scale for the dynamical behavior $T = T_s(1 - z_0)^{-1}$ in terms of the state variables p_i and q_i. For small T, the time scale of the coupled system (x_i, p_i, q_i) may be dominated by T rather than τ_L, and thus the Flunkert

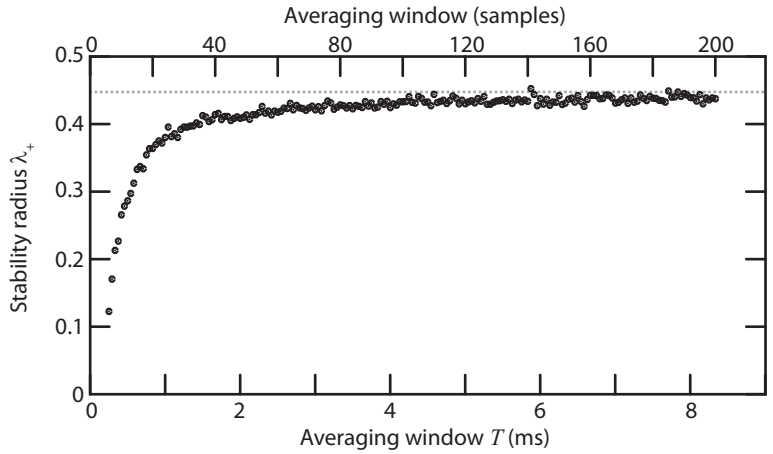

Figure 6.9: Stability radius of as averaging time $T = T_s(1 - z_0)^{-1}$ is varied. For $T > 2$ ms, they asymptotically approach $r_0 \approx 0.45$.

theory fails. In Fig. 6.9, we plot the critical radius r_0 of the master stability function M as a function of the adaption coefficient T. The radius asymptotically approaches an upper bound. This result is practically useful in choosing the z_0 parameter that maximizes the range of stability for a given speed of channel fluctuations. It is evident that choosing T much larger than 2 ms has little effect on enlarging the range of stable operation.

For a rotationally symmetric master stability function, all the information about the stability of the synchronous state for an arbitrary weighted network is composed in single scalar function $M(|\lambda|)$. Only the magnitudes of the relevant eigenvalues $|\lambda_j|$ are required to determine if the configuration $\mathbf{A}$ can maintain synchronous operation. A two-node unidirectional network with a variable coupling strength A_{21} can be used to ascertain the stability range. Namely by determining the upper and lower bound of A_{12} for which the two oscillators synchronize, the stability radius r_0 is ascertained and can be applied to all configurations of N oscil-

lators. This is a powerful result that reduces the complexity of the stability problem for a large class of time-delay networks.

6.6 Summary

1. An adaptive synchronization scheme maintains the synchronous state of identical coupled chaotic oscillators in the presence of time-varying coupling strengths.

2. The stability of adaptive synchronization is addressed by extending the master stability function technique to include adaptation.

3. The eigenvalues of the rescaled coupling matrix $\mathbf{A}'$ must fall within a specified region of the complex plane for the network to support synchronism.

4. The range of stability is substantially affected by the adaptation coefficient which characterizes the time-scales for which an adaptive network can sense perturbations to its coupling structure.

5. The master stability function for the class of time-delay networks has a circular shape in the complex plane.

Chapter 7

Prediction of network convergence rate

Upon enabling coupling and information exchange, the dynamics of an initially noninteracting collection of chaotic oscillators may fall into a state of synchronism. The master stability function framework allows us to predict whether a given interaction arrangement fosters such entrainment [30]. Recently, the rate μ at which a synchronizable network converges into synchrony has been recognized as an important metric for classifying and ranking the network [56]. A faster convergence rate is correlated with enhanced stability, more rapid recovery from perturbations, and reduced sensitivity to parameter mismatches and noise. These observations can also be understood in terms of the master stability function framework, which mathematically decouples the detailed time evolution of each node on the network from the dynamical role performed by the network interaction structure. While network structure underlies the process of synchronization, we can analyze network structure independently from the dynamics *on* the network . In particular, experiments on a small network (in which all the system parameters are under precise control) can be used to infer or predict the performance of much larger networks [58]. In this chapter, we study the convergence properties of a two-node auxiliary network, develop a theory of how to apply the results to an arbitrary network, and test the conjecture with experiments on a four-node network and numerical simulations of a

50-node network.

7.1 Network convergence

To begin, let us formalize what is meant by network convergence and present a method for experimentally measuring it. Consider a network of N chaotic oscillators whose internal states are $\mathbf{u}_i(t)$. Let the scalar $x_i(t)$ be an observed variable. In terms of the optoelectronic feedback loops, $\mathbf{u}_i$ is the state space vector pertaining to the bandpass filter and x_i is the output of the filter, which is amplified and used to modulate the amplitude of the optical signal. In the fully chaotic regime, a pair of isolated feedback loops will have little or no correlation between their dynamical signals: $\langle x_1(t)x_2(t)\rangle \approx 0$. If the pair is coupled in such a way as to generate synchrony, the difference $x_1 - x_2$ is approximately zero. If coupling between the two oscillators is established at a particular moment of time, then there must be a transition from the initially uncorrelated dynamics to the synchronous state. The convergence rate μ quantifies this transition period; μ is the exponential decay rate of the synchronization error $x_1 - x_2$ from large to small: $|x_1 - x_2| \sim e^{-\mu t}$.

We generalize this definition for a network of N oscillators, where we must consider $N(N-1)$ difference terms $|x_i - x_j|$ for $i, j = 1, \ldots, N$ (excluding the N $i = j$ terms). Let $t = 0$ be the time when coupling is enabled between the oscillators: before $t = 0$, $A_{ij} = 0$ for all $i \neq j$, and at $t = 0$, the A_{ij}'s go to static predetermined values. We measure the global synchronization error $\theta(t)$ as the average pairwise

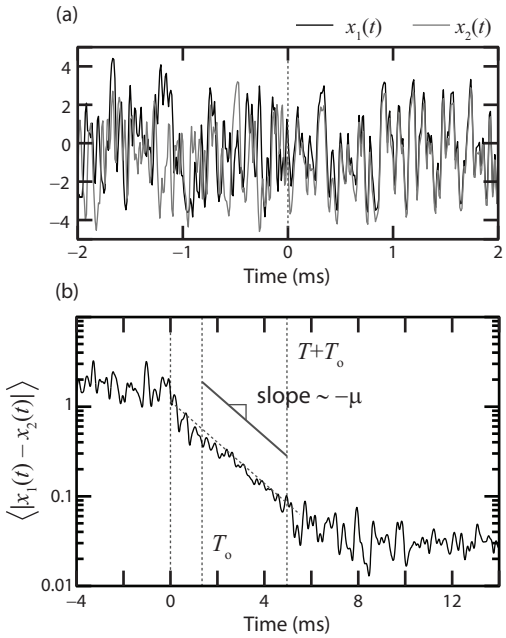

Figure 7.1: (a) Initially ($t < 0$) the two nodes operate independently. At $t = 0$, coupling is immediately enabled and the time-series $x_1(t)$ and $x_2(t)$ converge in synchronous state, i.e. $x_1 - x_2 \to 0$. (b) Estimation of the exponential rate of convergence μ in the time window between $t = T_0$ and $t = T + T_0$. For $t > T + T_0$, the synchronization floor is reached.

difference:

$$\theta(t) = \frac{1}{N(N-1)} \sum_{i,j=1} N|x_i(t) - x_j(t)|. \tag{7.1}$$

If the full network synchronizes, then we expect $\theta(t) \approx 0$ after a transient period. In practice, it is not identically zero, because there are unavoidable mismatches and noise. Let θ_0 be the synchronization floor, i.e. $\theta(t) \to \theta_0$. For N synchronizing oscillators, we expect

$$(\theta(t) - \theta_0) \sim e^{-\mu t}. \tag{7.2}$$

Can we predict the rate μ for a given network topology $\mathbf{A}$? We begin to answer this question in §7.5.

Given the time-series records $\{x_i(t)\}$, how do we extract the rate μ? Consider

a network of two nodes with outputs $x_1(t)$ and $x_2(t)$. In Fig. 7.1(a), we plot the observed signals before and during the transient period. At $t = 0$, the coupling is enabled such that $\kappa x_1(t)$ is sent to system 2 and $\kappa x_2(t)$ is sent to system 1. Each node also scales its internal feedback signal by $(1 - \kappa)$ to maintain a fixed signal strength. This ensures that the eventual synchronous state $\mathbf{u}_1 = \mathbf{u}_2 = \mathbf{s}$ is the solution of an isolated node. It is observed that $x_1(t)$ and $x_2(t)$, which are initially quite different, begin to fall in line with one another. In Fig. 7.1(b), we plot the difference $|x_1(t) - x_2(t)|$ which has been boxcar averaged with a 100 μs moving window. Within the period T_0 and $T + T_0$, there is an obvious exponential relationship, represented as a line with slope $-\mu$ on this semilogarithmic scale. A best fit line to $\ln\langle|x_1 - x_2|\rangle$ between T_0 and $T + T_0$ yields μ for this pair of converging time-series. In a similar manner, a linear fit to $\ln\langle\theta(t)\rangle$ can extract the rate μ for an arbitrary network of size N.

7.2 Transverse Lyapunov exponents

For a pair of converging time-series x_1 and x_2, the rate μ will depend on the coupling strength κ as well as where along the chaotic attractor x_1 and x_2 were when coupling was enabled (at $t = 0$). In other words, the trajectories in which x_1 and x_2 approach the synchronization manifold $x_1 = x_2$ is determined by the initial conditions x_1 and x_2. This local structure within phase space is quantified by a finite time transverse Lyapunov exponent (TLE) [43, 73, 84]. The distribution of the set of TLEs around the entire attractor embeds information about the variation

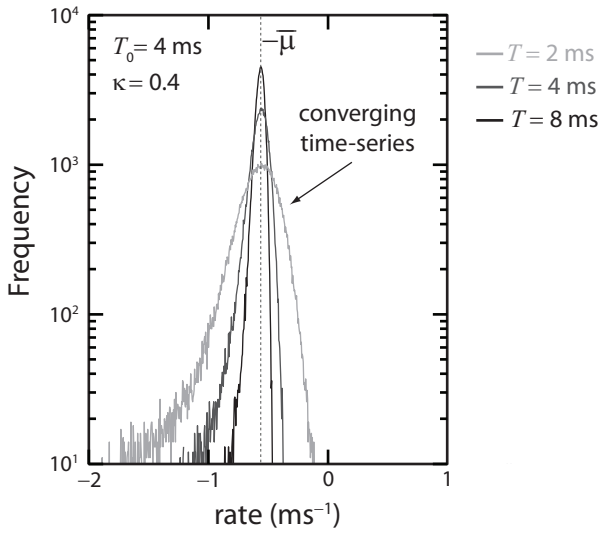

Figure 7.2: Distribution of finite time transverse Lyapunov exponents for time windows of length 2, 4, and 8 ms.

of synchronization convergence rates – some locales may induce faster convergence than others.

To measure a TLE, we enable coupling at $t = 0$ and fit an exponential relation to the difference $|x_1 - x_2|$, as described in §7.1. The time window T is associated with locality; for a short T, $x_1 - x_2$ remains confined within a relatively small region in phase space, and as $T \to \infty$, the entire attractor is traversed. In experiments, the maximal window length is set by the synchronization floor – where the exponential relation ceases. In numerical simulations, where we can study the dynamics without noise and mismatches, T can be enlarged until the synchronization error approaches a floor limited only by the numerical precision.

In Fig. 7.2, we plot histograms of the TLEs for three cases with fitting windows $T = 2$, 4 and 8 ms. The numerical simulations that produced the time-series used the discrete-time model (§2.11) with $f_1 = 100$ Hz, $f_2 = 10$ kHz, $f_s = 96$ kHz, $\tau = 230$ μs,

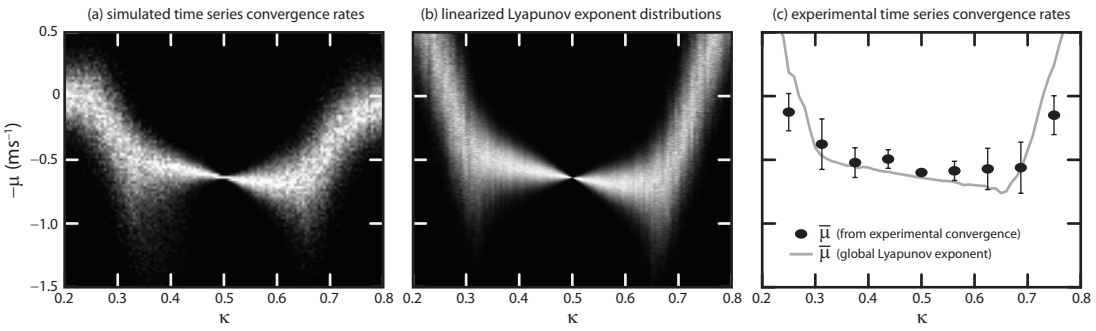

Figure 7.3: Distribution of finite time TLEs for two-node network as function of symmetric bidirectional coupling strength κ, determined by (a) time-series analysis of convergent transients, and (b) directly solving the linearized transverse equations of motion. (c) Comparison of calculated global TLEs and the measured TLEs determined by experimentally measuring the transient convergence. The data points and bars indicate the average and standard deviation of the measured statistical distribution of μ, using a finite fitting time of 4 ms. The gray line is $\bar{\mu}$ from simulation.

and $\beta = 4.5$. The TLE statistics were obtained repeating the convergence fit on 10^5 sets of different initial conditions on the chaotic attractor when the coupling strength κ was switched from 0 to 0.44. As expected, each distribution is Gaussian about a central peak and has non-Gaussian tails [43, 84]. The mean of each distribution is the average convergence rate $\bar{\mu}$ – the rate which would be measured if $T \to \infty$. $\bar{\mu}$ is called the average or global TLE. The key conclusion from this set of numerical experiments is that we can extract useful information about $\bar{\mu}$ by measuring the rates μ associated with many sets of converging experimental time-series x_1 and x_2 even if the convergence is only over an abbreviated time period.

To further support this claim, we repeat the same exercise as the coupling strength κ is varied from 0.2 to 0.8. In Fig. 7.3(a), we plot in a gray scale the distribution of TLEs $P(\mu, T)$ for $T = 4$ ms. Here black corresponds to no counts at that rate, and white corresponds to all rates within a specific bin. For example,

at $\kappa = 0.5$, x_1 and x_2 converge unconditionally at a rate determined only by the bandpass filter response, so the distribution collapses to a delta function. At $\kappa = 0.32$ and $\kappa = 0.68$, the distributions are at their broadest – implying that there is a wide variability in the observed rates μ. Since the μ's are extracted from converging time-series, only for κ values which allow stable synchrony do we obtain a reliable measure. If $(x_1 - x_2) \nrightarrow 0$, then the rate is not well-defined for this routine.

For Fig. 7.3(c), the same procedure was repeated, except for x_1 and x_2 obtained from a series of experiments. The data points are the distribution mean $\bar{\mu}$ for nine values of κ and the vertical bars are the widths of the statistical distribution. The statistics are for 100 independent trials for each coupling strength. The solid curve is the asymptotic TLE obtained by numerically integrating a linearized model (the subject of the next paragraph). Because of the excellent agreement between the means and widths of (a) and (c), we conclude that this switch experiment is a powerful tool for learning about network convergence properties. In particular, if we observe the set of N time-series $\{x_i\}$ for an N node network while simultaneously turning on all of the couplings, we can measure $\bar{\mu}$ by calculating $\theta(t)$ as in Eq. (7.1) above.

Finally, we compare the convergence rate μ obtained from analyzing transient dynamics with the conventional technique of computing phase space expansion or contraction via a linearized numerical model [30, 51]. We compute the growth rates by linearizing the difference $\delta\mathbf{u} = \mathbf{u}_1 - \mathbf{u}_2$ about the synchronous solution $\mathbf{u}_1 = \mathbf{u}_2 = \mathbf{s}$. We collect the growth factors α_j, following the standard MLE procedure (as outlined in §3.2.1). To obtain a finite time distribution of the μ's, we perform

averaging of the α_j's only over a finite number of normalization intervals J such that $J \cdot \delta t = T$. Thus, we compute a local μ as

$$-\mu = \frac{1}{T} \sum_{j=1}^{J} \ln \alpha_j. \tag{7.3}$$

By logging a running register of the μ's from different locations on the attractor (as $\mathbf{s}$ moves in phase space), we obtain $P(\mu, T)$ for a given T. Since this MLE computation can evaluate both positive or negative phase space growth, $-\mu$ can be positive unlike for the time-series convergence technique. In Fig. 7.3(b), we plot the distributions of μ for $T = 4$ ms as we vary the coupling strength κ. Apart from the expected discrepancy where $\bar{\mu} < 0$, this image matches the image in (a).

The time-series technique described here for quantifying convergence behavior of networks complements the methods of Chapter 4 for studying chaotic divergence. The common theme is that abrupt modification of couplings (either enabling or disabling them) and observation of the subsequent transient dynamics, is a powerful tool for learning about the underlying chaos and network structure. Fig. 7.1 and Fig. 4.14 are direct complements in terms of convergence and divergence, and likewise are Figs. 7.2 and 4.9.

7.3 Measured master stability function

The transient time-series analysis method for extracting $\bar{\mu}$ can be considered a measurement of the master stability function $M(\lambda)$ for real eigenvalues $\lambda \in \mathbb{R}$. The two-node network with bidirectional and symmetric coupling strength κ can be

cast into the form of a general network:

$$\frac{d\mathbf{x}_i}{dt} = \mathbf{F}(\mathbf{x}_i) + \varepsilon \sum_{j=1}^{N} A_{ij}\mathbf{H}(\mathbf{x}_j) \tag{7.4}$$

by setting $N = 2$ and

$$\mathbf{A} = \begin{bmatrix} 1-\kappa & \kappa \\ \kappa & 1-\kappa \end{bmatrix}. \tag{7.5}$$

The associated Laplacian matrix is

$$\mathbf{L} = \begin{bmatrix} \kappa & -\kappa \\ -\kappa & \kappa \end{bmatrix} \tag{7.6}$$

which has eigenvalues $\lambda_1 = 0$ and $\lambda_2 = 2\kappa$. Since the two-node network has only a single free eigenvalue 2κ, we may associate the convergence rate $\bar{\mu}$ with the stability function as $-\bar{\mu} = M(\lambda = 2\kappa)$. However, unlike the standard routine for calculating $M(\lambda)$ from linearized equations, only negative values of M can be ascertained. This does not limit the applicability of $M(\lambda)$ since the rates yielded by master stability function are only useful for synchronizable networks with $M(\lambda_k) < 0$. To establish the range of $\lambda = 2\kappa$ where $\bar{\mu} = M(\lambda)$ is valid, we constrain the function to the region with $\theta_0 < 0.1$, i.e. where the measured synchronization floor is reasonably small.

In Fig. 7.4(a), we plot θ_0 as function of λ for two optoelectronic feedback loops with parameters $f_1 = 100$ Hz, $f_2 = 2.5$ kHz, $f_s = 24$ kHz, $\tau = 1.5$ ms, and $\beta = 3.8$. The associated convergence rates $M(\lambda)$ are plotted in (b). The grayed interval is the region where $M(\lambda)$ is trusted. The stable region along the real line is $(0.57, 1.43)$.

To determine *if* a network will synchronize only $\theta_0(\lambda)$ is required. For example, for an arbitrary network with only real eigenvalues, all the eigenvalues λ_k

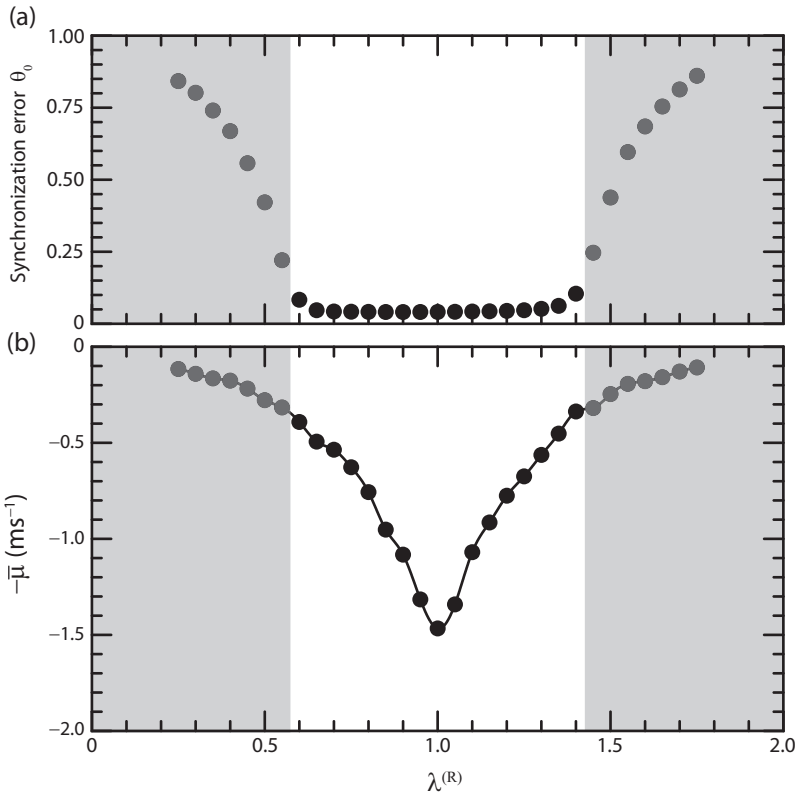

Figure 7.4: (a) Synchronization error θ_0 from a pair of coupled oscillators as the coupling strength $\kappa = \lambda/2$ is varied. For $\theta_0 < 0.10$, we obtain good synchrony. (b) Measured convergence rates which is associated with the single relevant eigenvalue of the two-node system.

must be such that $\theta_0(\lambda_k)$ is small for the synchrony to be stable. For a network with complex eigenvalues $\lambda_k = \lambda_k^{(\mathrm{R})} + i\lambda_k^{(\mathrm{I})}$, the function θ_0 with a complex argument $\lambda^{(\mathrm{R})} + i\lambda^{(\mathrm{I})}$ must be available. In Ref. [57], a three-node network was used to systematically measure the range of stability for an arbitrary network with complex eigenvalues. For delay-coupled oscillators, it may suffice to have only $\theta_0(\lambda^{(\mathrm{R})})$ since there is preliminary evidence that only distance from the global minimum (at $\lambda = 1$) is necessary for stability analysis [55]. Here, the rates $M(\lambda)$ provide an additional layer of information which is useful for classifying networks. In particular, we can associate each of the eigenvalues $\lambda_k \in \mathbb{R}$ of a network with a convergence

mode $-\mu_k = M(\lambda_k)$ to determine a global convergence rate $\langle\theta\rangle \sim e^{\mu t}$ where μ is a combination of all the rates μ_k. This is the subject of §7.5.

7.4 Optimal synchronization

An optimal network is one that maximizes synchronizability and equivalently the average convergence rate $\bar{\mu}$. Nishikawa and Motter conjecture that a network that minimizes the Laplacian eigenspread in the complex plane [56]

$$\sigma = \frac{1}{d^2(N-1)} \sum_{j=2}^{N} |\lambda_j - \bar{\lambda}|^2 \tag{7.7}$$

where

$$\bar{\lambda} = \frac{1}{N-1} \sum_{j=2}^{N} \lambda_j \tag{7.8}$$

is optimal. The minimum is $\sigma = 0$, and this is the case only if $\lambda_2 = \cdots = \lambda_N = \bar{\lambda}$, i.e. having $(N-1)$ identical eigenvalues. Binary directed networks ($A_{ij} \in \{0, 1\}$) were analyzed in detail with respect to optimality. The most important result is that an optimal network ($\sigma = 0$) must have m total links which is an integer multiple of $(N-1)$. A suboptimal network is one that minimizes σ for m not a multiple of $(N-1)$. Here we consider optimal and suboptimal networks because all their eigenvalues are real. Thus, we can directly apply $M(\lambda^{(R)})$ measured from a two-node network to optimal and suboptimal networks with an arbitrary number of nodes.

In Ref. [58], a selection of optimal and suboptimal four-node network configurations were considered experimentally. The convergence rate $\bar{\mu}$ was shown to be inversely proportional to σ: a smaller σ implies a faster convergence rate. A selection of 50-node networks were also considered numerically. We begin with a

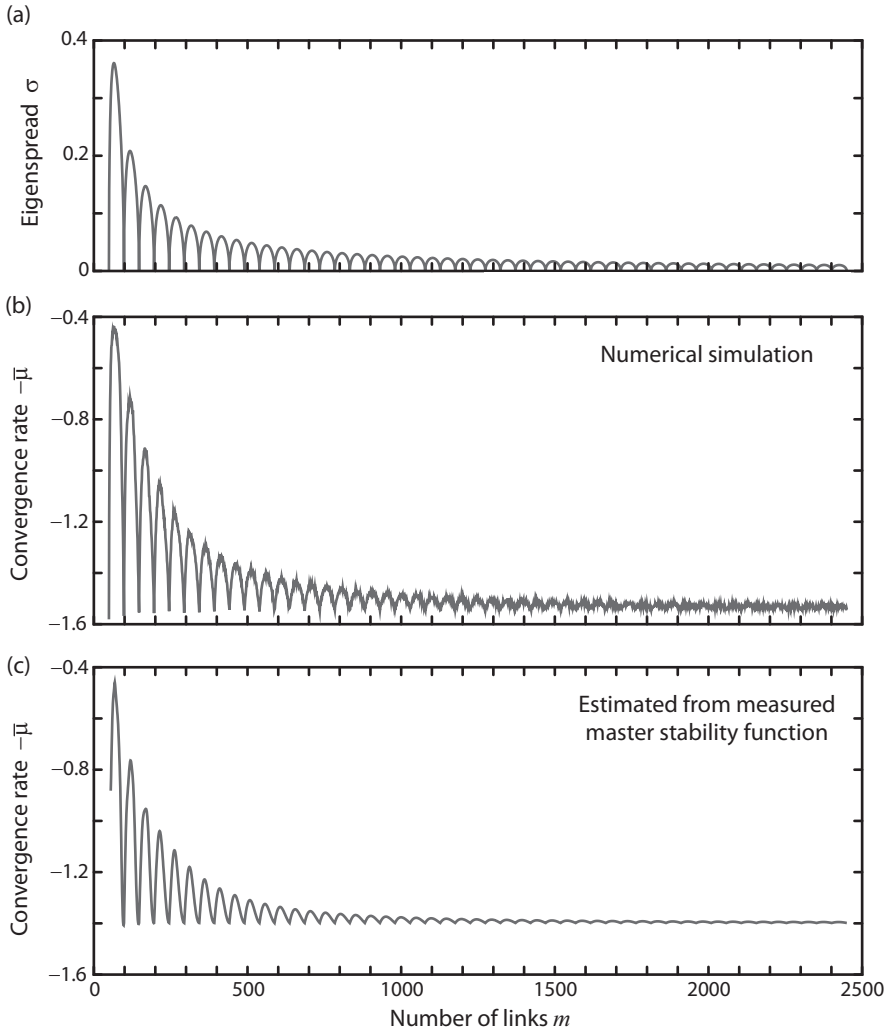

Figure 7.5: Convergence properties of 50-node optimal and suboptimal networks. (a) Eigenspread σ for a set of optimal and suboptimal networks as a function of total number of links m. (b) Average convergence rates for these networks obtained from 100 independent numerical simulations of each network starting from different initial conditions. (c) Convergence rate inferred from measured master stability function.

fully connected network with $m = N(N-1) = 2450$ links. This all-to-all network is optimal with $\lambda_k = \bar{\lambda}$ for $k = 2, \ldots, N$. Next, a link is removed as to keep σ minimized. This process is repeated until only $(N-1) = 49$ links remain. For the 2401 configurations considered, the Laplacian eigenvalue spectrum of each is populated with only real numbers, even though many of the networks are asymmetric [56]. In Fig. 7.5(a), we plot σ as a function of m, which follows a cusp-like path with minima at $m = (N-1), 2(N-1), \ldots, N(N-1) = 49, 98, \ldots, 2450$. In (b), we plot the average convergence rate $\bar{\mu}$ obtained from running a full nonlinear simulation for each network. For each configuration, the abrupt coupling procedure was repeated 100 times, the synchronization error $\theta(t)$ was fit to an exponential relation, and the average convergence rate $\bar{\mu}$ is an average from all 100 trials. As expected from theory, $\bar{\mu}$ follows a cusp-like curve with m. Is there a way to predict $\bar{\mu}$ without running a full simulation, but instead utilizing the master stability function $M(\lambda)$?

7.5 Estimating convergence rate from master stability function

Each Laplacian eigenvalue λ_k is associated with a Lyapunov exponent $M(\lambda_k)$. Typically the function $M(\lambda)$ is calculated via a linearized auxiliary equation. A subject of this thesis (Chapters 4 and 7) is diagnosing the rates $M(\lambda_k)$ via experimental measurements. In §7.3, we measure $M(\lambda)$ using controlled experiments on a two-node network. In this section, we derive a formula for constructing the transient rate $\bar{\mu}$ from the rates $-\mu_k = M(\lambda_k)$.

It is often assumed that a network will converge at the slowest rate of the

set $\{\mu_k\}_{k=2}^N$. However, this is only true infinitesimally close to the synchronization manifold where excitations of all the other modes have decayed. Far from the synchronization floor, the only regime available in experiments with a finite synchronization floor, the influence along all eigendirections is important. Yet, it is possible to use $-\mu_k = M(\lambda_k)$ to infer the expected transient rate. As described in §7.4, this rate is important for real-world characterization of network optimality. In general, we note that far from the synchronization manifold, the behavior may be dominated by nonlinear terms that are excluded in the linear stability analysis.

Consider an N node network with $(N-1)$ relevant eigenvalues $\lambda_k \in \mathbb{R}$. The associated convergence eigenrates are $-\mu_k = M(\lambda_k) < 0$. We expect each mode to relax exponentially as $e^{-\mu_k t}$, such that the overall convergence takes the form

$$\theta(t) \sim \sum_{k=2}^{N} C_k e^{-\mu_k t}. \tag{7.9}$$

The coefficients C_k are determined by the initial states of all the chaotic trajectories $\mathbf{u}_1, \mathbf{u}_2, \ldots, \mathbf{u}_N$. However, if we repeat the measurement of $\theta(t)$ many times, we may assume there is no preferential mode selected, and we set $C_k = 1$ for all k. We assume $\langle\theta(t)\rangle \sim e^{-\bar{\mu}t}$, then

$$e^{-\bar{\mu}t} = \sum_{k=2}^{N} e^{-\mu_k t} \tag{7.10}$$

(where $\langle\bullet\rangle$ represents an ensemble average over different choices of initial conditions). Differentiating both sides of Eq. (7.10) with respect to t and solving for $\bar{\mu} = \bar{\mu}(t)$, we have:

$$\bar{\mu}(t) = \frac{\sum_{k=2}^{N} \mu_k e^{-\mu_k t}}{\sum_{k=2}^{N} e^{-\mu_k t}}. \tag{7.11}$$

Thus, the observed convergence behavior $\bar{\mu}$ is a time-varying combination of all the

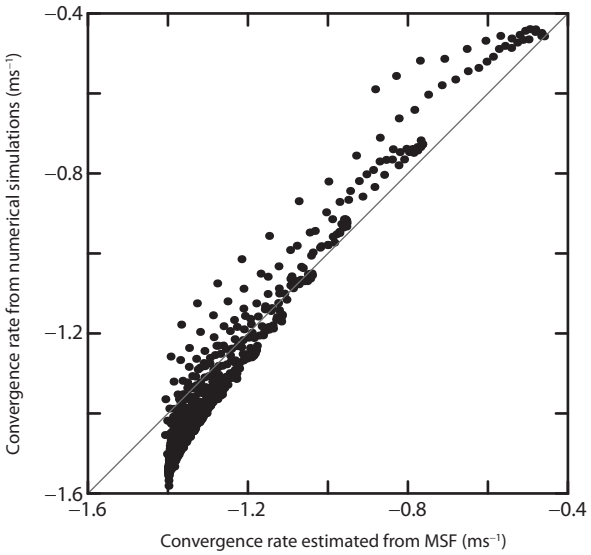

Figure 7.6: Comparison of convergence rate for 50-node network obtained from two different methods: numerical simulation and using master stability function.

rates μ_k. In the limit of small t, near to the coupling switch and far away from the synchronization manifold,

$$\bar{\mu} \approx \frac{\sum_{k=2}^{N} \mu_k}{(N-1)} = \langle \mu_k \rangle, \tag{7.12}$$

which is the average of the convergence rates (i.e. all the eigenmodes contribute equally). Far from the switch (at $t = 0$), in the limit $t \to \infty$, the dominant contribution is from the slowest rate, as expected.

In Fig. 7.5(c), we plot the derived convergence rate calculated by factoring in all the eigenmodes at small t ($t = 0$). These rates agree with those determined from the full nonlinear implantations (in panel (b)). In Fig. 7.6, we plot the rates obtained with these two methods against one another, and we see reasonable agreement.

In Fig. 7.7, we plot the rates derived from theory using $M(\lambda)$ vs. the rates measured from experiments on a set of nine optimal and suboptimal four-node networks. The vertical bars are the standard deviations of the distributions of the

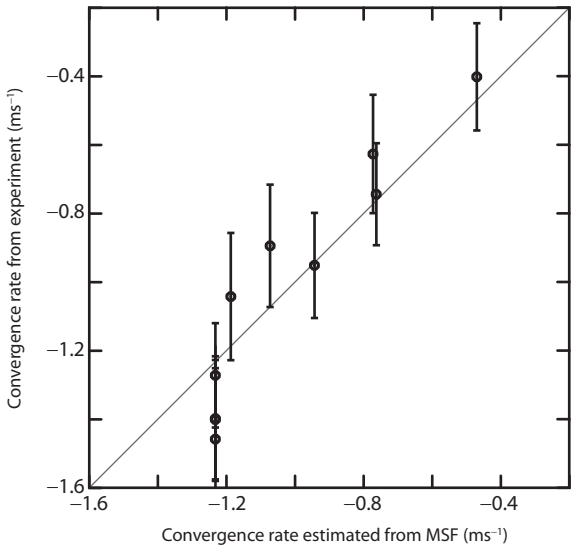

Figure 7.7: Comparison of convergence rate for four-node network obtained from two different methods: experiments and using master stability function.

measured μ's for 100 trials for each network. We conclude that we can predict the expected average convergence rate $\bar{\mu}$ for a given network with Laplacian eigenvalues λ_k.

7.6 Summary

1. The convergence rate to the synchronous state quantifies stability of a network.

2. We can measure convergence rates experimentally by enabling coupling between nodes and observing the transient dynamics to a synchronization floor.

3. The master stability function is used to predict the convergence rate for an N-node network by incorporating all $(N-1)$ synchronization modes.

4. A two-node network with controllable coupling strengths is used to experimentally measure the master stability function.

5. Optimal networks, which have $(N-1)$ identical Laplacian eigenvalues, have the fastest rates of convergence.

Chapter 8

Conclusion

The major theme of the projects outlined in this thesis is that advances in nonlinear science are achieved through a balance of controlled experiments, numerical modeling, and theoretical analysis. In nonlinear systems, the dynamics of an interconnected network cannot necessarily be understood in terms of the behavior of the individual components. However, sometimes we can arrange a complex network into a particular configuration that allows us to comprehend the myriad interdependencies present in the system and identify the responsible mechanisms. The phenomenon of synchronization – in which global order emerges out of a decentralized communication process – provides a powerful toolbox for studying and applying chaos. The mathematical and experimental realizations of synchrony are relatively simple, and yet they have provided fundamental insights into the nature chaos and order. In this thesis, we focus on a prototype nonlinear oscillator which captures many basic features found in a large class of systems, including: a route into chaos, time-delayed feedback, and a range of time scales. We construct an array of such node systems into a network, and we tune the network into synchrony. Experimentation and analysis of the synchronous state allows us to design a strategy for time-series prediction and quantification of chaos, test an adaptive technique for maintaining synchrony when coupling parameters fluctuate, and diagnose what

set of interactions optimize synchrony. While these procedures were applied to a specific network of optoelectronic oscillators, the results have implications for our basic understanding of other complex networks, including those composed of genes, cells, or people. The main conclusion from the set of experiments, simulations, and analyses presented in this thesis is: by observing the response of an entire network to time-evolution of the network structure (be it slow variations in the individual coupling strengths or rapid shocks that either induce or destroy synchrony), we can garner a basic understanding of how collective behavior emerges.

8.1 Proposed research topics

In this final section, we discuss some ideas for potential topics of research on a network of time-delayed optoelectronic feedback loops.

8.1.1 Random number generation

The chaos generated by a time-delayed feedback oscillator may be a source for high-quality, difficult-to-predict pseudorandom numbers [7]. For example, the output dynamical signal from a semiconductor laser with time-delayed optical feedback has been shown to have no detectable non-random features by passing a battery of statistical tests developed by NIST [7, 62, 77]. The optoelectronic feedback loops hold promise as a random number generator. By increasing the bandwidth of the feedback channel into tens of gigahertz, it is possible to sample the dynamical signal with a high-speed digitizer. The output bit sequence can be analyzed for correlation

and patterns that are expected for chaotic motion. A major advantage of studying optoelectronic feedback loops over other systems for this purpose is the potential for realistic modeling of the underlying dynamics. For this system, the relationship between randomness, dynamical entropy, and Lyapunov exponents can be studied in detail. As parameters are tuned (such as delay, bandwidth, feedback strength, and modulator bias), the complexity of the output bit sequences are also modified in a predictable manner. Can dynamical complexity be associated with metrics for quantifying randomness? For example, it may be that rare events embedded within a chaotic attractor are responsible for amplification of stochastic noise and thus act like a seed to sporadically reset the dynamics. Can this source of unpredictability be described in terms of the non-Gaussian tail of distributions of local Lyapunov exponents? The optoelectronic feedback loop is a good prototype system for developing requirements and standards for random number generation using chaotic sources.

8.1.2 Network reconstruction

The networks of feedback loops used for studying adaptive synchronization and optimal synchronization were carefully tuned to admit stable isochronal synchrony. The network could also be operated in a regime where the individual node parameters and interaction time-delays are mismatched. Some possibilities for the network dynamics include: phase synchrony, cluster synchrony, lead/lag synchrony, or incoherence. In this latter case, the nodes are influencing each other by sharing in-

formation, yet there may be no obvious relationships in the observed dynamics. Can the interaction structure be identified from the observational data sets [79]? This is the inverse network problem, in which the adjacency matrix is reconstructed. By carefully selecting the network parameters (coupling strengths and delay), we may have a priori knowledge of the underlying network; yet, do network forensics based on dynamical signals uncover other hidden relationships? For example, long-range interactions (using dynamical nodes as relays) may play an important role which is not directly evident through the network structure [108].

8.1.3 Master stability function symmetries

An experimental network of three optoelectronic feedback loops with uniform coupling delays τ is an ideal system for studying symmetries of the master stability function in the complex plane [55]. By systematically tuning the six independent coupling strength parameters A_{ij} $(i \neq j)$, and measuring the network convergence rate $\bar{\mu}$, the stability contours M can be ascertained [57]. How do the shape of the contours evolve as the coupling delay τ is varied? Is rotational symmetry broken for a certain range of τ? How robust are predictions regarding $M(\lambda)$ for real-world parameter mismatches and noise? Can we interpret the universal nature of master stability functions for delay-coupled oscillators in terms of certain local motifs [36]?

Bibliography

[1] S. H. Strogatz, *Sync: how order emerges from chaos in the universe, nature, and daily life*. New York: Hyperion, 1 ed., 2003.

[2] Y. Chembo Koumou, P. Colet, L. Larger, and N. Gastaud, "Chaotic breathers in delayed electro-optical systems," *Physical Review Letters*, vol. 95, p. 203903, 2005.

[3] A. Argyris *et al.*, "Chaos-based communications at high bit rates using commercial fibre-optic links," *Nature*, vol. 438, pp. 343–346, 2005.

[4] G. D. VanWiggeren and R. Roy, "Chaotic communication using time-delayed optical systems," *International Journal of Bifucations and Chaos*, vol. 9, pp. 2129–2156, 1998.

[5] B. Ravoori *et al.*, "Adaptive synchronization of coupled chaotic oscillators," *Physical Review E*, vol. 80, p. 056205, 2009.

[6] K. E. Callan *et al.*, "Broadband chaos generated by an optoelectronic oscillator," *Physical Review Letters*, vol. 104, p. 113901, 2010.

[7] A. Uchida *et al.*, "Fast physical random bit generation with chaotic semiconductor lasers," *Nature Photonics*, vol. 2, pp. 728–732, 2008.

[8] T. E. Murphy *et al.*, "Complex dynamics and synchronization of delayed-feedback nonlinear oscillators," *Proceedings of the Royal Society of London A*, vol. 368, pp. 343–366, 2010.

[9] L. Illing and D. J. Gauthier, "Hopf bifurcations in time-delay systems with band-limited feedback," *Physica D*, vol. 210, pp. 180–202, 2005.

[10] A. B. Cohen, B. Ravoori, T. E. Murphy, and R. Roy, "Using synchronization for prediction of high dimensional chaotic dynamics," *Physical Review Letters*, vol. 101, p. 154102, 2008.

[11] F. M. Atay, *Complex Time-Delay Systems: Theory and Applications*. Berlin: Springer, 1 ed., 2010.

[12] A. E. Siegman, *Lasers*. Sausalito, California: University Science Books, 1 ed., 1986.

[13] M. C. Mackey and L. Glass, "Oscillation and chaos in physiological control systems," *Science*, vol. 197, pp. 287–289, 1977.

[14] L. C. Davis, "Modifications of the optimal velocity traffic model to include delay due to driver reaction time," *Physica A*, vol. 319, pp. 557–567, 2003.

[15] K. Pyragas, "Continuous control of chaos by self-controlling feedback," *Physical Letters A*, vol. 170, pp. 421–428, 1992.

[16] M. Schanz and A. Pelster, "Analytical and numerical investigations of the phase-locked loop with time delay," *Physical Review E*, vol. 67, p. 056205, 2003.

[17] S. G. Hormuzdi *et al.*, "Electrical synapses: a dynamic signaling system that shapes the activity of neuronal networks," *Biochimica et Biophysica Acta - Biomembranes*, vol. 1662, pp. 113–137, 2004.

[18] A. Namajunas, K. Pyragas, and A. Tamasevicius, "An electronic analog of the Mackey-Glass system," *Physics Letters A*, vol. 201, pp. 42–46, 1995.

[19] J.-P. Thiran, "Recursive digital filters with maximally flat group delay," *IEEE Transactions on Circuit Theory*, vol. 18, pp. 659–664, 1971.

[20] A. Kittel, J. Parisi, and K. Pyragas, "Generalized synchronization of chaos in electronic circuit experiments," *Physica D*, vol. 112, pp. 459–471, 1998.

[21] *Scientific Background on the Nobel Prize in Physics 2009: Two Revolutionary Optical Technologies*. Stockholm: The Royal Swedish Academy of Sciences, 2009.

[22] F. A. Hopf, D. L. Kaplan, H. M. Gibbs, and R. L. Shoemaker, "Bifurcations to chaos in optical bistability," *Physical Review A*, vol. 25, pp. 2172–2182, 1982.

[23] J. D. Farmer, "Chaotic attractors of an infinite-dimensional dynamical system," *Physica D*, vol. 4, pp. 366–393, 1982.

[24] C. Masoller, "Spatio-temporal dynamics in the coherence collapsed regime of semiconductor lasers with optical feedback," *Chaos*, vol. 7, pp. 455–462, 1997.

[25] A. L. Franz, R. Roy, L. B. Shaw, and I. B. Schwartz, "Changing dynamical complexity with time delay in coupled fiber laser oscillators," *Physical Review Letters*, vol. 99, p. 053905, 2007.

[26] M.-Y. Kim *et al.*, "Scaling behavior of laser population dynamics with time-delayed coupling: Theory and experiment," *Physical Review Letters*, vol. 94, p. 088101, 2005.

[27] D. W. Sukow, M. E. Bleich, D. J. Gauthier, and J. E. S. Socolar, "Controlling chaos in a fast diode resonator using extended time-delay autosynchronization: Experimental observations and theoretical analysis," *Chaos*, vol. 7, pp. 560–576, 1997.

[28] D. J. Gauthier, "Controlling lasers by use of extended time-delay autosynchronization," *Optics Letters*, vol. 23, pp. 703–705, 1998.

[29] S. H. Strogatz, "From Kuramoto to Crawford: exploring the onset of synchronization in populations of coupled oscillators," *Physica D*, vol. 143, pp. 1–20, 2000.

[30] L. M. Pecora and T. L. Carroll, "Master stability functions for synchronized coupled systems," *Physical Review Letters*, vol. 80, p. 2109, 1998.

[31] M. Bennett, M. F. Schatz, H. Rockwood, and K. Wiesenfeld, "Huygens's clocks," *Proceedings of the Royal Society of London A*, vol. 458, pp. 563–579, 2002.

[32] S. H. Strogatz *et al.*, "Theoretical mechanics: Crowd synchrony on the Millennium Bridge," *Nature*, vol. 438, pp. 43–44, 2005.

[33] A. F. Taylor *et al.*, "Dynamical quorum sensing and synchronization in large populations of chemical oscillators," *Science*, vol. 323, pp. 614–617, 2009.

[34] W. Singer, "Neuronal synchrony: a versatile code for the definition of relations?," *Neuron*, vol. 24, pp. 49–65, 1999.

[35] P. J. Uhlhaas and W. Singer, "Neural synchrony in brain disorders: Relevance for cognitive dysfunctions and pathophysiology," *Neuron*, vol. 52, pp. 155–168, 2006.

[36] R. Milo *et al.*, "Network motifs: Simple building blocks of complex networks," *Science*, vol. 298, pp. 824–827, 2002.

[37] F. Sorrentino and E. Ott, "Adaptive synchronization of dynamics on evolving complex networks," *Physical Review Letters*, vol. 100, p. 114101, 2008.

[38] J. Zamora-Munt, C. Masoller, J. García-Ojalvo, and R. Roy, "Crowd synchrony and quorum sensing in delay-coupled lasers," *Physical Review Letters*, vol. 105, p. 246101, 2010.

[39] K. M. Coumo and A. V. Oppenheim, "Circuit implementation of synchronized chaos with applications to communications," *Physical Review Letters*, vol. 71, pp. 65–68, 1993.

[40] G. D. VanWiggeren and R. Roy, "Communication with chaotic lasers," *Science*, vol. 279, pp. 1198–1200, 1998.

[41] E. Kalnay, *Atmospheric Modeling, Data Assimilation and Predictability*. Cambridge: Cambridge University Press, 1 ed., 2002.

[42] A. B. Cohen *et al.*, "Dynamic synchronization of a time-evolving optical network of chaotic oscillators," *Chaos*, vol. 20, p. 043142, 2010.

[43] A. Prasad and R. Ramaswamy, "Characteristic distributions of finite-time Lyapunov exponents," *Physical Review E*, vol. 60, pp. 2761–2766, 1999.

[44] A. Uchida *et al.*, "Local conditional Lyapunov exponent characterization of consistency of dynamical response of the driven Lorenz system," *Physical Review E*, vol. 78, p. 036203, 2008.

[45] E. Ott, T. Sauer, and J. A. Yorke, *Coping with Chaos: Analysis of Chaotic Data and the Exploitation of Chaotic Systems*. New York: Wiley-Interscience, 1 ed., 1994.

[46] T. Sauer, "Time series prediction by using delay coordinate embedding," in *Time Series Prediction: Forecasting the Future and Understanding the Past* (A. S. Weigend and N. A. Gershenfeld, eds.), Boulder, Colorado: Westview Press, 1993.

[47] M. Casdagli, "Nonlinear prediction of chaotic time series," *Physica D*, vol. 35, pp. 335–356, 1989.

[48] I. Fischer *et al.*, "Zero-lag long-range synchronization via dynamical relaying," *Physical Review Letters*, vol. 97, p. 123902, 2006.

[49] B. B. Zhou and R. Roy, "Isochronal synchrony and bidirectional communication with delay-coupled nonlinear oscillators," *Physical Review E*, vol. 75, p. 026205, 2007.

[50] E. A. Rogers-Dakin, J. García-Ojalvo, D. J. DeShazer, and R. Roy, "Synchronization and symmetry breaking in mutually coupled fiber lasers," *Physical Review E*, vol. 73, p. 045201(R), 2006.

[51] H. Fujisaka and T. Yamada, "Stability theory of synchronized motion in coupled-oscillator systems," *Progress of Theoretical Physics*, vol. 69, pp. 32–47, 1983.

[52] F. Sorrentino, G. Barlev, A. B. Cohen, and E. Ott, "The stability of adaptive synchronization of chaotic systems," *Chaos*, vol. 20, p. 013103, 2010.

[53] T. Nishikawa and A. E. Motter, "Synchronization is optimal in nondiagonalizable networks," *Physical Review E*, vol. 73, p. 065106(R), 2006.

[54] L. Huang, Q. Chen, Y.-C. Lai, and L. M. Pecora, "Generic behavior of master-stability functions in coupled nonlinear dynamical systems," *Physical Review E*, vol. 80, p. 036204, 2009.

[55] V. Flunkert, S. Yanchuk, T. Dahms, and E. Schöll, "Synchronizing distant nodes: A universal classification of networks," *Physical Review Letters*, vol. 105, p. 254101, 2010.

[56] T. Nishikawa and A. E. Motter, "Network synchronization landscape reveals compensatory structures, quantization, and the positive effect of negative interactions," *Proceedings of the National Academy of Sciences USA*, vol. 107, pp. 10342–10347, 2010.

[57] K. S. Fink *et al.*, "Three coupled oscillators as a universal probe of synchronization stability in coupled oscillator arrays," *Physical Review E*, vol. 61, pp. 5080–5090, 2000.

[58] B. Ravoori *et al.*, "Robustness of optimal synchronization in real networks," *Physical Review Letters*, vol. 107, p. 034102, 2011.

[59] H. U. Voss, "Anticipating chaotic synchronization," *Physical Review E*, vol. 61, pp. 5115–5119, 2000.

[60] G. P. Agrawal and N. K. Dutta, *Semiconductor Lasers*. New York: Van Nostrand Reinhold, 2 ed., 1993.

[61] D. A. B. Miller, *Course Notes for EE243, Semiconductor Optoelectronic Devices*. Stanford University, 2004.

[62] I. Reidler, Y. Aviad, M. Rosenbluh, and I. Kanter, "Ultrahigh-speed random number generation based on a chaotic semiconductor laser," *Physical Review Letters*, vol. 103, p. 024102, 2009.

[63] T. E. Murphy and R. Roy, "Chaotic lasers: The world's fastest dice," *Nature Photonics*, vol. 2, pp. 714–715, 2008.

[64] J. Hecht, *City of Light: The Story of Fiber Optics*. New York: Oxford University Press, 1999.

[65] R. W. Boyd, *Nonlinear Optics*. San Diego, California: Academic Press, 2 ed., 2003.

[66] H. C. LeFevre, "Fiber optic polarization controller," 1983. US Patent 4389090.

[67] M. Born and E. Wolf, *Principles of Optics: Electromagnetic Theory of Propagation, Interference and Diffraction of Light*. Cambridge: Cambridge University Press, 7 ed., 1999.

[68] M. A. Green, *Solar Cells: Operating Principles, Technology, and System Applications*. Englewood Cliffs, New Jersey: Prentice Hall, 1 ed., 1982.

[69] B. Ravoori, *Synchronization of chaotic optoelectronic oscillators: Adaptive techniques and the design of optimal networks*. PhD thesis, University of Maryland, College Park, 2011.

[70] A. Wolf, J. B. Swift, H. L. Swinney, and J. A. Vastanoa, "Determining Lyapunov exponents from a time series," *Physica D*, vol. 16, pp. 285–317, 1985.

[71] J.-P. Eckmann, S. O. Kamphorst, D. Ruelle, and S. Ciliberto, "Liapunov exponents from time series," *Physical Review A*, vol. 34, pp. 4971–4979, 1986.

[72] J. C. Sprott, *Chaos and Time-Series Analysis*. New York: Oxford University Press, 1 ed., 2003.

[73] E. Ott, *Chaos in Dynamical Systems*. New York: Cambridge University Press, 2 ed., 2002.

[74] M. Sano and Y. Sawada, "Measurement of the Lyapunov spectrum from a chaotic time series," *Physical Review Letters*, vol. 55, pp. 1082–1085, 1985.

[75] H. von Bremen, F. Udwadia, and W. Proskurowski, "An efficient QR based method for the computation of Lyapunov exponents," *Physica D*, vol. 101, pp. 1–16, 1997.

[76] I. Kanter *et al.*, "An optical ultrafast random bit generator," *Nature Photonics*, vol. 4, pp. 58–61, 2010.

[77] A. Argyris, "Implementation of 140 Gb/s true random bit generator based on a chaotic photonic integrated circuit," *Optics Express*, vol. 18, pp. 18763–18768, 2010.

[78] T. M. Cover and J. A. Thomas, *Elements of information theory*. Hoboken, New Jersey: John Wiley and Sons, 2 ed., 2006.

[79] T. Schreiber, "Measuring information transfer," *Physical Review Letters*, vol. 85, pp. 461–464, 2000.

[80] K. Otsuka, J.-Y. Ko, T. Ohtomo, and K. Ohki, "Information circulation in a two-mode solid-state laser with optical feedback," *Physical Review E*, vol. 64, p. 056239, 2001.

[81] M. G. Rosenblum and A. S. Pikovsky, "Detecting direction of coupling in interacting oscillators," *Physical Review E*, vol. 64, p. 045202(R), 2001.

[82] Y. Chembo Kouomo, *Nonlinear Dynamics of Semiconductor Laser Systems with Feedback: Applications to Optical Chaos Cryptography, Radar Frequency Generation and Transverse Mode Control*. PhD thesis, University of the Balearic Islands, Palma de Mallorca, Spain, 2006.

[83] H. D. I. Abarbanel, D. R. Creveling, and J. M. Jeanne, "Estimation of parameters in nonlinear systems using balanced synchronization," *Physical Review E*, vol. 77, p. 016208, 2008.

[84] S. Datta and R. Ramaswamy, "Non-Gaussian fluctuations of local Lyapunov exponents at intermittency," *Journal of Statistical Physics*, vol. 113, pp. 283–295, 2003.

[85] H. D. I. Abarbanel, *Analysis of Observed Chaotic Data*. New York: Springer, 1 ed., 1996.

[86] T. Heil *et al.*, "Chaos synchronization and spontaneous symmetry-breaking in symmetrically delay-coupled semiconductor lasers," *Physical Review Letters*, vol. 86, pp. 795–798, 2001.

[87] L. B. Shaw, I. B. Schwartz, E. A. Rogers, and R. Roy, "Synchronization and time shifts of dynamical patterns for mutually delay-coupled fiber ring lasers," *Chaos*, vol. 16, p. 015111, 2006.

[88] E. Klein *et al.*, "Stable isochronal synchronization of mutually coupled chaotic lasers," *Physical Review E*, vol. 73, p. 066214, 2006.

[89] A. K. Engel, P. Konig, A. K. Kreiter, and W. Singer, "Interhemispheric synchronization of oscillatory neuronal responses in cat visual cortex," *Science*, vol. 252, pp. 1117–1179, 1991.

[90] P. Konig, A. K. Engel, and W. Singer, "Relation between oscillatory activity and long-range synchronization in cat visual cortex," *Proceedings of the National Academy of Sciences USA*, vol. 92, pp. 290–294, 1995.

[91] I. B. Schwartz and L. B. Shaw, "Isochronal synchronization of delay-coupled systems," *Physical Review E*, vol. 75, p. 046207, 2007.

[92] M. Zigzag *et al.*, "Zero-lag synchronization and multiple time delays in two coupled chaotic systems," *Physical Review E*, vol. 81, p. 036215, 2010.

[93] A. Englert, S. Heiligenthal, W. Kinzel, and I. Kanter, "Synchronization of chaotic networks with time-delayed couplings: An analytic study," *Physical Review E*, vol. 83, p. 046222, 2011.

[94] A. Englert *et al.*, "Zero lag synchronization of chaotic systems with time delayed couplings," *Physical Review Letters*, vol. 104, p. 114102, 2010.

[95] M. J. Berry, II, I. H. Brivanlou, T. A. Jordan, and M. Meister, "Anticipation of moving stimuli by the retina," *Nature*, vol. 398, pp. 334–338, 1999.

[96] T. Hosoya, S. A. Baccus, and M. Meister, "Dynamic predictive coding by the retina," *Nature*, vol. 436, pp. 71–77, 2006.

[97] H. U. Voss, "Dynamic long-term anticipation of chaotic states," *Physical Review Letters*, vol. 87, p. 014102, 2001.

[98] H. U. Voss, "Real-time anticipation of chaotic states of an electronic circuit," *International Journal of Bifucations and Chaos*, vol. 12, pp. 1619–1625, 2002.

[99] Y. Liu *et al.*, "Experimental observation of complete chaos synchronization in semiconductor lasers," *Applied Physics Letters*, vol. 80, pp. 4306–4308, 2002.

[100] M. Ciszak *et al.*, "Anticipating the response of excitable systems driven by random forcing," *Physical Review Letters*, vol. 90, p. 204102, 2003.

[101] M. Mendoza, S. Boccaletti, and A. Politi, "Convective instabilities of synchronization manifolds in spatially extended systems," *Physical Review E*, vol. 69, p. 047202, 2004.

[102] M. Ciszak *et al.*, "Approach to predictability via anticipated synchronization," *Physical Review E*, vol. 72, p. 046218, 2005.

[103] H. Wei and L. Li, "Estimating parameters by anticipating chaotic synchronization," *Chaos*, vol. 20, p. 023112, 2010.

[104] F. Sorrentino and M. Porfiri, "Analysis of parameter mismatches in the master stability function for network synchronization," *European Physics Letters*, vol. 93, p. 50002, 2011.

[105] J. G. Restrepo, E. Ott, and B. R. Hunt, "Spatial patterns of desynchronization bursts in networks," *Physical Review E*, vol. 69, p. 066215, 2004.

[106] J. Sun, E. M. Bollt, and T. Nishikawa, "Master stability functions for coupled nearly identical dynamical systems," *European Physics Letters*, vol. 85, p. 60011, 2009.

[107] S. C. Venkataramani *et al.*, "Transitions to bubbling of chaotic systems," *Physical Review Letters*, vol. 77, pp. 5361–5364, 1996.

[108] J. F. Donges, Y. Zou, N. Marwan, and J. Kurths, "The backbone of the climate network," *European Physics Letters*, vol. 87, p. 48007, 2009.